August 2016

Characterization of Impact Properties of Forged, Layered, and Additive Manufactured Titanium Alloy

Melissa Kathryn Matthes
University of Nevada, Las Vegas

CHARACTERIZATION OF IMPACT PROPERTIES OF FORGED, LAYERED, AND ADDITIVE MANUFACTURED TITANIUM ALLOY

By

Melissa Kathryn Matthes

Bachelor of Science – Mechanical Engineering

University of Nevada, Las Vegas

May 2015

A thesis submitted in partial fulfillment

of requirements for the

Master of Science in Engineering- Mechanical Engineering

Department of Mechanical Engineering

Howard R. Hughes College of Engineering

The Graduate College

University of Nevada, Las Vegas

August 2016

UNLV | GRADUATE COLLEGE

Thesis Approval

The Graduate College
The University of Nevada, Las Vegas

August 1, 2016

This thesis prepared by

Melissa Matthes

entitled

Characterization of Impact Properties of Forged, Layered, and Additive Manufactured Titanium Alloy

is approved in partial fulfillment of the requirements for the degree of

Master of Science in Engineering - Mechanical Engineering
Department of Mechanical Engineering

Mohamed Trabia, Ph.D.
Examination Committee Co-Chair

Kathryn Hausbeck Korgan, Ph.D.
Graduate College Interim Dean

Brendan O'Toole, Ph.D.
Examination Committee Co-Chair

Jaeyun Moon, Ph.D.
Examination Committee Member

Robert S. Hixson, Ph.D.
Examination Committee Member

Moses Karakouzian, Ph.D.
Graduate College Faculty Representative

ABSTRACT

CHARACTERIZATION OF IMPACT PROPERTIES OF FORGED, LAYERED, AND ADDITIVE MANUFACTURED TITANIUM ALLOY

BY: Melissa Matthes

Dr. Mohamed B. Trabia, Examination Committee Chair
Associate Dean for Research, Graduate Studies, and Computing
Professor of Mechanical Engineering
University of Nevada, Las Vegas

Dr. Brendan J. O'Toole, Examination Committee Chair
Chair, Department of Mechanical Engineering
Co-Director, Center for Math, Science and Engineering Education
Professor of Mechanical Engineering
University of Nevada, Las Vegas

New additive manufactured (AM) materials have the potential of optimizing the geometry and microstructure of complex components to enhance their structural integrity while creating them quickly. However, the behavior of AM materials under extreme dynamic loading conditions is not fully understood. This is especially important in many applications. For example, spacecraft components may be impacted by micrometeorites at hyper velocities of multiple kilometers per second, inducing extreme dynamic loading.

One type of AM material is created by melting and solidifying metal along a specified path. Depending on the geometry, additional streams will be deposited side-by-side. This process affects the microstructure of the AM part. More voids will exist in a typical AM part as compared to its forged counterpart. While some researchers studied the mechanical

characteristics of AM metallic components under static and some dynamic loading, no comparable research for behavior under extreme dynamic loading could not be found.

The objective of this thesis is to experimentally and computationally study the behavior of titanium alloy, Ti-6Al-4V (Grade 5), under shock loading by comparing forged and layered titanium to the AM titanium. In these experiments, the target materials were subjected to hypervelocity impact using a two-stage light gas gun. A Photonic Doppler Velocimetry (PDV) diagnostics system was used to measure free-surface velocity on the back of each target configuration. The experimental measurements were well documented and can be used to describe the behavior of these materials under shock loading. In addition to velocity measurements, physical damage and spall crack formation were monitored. The experimental measurements were used to validate computational simulations of the experiments.

It was determined that AM and forged titanium produce similar velocity profiles during the early stage of impact, with the AM targets exhibiting spall at lower velocities and the multi-layered stacks exhibiting vibrations between plates. Simulations of single layer forged and AM materials provide a good match to experimental data. This study will provide insights into the failure mechanisms of AM titanium under extreme dynamic loading.

ACKNOWLEDGEMENTS

First, I would like to express my very great appreciation to my loving parents and sister for their continued support and patience during the preparation for this final project. I am particularly grateful to Dr. Brendan O'Toole and Dr. Mohammed Trabia for their constructive suggestions during the planning and development of this research work. Especially want to thank them for their willingness to give their time so generously; even when they had a significant amount of other obligations. I want to acknowledge the gas gun lab team Richard Jennings, Eric Bodenchak, and Matthew Boswell for their assistance in gas gun operations. Finally I want to especially thank Dr. Muna Slewa for helping me polish some of my samples.

This manuscript has been authored by National Security Technologies, LLC, under Contract No. DE-AC52-06NA25946 with the U.S. Department of Energy and supported by the Site-Directed Research and Development Program. The United States Government retains and the publisher, by accepting the article for publication, acknowledges that the United States Government retains a non-exclusive, paid-up, irrevocable, world-wide license to publish or reproduce the published form of this manuscript, or allow others to do so, for United States Government purposes. The U.S. Department of Energy will provide public access to these results of federally sponsored research in accordance with the DOE Public Access Plan (http://energy.gov/downloads/doe-public-access-plan). DOE/NV/25946—2924. I would also like to thank Dr. Cameron Hawkins, Dr. Ed Daykin, Michael Peña, Dr. Robert Hixson, Zach Fussell, Austin Daykin, and Michael Heika for their help and support throughout the project.

Finally, I offer my regards and love to my family, my boyfriend, and all of those who supported me in any respect during the completion of the project.

TABLE OF CONTENTS

ABSTRACT iii

ACKNOWLEDGEMENTS v

TABLE OF CONTENTS vi

LIST OF TABLES ix

LIST OF FIGURES x

1. INTRODUCTION 1

1.1 LITERATURE REVIEW 1

1.2 RESEARCH HYPOTHESIS 8

1.3 RESEARCH OBJECTIVES 9

2. EXPERIMENTAL SETUP 11

2.1 UNLV's TWO-STAGE LIGHT GAS GUN 11

2.1.1 POWDER BREECH AND PUMP TUBE 13

2.1.2 GAS HANDLING SYSTEM 15

2.1.3 CENTRAL BREECH AND LAUNCH TUBE 18

2.1.4 BLAST TANK, DRIFT TUBE, AND TARGET CHAMBER 20

2.2 INSTRUMENTATION 23

2.2.1 PROJECTILE VELOCITY MEASUREMENT 23

2.2.2 PHOTONIC DOPPLER VELOCIMETRY (PDV) 25

2.3 MATERIALS 27
2.3.1 FORGED TITANIUM ALLOY 29
2.3.2 EBAM TITANIUM ALLOY 29
2.4 EXPERIMENTAL SETUP FOR HYPERVELOCITY IMPACT EXPERIMENTS 31
2.4.1 TARGET PLATES CONFIGURATIONS 31
2.4.2 TARGET HOLDER CONFIGURATIONS 32
2.5 OPTICAL MICROSCOPY 33
3. EXPERIMENTAL RESULTS 35
3.1 PHYSICAL OBSERVATIONS 35
3.2 MICROSCOPIC RESULTS 49
3.3 FREE SURFACE VELOCITY 50
4. FINITE ELEMENT ANALYSIS 56
4.1 SOFTWARE AND HARDWARE 56
4.2 SMOOTHED PARTICLE HYDRODYNAMICS (SPH) 57
4.3 MODEL DESIGN 57
4.4 JOHNSON-COOK MATERIAL MODEL 59
4.5 MIE-GRÜNEISEN EQUATION OF STATE (EOS) 60
4.6 HUGONIOT ELASTIC LIMIT (HEL) AND SPALL STRENGTH ESTIMATION CALCULATION 62
4.7 SIMULATION DAMAGE RESULTS 65

4.8 SIMULATION VELOCIMETRY RESULTS 77

5. DISCUSSION 83

5.1 PHYSICAL CHARACTERISTICS COMPARISON BETWEEN TARGETS 83

5.2 FREE SURFACE VELOCITY PROFILE COMPARISON BETWEEN TARGETS... 84

5.3 LS-DYNA® SIMULATION FREE SURFACE VELOCITY COMPARISON 85

6. CONCLUSIONS AND FUTURE WORK 86

APPENDIX A. GRAPHICAL REPRESENTATION OF PDV PROBE LOCATIONS 90

APPENDIX B. ALL VELOCITY TRACES 101

FORGED TITANIUM- 12.7 MM THICK 101

FORGED TITANIUM-TWO 6.35 MM STACKED PLATES 105

FORGED TITANIUM-4 3.2 MM STACKED PLATES 107

ADDTIVELY MANUFACTURE TITANIUM-12.7 MM THICK..... 109

APPENDIX C. PARTICLE SPACING STUDY..... 114

APPENDIX D. SAMPLE LS-DYNA® CODE..... 116

REFERENCES 120

CURRICULUM VITA 126

LIST OF TABLES

Table 2.1: Typical Chemical Composition of Titanium Alloy (%) Composition by Weight..... 28

Table 2.2: Mechanical Properties of Titanium Alloy 28

Table 2.3: Densities of target materials 31

Table 3.1: Deformation results single-layer forged targets 36

Table 3.2: Deformation results two-layer forged targets 36

Table 3.3: Deformation results four-layer plate forged targets..... 37

Table 3.4: Deformation results of AM targets 37

Table 3.5: Target descriptions, velocity ranges, and probe locations 52

Table 4.1: Simulation Dimensions..... 58

Table 4.2: Johnson-Cook Material Properties 60

Table 4.3: Mie- Grüneisen parameters..... 61

Table 4.4: Forged titanium HEL and spall strength estimation 64

Table 4.5: AM 'C' HEL and spall strength estimation 64

Table 4.6: Forged 2-layer HEL and spall strength estimation 64

Table 4.7: Simulation and experimental deformation values for forged titanium alloy 67

Table 4.8: Simulation and experimental deformation values for AM 'C' 71

Table 4.9: Experimental and simulation deformation values for layered forged titanium alloy .. 76

LIST OF FIGURES

Figure 1.1: Typical frequency spectrogram with user define ROI 6

Figure 2.1: UNLV's two-stage light gas gun with SolidWorks® schematic 12

Figure 2.2: Piston with O-ring 12

Figure 2.3: Cap breech and firing solenoid 13

Figure 2.4: Firing station 14

Figure 2.5: Powder breech 14

Figure 2.6: Cartridge pre- and post-experiment 14

Figure 2.7: Pump tube 15

Figure 2.8: Gas Panel 16

Figure 2.9: Gas cylinder storage 16

Figure 2.10: Manual gas valves 17

Figure 2.11: Vacuum Pump 17

Figure 2.12: a) Central breech b) central breech launch tube end c) central breech with petal valve d) central breech pump tube end 18

Figure 2.13: Used piston deformed into conical shape 19

Figure 2.14: Petal valve pre- and post- experiment 19

Figure 2.15: a) Projectile length b) Projectile diameter 19

Figure 2.16: Launch tube 20

Figure 2.17: Blast tank 21

Figure 2.18: Drift tube 21

Figure 2.19: Target chamber 22

Figure 2.20: a) Side diagnostic port b) Top diagnostic port 22

Figure 2.21: Laser intervalometer 24
Figure 2.22: Digital readout of laser intervalometer 24
Figure 2.23: Schematic of PDV system 25
Figure 2.24: Linear mechanical transfer array 27
Figure 2.25: Experimental targets (a) one 0.5" thick plate, (b) two 0.25" thick stacked plates, (c) four 0.125" thick stacked plates 29
Figure 2.26: As shipped EBAM material 30
Figure 2.27: Machined AM preforms 31
Figure 2.28: New target holder configuration 33
Figure 2.29: Polishing Preparation 34
Figure 3.1: Deformation vs. impact velocity for forged 12.7mm Ti plate at velocities of (a) 4.838 km/s, (b) 5.655 km/s, (c) 6.145 km/s, and (d) 6.612 km/s 38
Figure 3.2: Deformation vs. impact velocity for AM 'A' 12.7 mm Ti plate at velocities of (a) 5.175 km/s, (b) 5.552 km/s, and (c) 5.976 km/s 39
Figure 3.3: Deformation vs. impact velocity for AM ‘B’ 12.7 mm Ti plate at velocities of (a) 5.255 km/s, (b) 5.613 km/s, and (c) 6.08 km/s 39
Figure 3.4: Deformation vs. impact velocity for AM ‘C’ 12.7 mm Ti plate at velocities of (a) 5.14 km/s, (b) 5.634 km/s, and (c) 5.907 km/s 39
Figure 3.5: AM ‘A’ shows severe shear failure at 5.976 km/s 39
Figure 3.6: Deformation vs. impact velocity for 2-layer plates at velocities of (a) 5.6 km/s (b) 6.2 km/s (c) 6.7 km/s 40
Figure 3.7: Deformation vs. impact velocity for 4-layer plates at velocities of (a) 5.1 km/s, (b) 5.603 km/s, (c) 6.773 km/s 40

Figure 3.8: Velocity vs. crater diameter trends (a) Forged Ti, (b) AM ‘A’ Ti, (c) AM ‘B’ Ti, (d) AM ‘C’ Ti, (e) 2-layer (f) 4-layer 42
Figure 3.9: Single layer plate velocities vs. penetration depth (a) Forged Ti (b) AM ‘A’ Ti (c) AM ‘B’ Ti (d) AM ‘C’ Ti..... 44
Figure 3.10: Multi-layer sample velocities vs. penetration depth (a) 2-layer (b) 4-layer..... 45
Figure 3.11: Single layer plate impact velocities vs. back surface bulge (a) Forged Ti (b) AM 'A' Ti (c) AM 'B' Ti (d) AM 'C' Ti..... 47
Figure 3.12: Multi-layer plate impact velocities vs. back surface bulge (a) 2-layer (b) 4-layer .. 48
Figure 3.13: AM 'C' sample 49
Figure 3.14: Am 'C' Sample at v~5.6 km/s 50
Figure 3.15: a) AM comparison at v ~5.1 km/s b) AM comparison at v~5.5 km/s c) AM comparison at v~6.0 km/s 53
Figure 3.16: Comparison of forged, AM, and layered material at v~ 5.5 km/s..... 54
Figure 3.17: Comparison of forged and AM titanium alloy at v~ 6 km/s 55
Figure 4.1: Typical 2-D axis-symmetric model 59
Figure 4.2: Experimental HEL and spall strength calculation from velocimetry curve 63
Figure 4.3: Spall study on forged titanium alloy 65
Figure 4.4: Typical damage results in single-layer simulation 66
Figure 4.5: Spall formation in single layer simulation 66
Figure 4.6: Simulation vs. experimental values for crater diameter for forged titanium alloy..... 68
Figure 4.7: Simulation vs. experimental values for penetration depth of forged titanium alloy .. 69
Figure 4.8: Simulation vs. experimental values for back surface bulge for forged titanium alloy70
Figure 4.9: Simulation vs. experimental values for crater diameter for AM 'C'..... 72

Figure 4.10: Simulation vs. experimental values for penetration depth for AM 'C' 73

Figure 4.11: Simulation vs. experimental values for back surface bulge for AM 'C' 74

Figure 4.12: 2-Layer simulation 76

Figure 4.13: 4-Layer simulation 77

Figure 4.14: Simulation of forged 12.7 mm free surface velocity trace 78

Figure 4.15: Simulation of AM 'C' free surface velocity trace 78

Figure 4.16: Forged and AM 'C' simulation comparison of free surface velocity at about 5.1 km/s 79

Figure 4.17: Forged and AM 'C' simulation comparison of free surface velocity at about 5.9 km/s 80

Figure 4.18: 2-layer simulation of free surface velocity results 81

Figure 4.19: 4-layer simulation of free surface velocity results 82

Figure A.1: Shot 2 probe locations 90

Figure A 2: Shot 3 probe locations 90

Figure A.3: Shot 4 probe locations 91

Figure A.4: Shot 5 probe locations 91

Figure A.5: Shot 6 probe locations 92

Figure A 6: Shot 7 probe locations 92

Figure A.7: Shot 8 probe locations 93

Figure A 8: Shot 9 probe locations 93

Figure A.9: Shot 10 probe locations 94

Figure A.10: Shot 11 probe locations 94

Figure A 11: Shot 12 probe locations 95
Figure A.12: Shot 13 probe locations 95
Figure A.13: Shot 14 probe locations 96
Figure A.14: Shot 15 probe locations 96
Figure A.15: Shot 16 probe locations 97
Figure A.16: Shot 17 probe locations 97
Figure A.17: Shot 18 probe locations 98
Figure A.18: Shot 19 probe locations 98
Figure A.19: Shot 20 probe locations 99
Figure A.20: Shot 21 probe locations 99
Figure A.21: Shot 22 probe locations 100
Figure A.22: Shot 23 probe locations 100

Figure B.1: Shot 1 velocity trace forged titanium 4.8 km/s 101
Figure B.2: Shot 2 velocity trace forged titanium 5.2 km/s 102
Figure B.3: Shot 3 velocity trace forged titanium 5.5 km/s 102
Figure B.4: Shot 4 velocity trace forged titanium 5.7 km/s 103
Figure B.5: Shot 13 velocity trace forged titanium 6.1 km/s 103
Figure B.6: Shot 19 velocity trace forged titanium 6.6 km/s 104
Figure B.7: Shot 24 velocity trace forged titanium 6.6 km/s 104
Figure B.8: Shot 6 velocity trace 2-layer 5.6 km/s 105
Figure B.9: Shot 7 velocity trace 2-layer 5.6 km/s 105
Figure B.10: Shot 20 velocity trace 2-layer 6.2 km/s 106

Figure B.11: Shot 17 velocity trace 2-layer 6.7 km/s 106
Figure B.12: Shot 8 velocity trace 4-layer 5.4 km/s 107
Figure B.13: Shot 9 velocity trace 4-layer 5.6 km/s 107
Figure B.14: Shot 21 velocity trace 4-layer 6.2 km/s 108
Figure B.15: Shot 18 velocity trace 4-layer 6.8 km/s 108
Figure B.16: Shot 5 velocity trace AM 'A' 5.2 km/s 109
Figure B.17: Shot 10 velocity trace AM 'A' 5.5 km/s 109
Figure B.18: Shot 14 velocity trace AM 'A' 6.0 km/s 110
Figure B.19: Shot 2 velocity trace AM 'B' 5.3 km/s 110
Figure B.20: Shot 11 velocity trace AM 'B' 5.6 km/s 111
Figure B.21: Shot 15 velocity trace AM 'B' 6.1 km/s 111
Figure B.22: Shot 23 velocity trace AM 'C' 5.1 km/s 112
Figure B.23: Shot 12 velocity trace AM 'C' 5.6 km/s 112
Figure B.24: Shot 16 velocity trace AM 'C' 5.9 km/s 113

Figure C.1: Spacing study until 0.1 mm spacing 114
Figure C.2: Spacing study converges to 0.1 mm spacing 115

Figure D.1: Sample forged titanium alloy simulation code 116
Figure D.2: Sample AM titanium simulation code 117
Figure D.3: Sample 2-layer simulation code 118
Figure D.4: Sample 4-layer simulation code 119

1. INTRODUCTION

1.1 LITERATURE REVIEW

Scientists and engineers have been studying numerous components of hyper velocity impact (HVI) for several decades because of its importance in many areas including spacecraft design and the effects of high explosive on structures. HVI creates high temperatures and pressures in both the target and the projectile over an extremely short time period inducing high strain-rates in the target material. “Dynamic properties” refer to those mechanical and physical characteristics of the target which are affected by the extreme loading rates, temperatures, and pressures [5]. During a high velocity event, it becomes necessary to understand what is taking place on the microstructural level to help determine unique defects that will cause the material to fail. For example, a perfectly homogenous metallic sample would have a repetition of the particular lattice arrangement of the metal. However, during a hyper-velocity event, the metallic target will behave in liquid-like form and when the target finally solidifies after the end of the HVI event, an assortment of imperfections are formed [6]. These microstructural flaws can cause a variety of failures on a macroscopic level. Some of these defects include; spalling, petalling, discing, and plugging [5] (Figure 1.2, Rosenburg, Terminal Ballistics). These different failure mechanisms are based upon several different features like geometry of the projectile, the material properties of the target, and the projectile impact-velocity. Extensive research in the field of characterizing the dynamic response of homogenous metals has been conducted with much success [7 – 9].

The focus of this study is to understand the effects of HVI on titanium, specifically Ti6Al4V alloy. Ti6Al4V is the most commonly used titanium alloy and accounts for 50% of

total titanium usage in the world [10]. The chemical composition of Ti-6Al-4V is shown in Table 2.1. Due to exceptionally high strength-to-weight ratio, Ti6Al4V is extensively used in aerospace applications and nuclear industries. Recently, Additive Manufacturing (AM) techniques were introduced, bringing the potential of creating complex parts quickly and on demand. AM techniques have the potential for tailoring geometry and optimizing structural performance, in addition to minimizing the amount of material wasted for odd shaped parts and thereby reducing cost. However, there are many unanswered questions related to the effect of using AM techniques with titanium alloys, especially under shock conditions. A possible way of understanding the behavior of an AM plate is to compare its behavior with that of a forged single plate and stacked plates, with the same thickness, under similar loading conditions.

Recent research has led to an increased understanding of the mechanical behavior of AM metals. Quasi-static analysis of AM titanium shows only 3%-5% lower mechanical properties than that of a forged counterpart [11- 12]. Researchers studied the mechanical characteristics of AM metallic components under static loading conditions, which revealed that there was scatter in mechanical properties for wire-feed deposits, even some heat treatments were not useful for enhancing the strength and ductility [13]. Some dynamic loading conditions have been studied [14] showing more dense specimens exhibit superior strength. However, the behavior of AM metals under high-velocity impact conditions has not been studied.

A possible way of comparing the AM titanium alloy is to study homogenous layered titanium. Layered materials have a myriad of functions in many disciplines of engineering; including, the use of innovative composite laminates in the aerospace field, armoring, and complex elements of nuclear weapons. Studies were conducted on the ballistic performance of single-layer and multi-layered aluminum plates that were impacted by different end types of

projectiles [15]. It was discovered, that the in-contact multi-layered plates were weaker compared to that of single-layer plates of the same thickness. A similar study conducted impact experiments on steel plates hit by ordinary bullets to explore the outcome of target arrangement on the penetration performance [16]. It was determined that single-layer plates had less damage than multi-layered plates of corresponding thickness. Failure mechanisms of layered-materials subject to static-loading have been studied recently [17], as well as some of their dynamic counterparts [18-19] have been considered. A steady-state analysis was found to be the best way of designing against fractures in layered materials [17]. Dynamic testing of layered composite materials showed delamination failure was the main failure mode at the back surface of the target, while in the main failure mode in the middle and front of the target was tensile failure [18-19]. Layered metals could have these similar failure properties.

The two stage light-gas gun [1-2] is a widely used tool for studying HVI effects. This gun can accelerate a projectile to generate a shock wave in a target similar to micrometeorite impact [3]. Swift [4] surveyed, from a historical context, the needs for the development of this type of gun.

There has been a lack of proper diagnostic equipment to obtain reliable dynamic responses from these experiments. Development of diagnostic equipment for hyper-velocity impact has focused on capturing velocimetry data. Velocimetry data can be used to characterize spall strength, the equation of state, and the Hugoniot Elastic Limit (HEL) of materials [5]. Velocimetry data, if captured correctly, can lead to the development of accurate computational models for materials. The subsequent paragraphs will provide a short synopsis of velocimetry capturing diagnostic techniques.

Researchers studying HVI have only a fraction of a second (5 – 20 microseconds) to reveal useful data about the target material. Before the more popular laser interferometry methods, shorting pins were used to determine the velocity of the shock waves [19]. This technique, although still used today, is not useful for determining any dynamic material properties and the pins could possibly be destroyed after every experiment depending on the test [20]. In the 1950's, 1-D optical imaging was used to define the EOS of materials [21]. Streak cameras were used for imaging a 1D slit and flash the image of that slit across a recording device (CCD or film) to get a time history and as a result an EOS can be determined. The need for better diagnostic tools to understand dynamic material properties resulted in a few discoveries that later led to the use of laser interferometry.

The basics of laser interferometry start with shining a laser light on a back surface of a moving target. The light is then reflected and is Doppler-shifted in frequency. This procedure detects this phase shifted light relative to the reference light (heterodyne), or a time-delayed duplicate of itself (homodyne) [22]. A heterodyne interferometer produces fringes (difference in intensities of light) when the path length between the beams of light change, thus it becomes clear that it is a position interferometer. On the other hand, a homodyne interferometer produces fringes when there is a difference in frequency (velocity) over an identified time-delay, thus a velocity interferometer. It wasn't until 1965, when Barker and Hollenbach [23] first used a laser heterodyne interferometer to determine a velocity curve; that velocimetry data became the main technique for characterizing materials during hyper-velocity impact. This basic technique, had many setbacks including; the need to replace after every experiment, a mirrored finish on target surface, and little tilt in the target surface to get accurate data.

These setbacks, among many others, resulted in the development of a homodyne interferometric system, Velocity Interferometer System for Any Reflector (VISAR), in 1972 [24]. VISAR works by using the Doppler-shifted reflected light that produces fringes in the interferometer, and the number of fringes is proportional to the surface's velocity. One advancement in accuracy integrated into the VISAR, that had not been previously used, is the concurrent monitoring of two fringe signals which are 90° out of phase. The improvement gained from recording two signals that are 90° out of phase can be appreciated by noting that a plot of the interferometer's output light intensity vs. the fringe count is a simple sine wave. Thus, the derivative of intensity with respect to fringe gives an intensity maxima and minima. VISAR, although incredibly precise (1-2% accuracy), is costly, intricate, and not suitable for determining multiple velocities.

These limitations of VISAR, created a need for better diagnostics techniques that were easier to use and more cost effective. Strand et al. in 2006 [25], developed a diagnostic setup from "off-the-shelf telecommunications components" that was more robust than VISAR. This diagnostic system is called Photon Doppler Velocimetry (PDV). PDV is a heterodyne laser interferometer system that measures the beat frequency of coherent laser light to determine measuring position using fiber optic probes. PDV is an advancement in HVI studies because it is relatively simple and more robust. The PDV probe focuses the light onto the back surface of a plate and analyzes the Doppler-shifted light that is returned back [26]. The reflected light from a moving surface is joined with the light from a reference beam (typically a near infrared wavelength) producing fringes, each of which relate to the displacement of the surface. The measured data is recorded as a voltage and must be converted to a usable velocity trace.

The most common way of analyzing PDV data is to ablate a windowed signal (typically Hamming) and taking a Fast Fourier Transform (FFT) creating a frequency spectrogram [27]. Then, the user outlines a region of interest (ROI) in the spectrogram. Figure 1.1, shows a spectrogram, of a typical experiment that will later be described in Chapter 2, with a user defined ROI. The red in the spectrograph represents a strong signal conversely, the yellow symbolizes a weak signal. The straight red line along the bottom of the signal is the baseline added to the signal to upshift so that a non-movement of the surface relates to a beat frequency greater than 0.

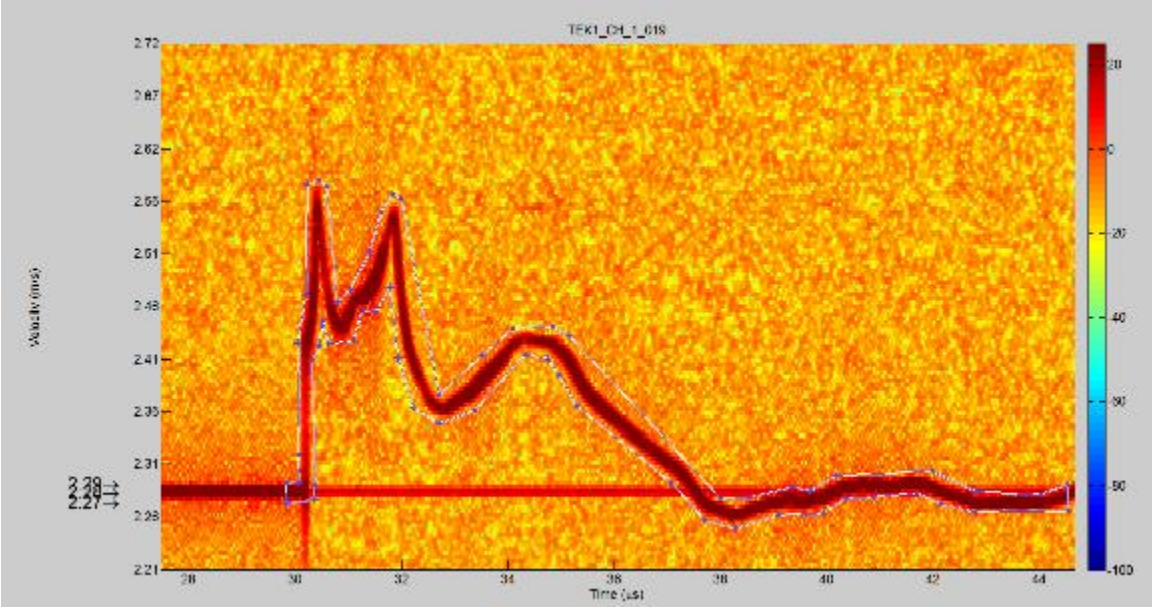

Figure 1.1: Typical frequency spectrogram with user define ROI

After the user has defined the ROI there are many different methods for analyzing the velocity using the spectrogram for different purposes, but the different approaches take methods that deviate from each other. There is no collective decision on which velocity extracting techniques, or class of methods, yields the best results. However, there has been substantial work to advance these techniques over the past few years [28-29]. The method that is being considered for this work is the Interpolated Fast Fourier Transform Method (IpFFT). This method, initiates a

dispersal to smooth the results [28]. This methodology is local in time, frequency-based, and is one of the most commonly used methods for PDV analysis.

Even though diagnostic equipment costs have improved with the utilization of PDV, the expenses associated with hypervelocity impact are significant. Computational modeling and numerical simulations have become a conventional way to examine behavior of materials during these impact events. The objective of using computational models is to predict the outcome of several types of events with limited error to reduce costs of unnecessary experiments. A major objective of this work is to create a reasonable model for the behavior of the forged, layered, and AM titanium under HVI conditions.

The following will be a brief overview of research in the field of computational modeling for HVI. Due to the extreme nonlinearities and great distortion, the HVI simulation is a complex job for numerical modeling. Two primary structures for explaining the distortion of the material exist: the Lagrangian characterization and the Eulerian characterization [30]. In the Lagrangian characterization, the mesh is fixed and distorts with the material area. The material shows no convective properties thus, the boundary conditions at free surfaces change the borders and material boundaries, which are computationally executed. This method works best for time-dependent material. However, this technique is limited if the distortion is extremely large, as in HVI, mesh deformation and element enmeshment. Conversely, in the Eulerian characterizing, the material moves through a grid stationary in space. It totally circumvents element deformations, but still complications in tracing the distortion history of a material exist and it has issues with the material interfaces. The Eulerian technique has a significant issue connected with mass flux among adjacent elements. There has also been mixed Eulerian- Lagrangian methods developed such as the Arbitrary Lagrangian-Eulerian (ALE) method [31], but still difficulties

with maintaining mesh regularities exist. Mesh-free methods were soon developed and use distinct points to make exploratory functions, so that the complications accompanying mesh distortions can be circumvented or improved [32-33]. Still, most of the mesh-free approaches suffer from high computational times and the precision is based on node regularities to a certain extent. There are some mesh-free methods that are preferred for HVI because they can capture some of the complexities of the materials during experiment.

A mesh-free method that is used extensively in HVI is Smoothed Particle Hydrodynamics (SPH). SPH is a Lagrangian particle method initially invented to explain astrophysical problems [34-35]. SPH is particularly useful because the movement of the particles mimics the flow of liquids or gases. These particles are capable of moving in space and transport the computational information. This creates the basic equations to solve the partial differential equations (PDEs) illustrating the conservation law of continuum fluid dynamics [36]. This is attractive to the field of modeling HVI because shock waves propagating through materials behave like fluids [37]. SPH has been acquiring a reputation for modeling impact penetration problems [38-40]. Some of the researchers concentrated on modeling the behavior of ceramic tiles under HVI, but the literature also provided valuable experimental statistics and computational material model properties for some metallic materials. More recently, studies have been conducted on modeling plastic deformation of steel plates during HVI [7-9]. The researchers outline an experimental approach to collecting and analyzing valuable data to input into computational models.

1.2 RESEARCH HYPOTHESIS

The current literature has provided a good foundation on an experimental approach to study plastic deformation on steel plates. However, there are many unanswered questions related to the effect of using AM techniques with titanium alloys, especially under shock conditions. I

propose that the processes used to create AM affect the behavior of the components, especially in the interface between streams. Another postulate is that due to the complexity of the processes of the AM, the AM part cannot be modeled as 2D axis-symmetric. The following section will outline research objectives needed in order to verify the hypothesis.

1.3 RESEARCH OBJECTIVES

To verify the above hypothesis, this research will pursue two objectives:

(a) Develop an experimental approach to measure the plastic deformation of AM plates impacted by projectiles with a two-stage gas gun at speeds ranging between 3-7 km/s. A multi-channel PDV system will measure the resulting deformation on the back surface of the plates. A range of velocities is needed to study failure mechanisms in the titanium.

(b) Develop a computational approach to simulate these experiments using a smoothed-particle hydrodynamics (SPH) solver within LS-DYNA® software [41]. SPH is a mesh-free Lagrangian-based modeling approach. These simulations can help understand the material models and equations of state (EOS) for these unique metals.

To accomplish all of the objectives, the effort has been divided into subsections:

1. Conduct a series of HVI experiments with different Titanium plate configurations
2. Quantitative measurement of target plates after experiment
3. Analyze raw PDV data to usable velocimetry data
4. Evaluate velocimetry data
5. Develop a computational model for forged Ti6Al4V
    a. Develop the model for a 2-layer configuration
    b. Develop the model for a 4-layer configuration

6. Compare data from forged Ti6Al4V with AM
7. Develop an approach to simulate AM Ti6Al4V

2. EXPERIMENTAL SETUP

This work will focus on hypervelocity impact on titanium plates. All experiments performed at UNLV were conducted using a two-stage light gas gun that was manufactured by Physics Application Incorporated. Two-stage light gas gun theory and design is outside the extent of this effort [1-4]. This chapter includes an introduction of how the gas gun operates, design of the experiment to impact various titanium alloy plates at hypervelocities using a two stage light-gas gun, and the necessary diagnostic equipment to run these experiments.

2.1 UNLV's TWO-STAGE LIGHT GAS GUN

A series of hyper-velocity impact experiments were conducted by means of UNLV's two-stage light gas gun. The main components of the two-stage light gas gun are depicted in Figure 2.1. The main subsystems are the powder breech, pump tube, central breech, launch tube, blast tank, drift tube, and the target chamber. The gun is activated through the electric ignition of powder inside the powder breech (Section 2.1.1), which forces a plastic piston (Figure 2.2) into a pump tube that is filled with a light gas such as hydrogen, helium, or nitrogen at a specific pressure. This gas is compressed as the piston travels from one end of the pump tube to the other end. Eventually, the pressure reaches a critical value that forces the rupture of a petal valve that separates the pressurized gas from the launch tube. The petal valve is placed inside the central breech and when the petal valve ruptures it accelerates a projectile, which is placed at the beginning of the 1.016 m launch tube and into the target chamber. The projectile is a Lexan™ cylinder. The dimensions and mass of the piston and projectile are provided in Table 2.1. The projectile impacts the target plate, which is bolted to a mounting plate, inside the target chamber at velocities between 4.8 and 6.9 km/s.

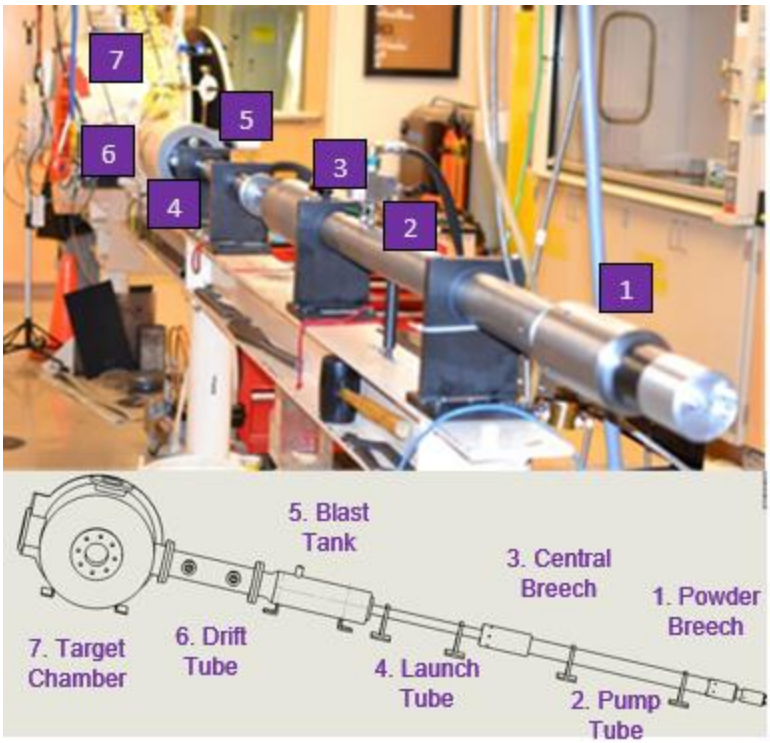

Figure 2.1: UNLV's two-stage light gas gun with SolidWorks® schematic

Figure 2.2: Piston with O-ring

Table 2.1 Piston and Projectile Dimensions and Mass

	Diameter (mm)	Length (mm)	Mass (grams)
Piston	20	120	28.8
Projectile	5.6	8.6	0.25

2.1.1 POWDER BREECH AND PUMP TUBE

A high voltage capacitor discharges, triggering a solenoid located inside the cap breech (Figure 2.3) which activates the firing solenoid pin to impact the cartridge primer. The capacitor is charged through the keyed firing station (Figure 2.4), switching the two buttons in opposite direction until the voltage reaches 20 V, and pressing the “fire” button. The powder breech (Figure 2.5) holds a varied quantity of IMR 4064 gun powder (17-23 g), which scorches seemingly instantaneously after firing. The gun powder is burned by electrically igniting a primer on the back surface of a .223-caliber (5.56×45 mm) cartridge casing (Figure 2.6). Typically, the cartridge melts during experiment and an anti-seize is placed on the cartridge pre-experiment to ensure it does not damage the powder breech. The cartridge is also filled with a charge of 0.6 g of a Green-Dot smokeless powder. Then the cartridge is placed to seal one of the two openings on the powder breech.

Figure 2.3: Cap breech and firing solenoid

Figure 2.4: Firing station

Figure 2.5: Powder breech

Figure 2.6: Cartridge pre- and post-experiment

The resulting blast shears the piston and propels it into the pump tube (Figure 2.7) which is filled with pressurized diatomic hydrogen gas. In all of the experiments, the pump tube was filled to 2.41 MPa (350 psig). This pressure is considered to be the operating pressure and gun powder variance will result in the safest way to change the velocity for the experiments. Pre-experiment it is necessary to evacuate the pump tube by using a vacuum pump, this safeguards the reliability of the gun's dynamics.

Figure 2.7: Pump tube

2.1.2 GAS HANDLING SYSTEM

The gas panel (Figure 2.8) allows the user to perform a multitude of tasks while operating the gas gun. The operator can evacuate the pump tube, fill the pump tube with gas, and vent the fumes post-experiment. The control panel has three gauges for monitoring:

- Gas tank
- The gas inside the pump tube

- Vacuum pressure

On the control panel the user can choose Hydrogen, Helium, or Nitrogen gas. Helium was used to perform a leak test (ensures the system is operational). In this research, Hydrogen is used to fill the pump tube for all the experiments. All gas cylinders (Figure 2.9) are connected to the gas panel and the pump tube using high pressure hoses, this helps ensure the reliability of operation. In order to place the Helium and Hydrogen gas into the pump tube, manual valves (Figure 2.10) are used.

Figure 2.8: Gas Panel

Figure 2.9: Gas cylinder storage

Figure 2.10: Manual gas valves

The vacuum pump (Figure 2.11) is also linked to the gas management system. In order to control the whole system, a pressure regulator is turned. During the experiment, noxious gas is produced so a vent valve is utilized in the gas control panel that is operated to expel the system of those noxious fumes or it can be used in case of an emergency.

Figure 2.11: Vacuum Pump

2.1.3 CENTRAL BREECH AND LAUNCH TUBE

The central breech is an integral part of the two-stage light gas gun. The central breech (Figure 2.12) connects the pump tube to the launch tube. The pump tube side of the central breech is 20 mm and then tapers down to 5 mm. On the launch tube side of the central breech, a petal valve opens until a critical point is reached and releases the pressurized gas to propel the projectile into the launch tube and on to the rest of the system. The piston is stopped by the taper, where the residual kinetic energy of the piston is dissipated by the front end of the piston, transforming into a conical shape (Figure 2.13), and by the friction between the piston and the inner walls of the central breech [42].

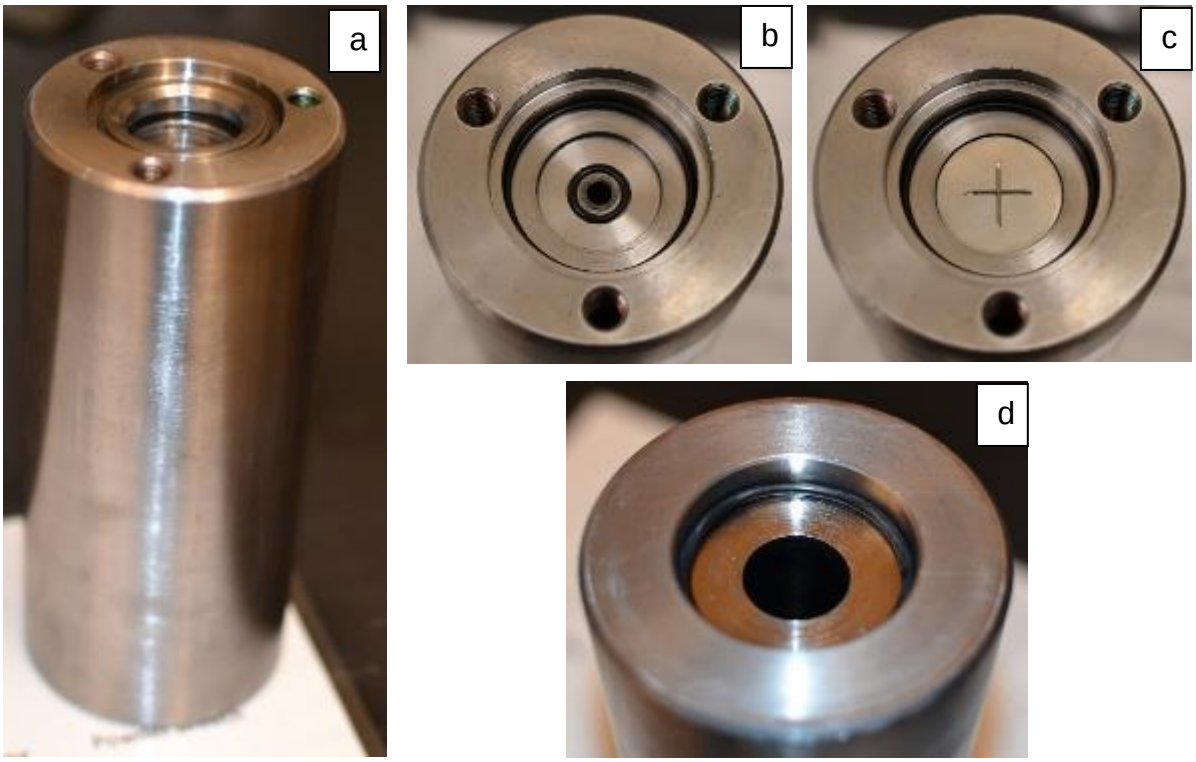

Figure 2.12: a) Central breech b) central breech launch tube end c) central breech with petal valve d) central breech pump tube end

Figure 2.13: Used piston deformed into conical shape

As mentioned earlier, the petal valve (Figure 2.14) will burst at a certain pressure and propel the projectile (Figure 2.15) down the launch tube (Figure 2.16). Since the pressure behind the petal valve is dynamic, it is challenging to find the actual burst pressure of the valve. All parts of the central breech are lined with O-rings to prevent leaking of gases during experiment.

Figure 2.14: Petal valve pre- and post- experiment

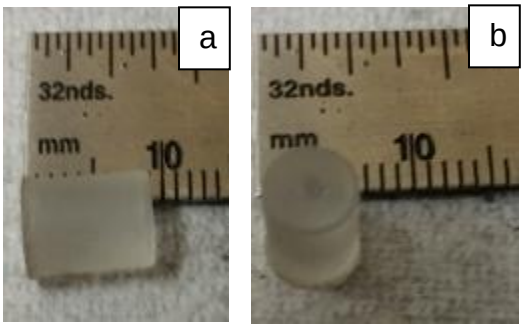

Figure 2.15: a) Projectile length b) Projectile diameter

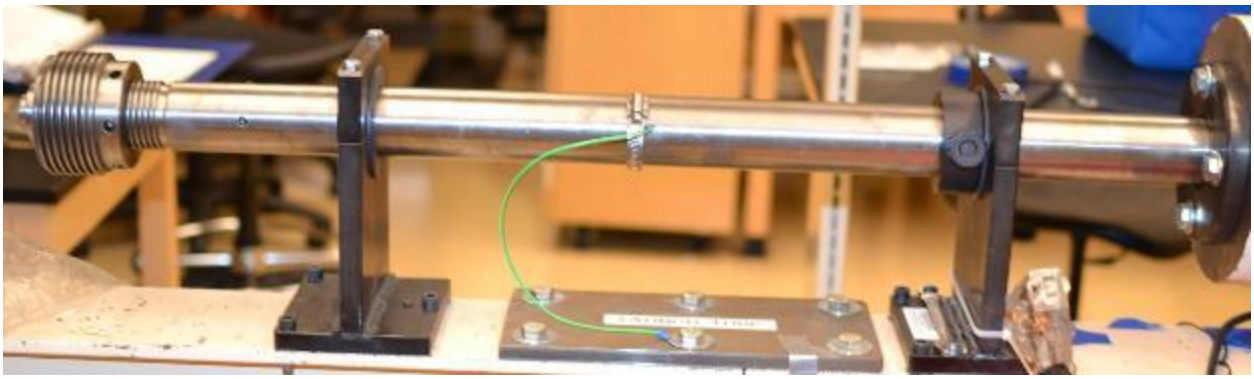

Figure 2.16: Launch tube

The same Lexan™ projectile was used in all experiments. Lexan™ is a polycarbonate amorphous thermoplastic, which is easily worked and molded. The projectile also acts like a greasing agent while it is propelled down the launch tube. The inner walls of the launch tube are rifled. Rifling is a helical groove that is purposefully placed in most guns to spin the projectile. The spin that is placed on the projectile improves the stability of the projectile and increases its accuracy.

2.1.4 BLAST TANK, DRIFT TUBE, AND TARGET CHAMBER

After the projectile reaches the end of the launch tube it starts to propel down the blast tank (Figure 2.17). The blast tank is roughly 0.228 m in diameter and 0.812 m in length. It is a heavy walled vessel capable of withstanding the expansion of the gases that are flowing behind the projectile. The blast tank is bolted to the drift tube (Figure 2.18) where an intervalometer (further details are included in Section 2.2.1) measures the projectile's velocity through two translucent windows. Drift tube is roughly 0.152 m diameter and 0.609 m length.

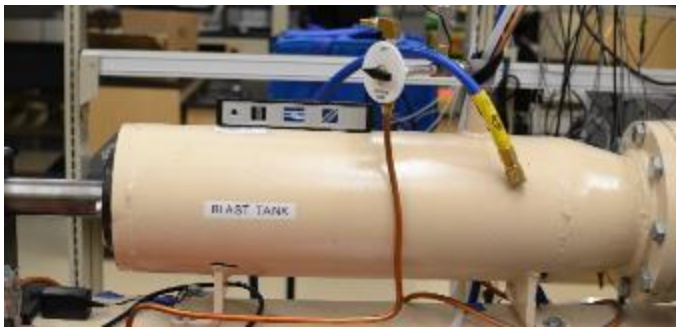

Figure 2.17: Blast tank

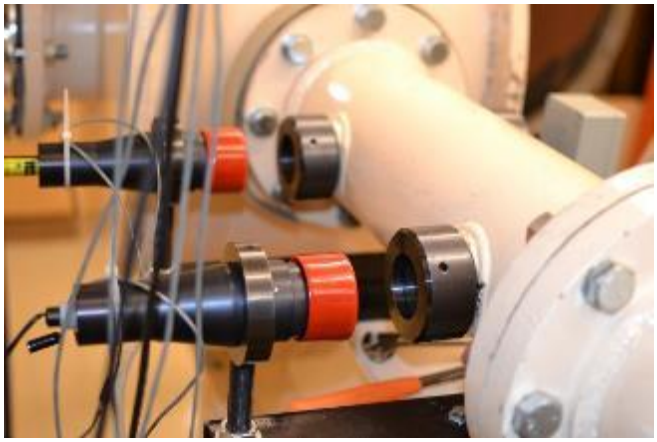

Figure 2.18: Drift tube

After the projectile passes through the drift tube, it impacts the target mounted inside the target chamber (Figure 2.19). The target chamber has a space for mounting the target into place and has space for instrumentation. Access points in the target tank, called ports (Figure 2.20), provide a way to use various instrumentation. The side port can be replaced with a translucent port for high speed video and the top diagnostic tank has a hole for fiber optic cables for experimental measurements. All openings in the tank assembly are compressing O-rings; the O-rings provide a way of sealing the tank off from atmospheric pressure and keeping the experimental gases contained.

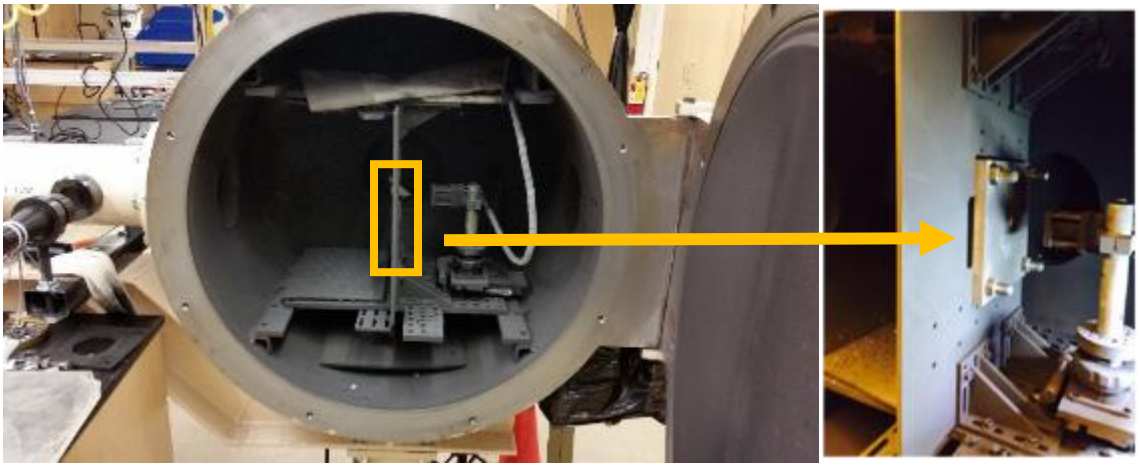

Figure 2.19: Target chamber

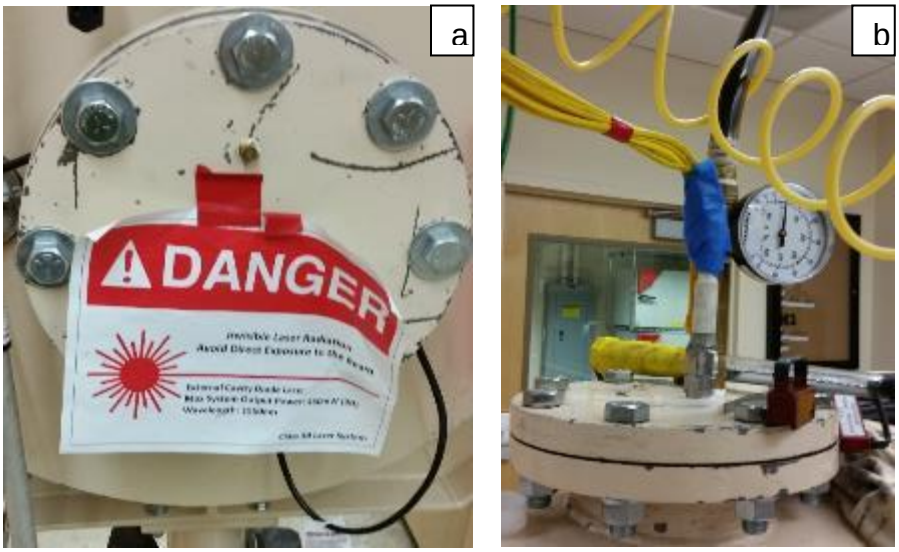

Figure 2.20: a) Side diagnostic port b) Top diagnostic port

Throughout the experiment, the target material is placed inside the target chamber and diagnostic equipment is assembled and tested. Once, this is complete the target chamber will be closed and systematically, according to a check list, the central breech, launch tube, pump tube, powder breech, and the cap breech are assembled together. The entire two-stage light gas gun is

evacuated and brought down to about 4 mm Hg. A leak test is completed to ensure the pump is properly functioning.

Once the vacuum has reached the appropriate level, the pump tube is filled with 2.41 MPa of diatomic hydrogen, powder is loaded and the powder breech is placed on the end of the pump tube. Then the cartridge is filled and placed in the powder breech, the cap breech is placed on the end of the powder breech, and a high voltage cable is attached to the cap breech. After this is completed the vacuum pump is switched off and diagnostic equipment is armed and prepared to capture data. The very last step, the firing pin is placed to certain depth in the cap breech and the solenoid is electronically engaged from the firing station to fire the gas gun.

2.2 INSTRUMENTATION

2.2.1 PROJECTILE VELOCITY MEASUREMENT

Throughout the experiment it is necessary to measure projectile velocity to quantify the gun's capabilities. The projectile's velocity is calculated by operating a laser intervalometer system. The invervalometer consists of two collimated laser light sources 304.8 mm away from each other (Figure 2.21). The beams pass through one transparent port to a receiving station on the other side. These receivers generate and brighten a linear arrangement of thirty-two photodiodes. The laser intervalometer works like a beam break. The projectile is detected by the lack of light level on one or multiple photodiodes. The photodiode arrangement is equipped with a narrow bandpass and is filtered to the 670 nm wavelength which reduces interference from the ambient light. The diode arrangement extends to a length of 50.8 mm. A timer unit is used that has a six-digit counter which is started by an outside source START pulse and disabled until it receives a STOP signal. During the experiment, the 'start' pulse is activated by the projectile after it inhibits the first light source. When the projectile moves across the threshold of the

second laser unit source, the timer receives a ‘stop’ signal. The digital readout (Figure 2.22) displays the time difference of the projectile’s interference of the two laser light sources. The space in-between the lasers is fixed and known to be 1 foot; the projectile velocity is then calculated based on the digital readout value. The equation for calculating the velocity is,

$$\text{velocity (m/s)} = \frac{0.3048}{\text{time (s)}}.$$

Figure 2.21: Laser intervalometer

Figure 2.22: Digital readout of laser intervalometer

2.2.2 PHOTONIC DOPPLER VELOCIMETRY (PDV)

The way the Photonic Doppler Velocimetry device works has been explained by Strand et al. in 2006 [25]. Figure 2.23 shows a schematic on how the PDV laser system functions. First, a laser transmits through a multi-mode fiber to a probe. The probe illuminates the target with the laser light. Then, as the target moves, the reflected laser is Doppler-shifted. The probe lens accumulates some of the Doppler-shifted laser and the laser circulates back through the fiber. The Doppler-shifted laser is mixed with a portion of the original laser in a fiber-optic coupler and is detected by a laser detector. Typically the detector generates an electrical current corresponding to the Doppler-shifted laser light. This corresponds to a beat frequency directly proportional to velocity of the target as a function of time [43].

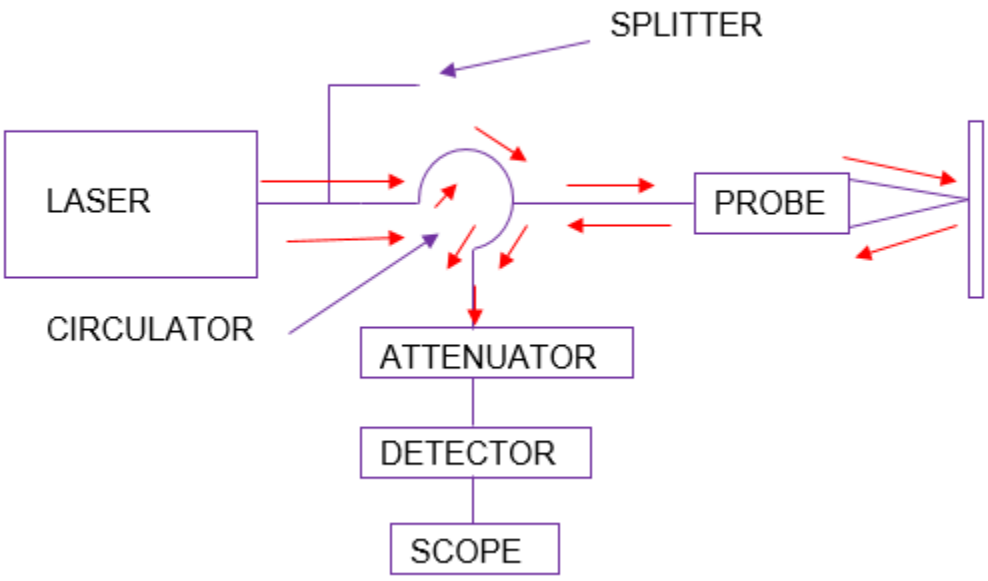

Figure 2.23: Schematic of PDV system

For this work, velocimetry data was taken from the back of the target plates with a four-channel PDV system. A 50.8 mm × 304.8 mm linear mechanical transfer (MT) array was

mounted in the target chamber with a distance of approximately 52 mm between the array and the back of each test plate (Figure 2.24). Four out of the total twenty-four available fibers in the array were utilized; resulting in four data collection points corresponding to the four-channel PDV system that was available for use. The system was originally set up for an MPDV system which was unavailable at the time of testing, therefore a four channel PDV was used in its place. The spacing between data collection points can be altered from shot to shot to provide better coverage of the impact zone of the target plates. The spacing was modified in order to achieve the best readings from the bulge on the back surface of the target plate. The spacing sizes used in the experiment are as follows:

- 1 mm – 1 mm – 1 mm,
- 2 mm – 2 mm – 3 mm, and
- 2 mm – 2 mm – 4 mm.

Figure 2.24: Linear mechanical transfer array

2.3 MATERIALS

Two materials were used for the experiments. Forged Titanium alloy (Ti6Al4V) and Electron Beam Additive Manufactured (EBAM) Titanium alloy of the same grade. The objective of this work is to compare forged titanium alloy and EBAM titanium alloy under HVI conditions. Currently, this grade of Titanium is used significantly in the aerospace and nuclear fields due to its high strength-to-weight ratio. AM technologies are especially important for these fields because it allows complex parts to be made quickly and reduce the cost of production and machining. However, since this technology is so new, it becomes an interesting engineering problem. The purpose of this work is to be able to quantify the differences between the forged

titanium alloy and the EBAM titanium alloy under HVI. There has been no recent research in this field because the material is so new.

The study was conducted on a well-tested metal, the forged titanium alloy, to understand the effects of the EBAM manufacturing process. The chemical composition of both materials are the same and are given in Table 2.1 with the mechanical properties given in Table 2.2. The mechanical properties of EBAM are 3%-5% lower than the forged material.

Table 2.1: Typical Chemical Composition of Titanium Alloy (%) Composition by Weight

Material	Ti6Al4V
Aluminum, Al	0-6
Vanadium, V	0-10
Iron, Fe	0-48
Molybdenum, Mo	0-6
Zirconium, Zr	0-4
Manganese, Mn	0-5
Tantalum, Ta	<1
Tin, Sn	0-5
Titanium, Ti	46-99

Table 2.2: Mechanical Properties of Titanium Alloy

Property	Forged Ti Alloy
Density (g/cc)	4.43
Tensile Strength, Ultimate (MPa)	950
Tensile Strength, Yield (MPa)	980
Young's Modulus (GPa)	109.8
Bulk Modulus (GPa)	41.9
Poisson's Ratio	0.31

2.3.1 FORGED TITANIUM ALLOY

All of the forged Titanium alloy products were purchased from Altemp Alloys Inc. All of the sheets were made to the SAE standard AMS 4911. The 12.7 mm thick target plate was originally cut to the dimension of 152.4 × 152.4 × 12.7 mm. Then, the dimensions were reduced to 76.2 x 76.2 x 12.7 mm to increase the number of experiments that could be completed with the same amount of material. A practice shot was performed to demonstrate that no edge effects were present during experiment at the smaller dimension. The two stacked 6.35 mm thick plates were cut to 152.4 × 152.4 × 6.35 mm. The four stacked 3.2 mm thick plates were cut to 152.4 × 152.4 × 3.2 mm. Figure 2.25 shows the standard setup in the experimental chamber with the different target types.

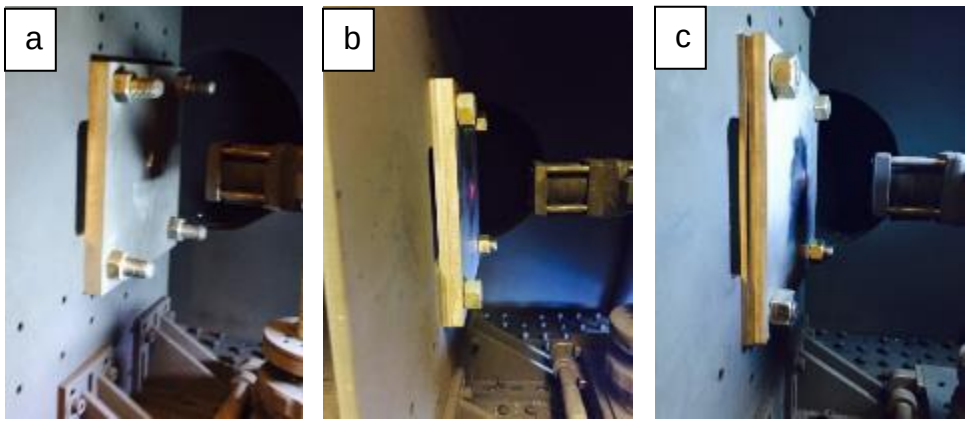

Figure 2.25: Experimental targets (a) one 0.5" thick plate, (b) two 0.25" thick stacked plates, (c) four 0.125" thick stacked plates

2.3.2 EBAM TITANIUM ALLOY

The second material system of interest included AM targets. As shown by Figure 2.26, six preforms were attached to a substrate of Titanium 6, Grade 4MS 4911, which is used as a flat surface to deposit the AM material, an extra low interstitial (ELI) grade of Titanium 6, AMS-

4956. The six preforms were heat treated and produced using varying deposition parameters, producing three coupons with two deposits each:

- 'A' (high speed, raster on); layer height 0.125 in –0.135 in
- 'B' (high speed, raster off); layer height 0.125 in –0.135 in
- 'C' (low speed, raster on); layer height 0.140 in –0.145 in

It is noted that the rate of deposition may affect the surface smoothness, i.e. a slow deposition rate will allow the material to cool prior to laying down more material on top. Preforms were built with three beads of material being deposited per layer. Each bead overlaps slightly with the bead next to it. The centerlines of the beads are spaced 0.36 inches apart and are approximately 0.49-0.50 inches wide, creating an overlap of approximately 0.14 inches. The material may have voids that are 0.020" in diameter. The material was later machined to have similar dimensions of forged plates and is shown in Figure 2.27.

Figure 2.26: As shipped EBAM material

Figure 2.27: Machined AM preforms

However, although these materials are very close in chemical composition there are some differences. Mostly, there is a significant difference in density, especially in sample ‘C’. The density calculation is shown in Table 2.3.

Table 2.3: Densities of target materials

	Forged Ti	**AM 'A'**	**AM 'B'**	**AM 'C'**
Density (g/cc)	4.368	4.363	4.318	4.178
Percentage Difference (%)	--	0.124	1.16	4.36

2.4 EXPERIMENTAL SETUP FOR HYPERVELOCITY IMPACT EXPERIMENTS

2.4.1 TARGET PLATES CONFIGURATIONS

The thickness of the target plates is 12.7 mm so that during experiments projectiles cannot penetrate the plates completely. The projectile produces a bulge on the back surface of the target plate instead; this method has previously been successful with studied plastic deformation of other metallic materials [7-9]. The researchers used a dimension 152.4 × 152.4 x 12.7 mm (6 in× 6 in ×0.5 in). The exact target plate configuration is shown in Dr. Shawoon Roy’s Ph.D. dissertation [45].

Since there was a limited amount of AM material procured, a new, smaller sized target plate arrangement was set up to study plastic deformation of the AM titanium plates. In order to confirm our new target plate arrangement would not change the parameters of the experiment, a modeling approach was used to confirm that from changing from a 152.4 × 152.4 x 12.7 mm (6 × 6 ×0.5 in) to a 76.2 x 76.2 x 12.7 mm (3 x 3 x 0.5 in) plate would, in fact, not change the parameters of the experiment. The results of the modeling and experimental data of two test samples of A36 steel, revealed that the change of the target size did not change the parameters of the experiment.

The PDV array was focused on the back surface of the targets during experiments. In order to collect good velocimetry data, preparing the back surface of the target was critical. Using a specialized ball roller technique, a small portion of the back surface was prepared. This ball roller ensured that there was not too much reflectivity read on the PDV instrumentation. Too much reflectivity would result in spectral artifacts in the PDV data.

2.4.2 TARGET HOLDER CONFIGURATIONS

Previous experiments used a target holder configuration that was well characterized by Dr. Deepak Somasundaram in his Ph.D. dissertation [44]. These schematics and results can be found in [44-45]. In order to adapt to the new target plate configuration, a new target holder that would be mounted into the previous target chamber arrangement was designed. It included using two 152.4 × 152.4 x 12.7 mm (6 x 6 x 0.5 in) plates with holes in both plates large enough for the PDV array and projectile impact. There was an inlay in both of the targets that would house the target plates. Then it was bolted in with four ¼-20 x 5/8 in bolts. This then would be bolted into the previous target chamber arrangement. The new target plate configuration is shown in Figure 2.28.

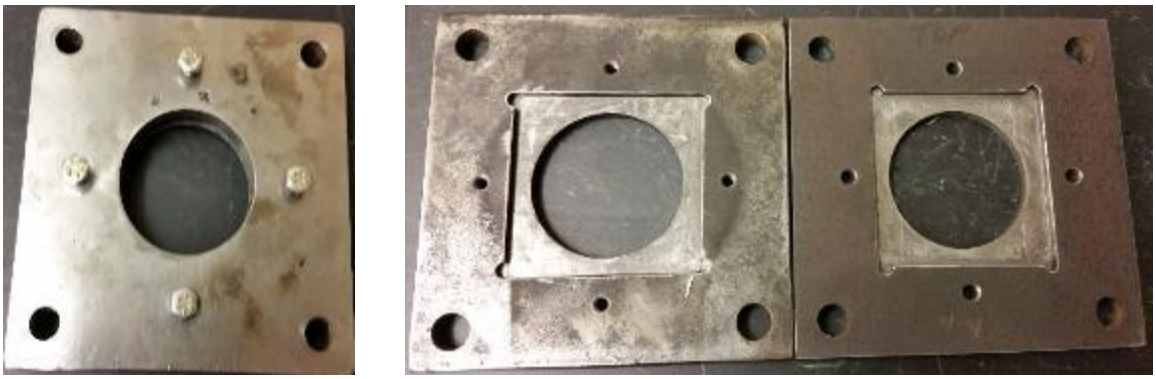

Figure 2.28: New target holder configuration

2.5 OPTICAL MICROSCOPY

In order to understand the new materials studied during experiments, a technique for optical microscopy was applied. This optical technique was perfected by Dr. Muna Slewa in her Ph.D. Dissertation [46].

The samples were polished in a BUEHLER Beta Grinder Polisher, as displayed in Figure 2.29. The process requires sanding, grinding, and polishing. The first step in the polishing process is grinding; using 270, 320, 400, 600 and 800 grit sand paper. The final polishing practice requires a 3 micrometer and a .05 micrometer polishing solution to complete the procedure. This method is very time consuming and labor intensive, particularly the impact samples, due to the uneven impact area of interest. Each sample can take 16+ hours to finalize.

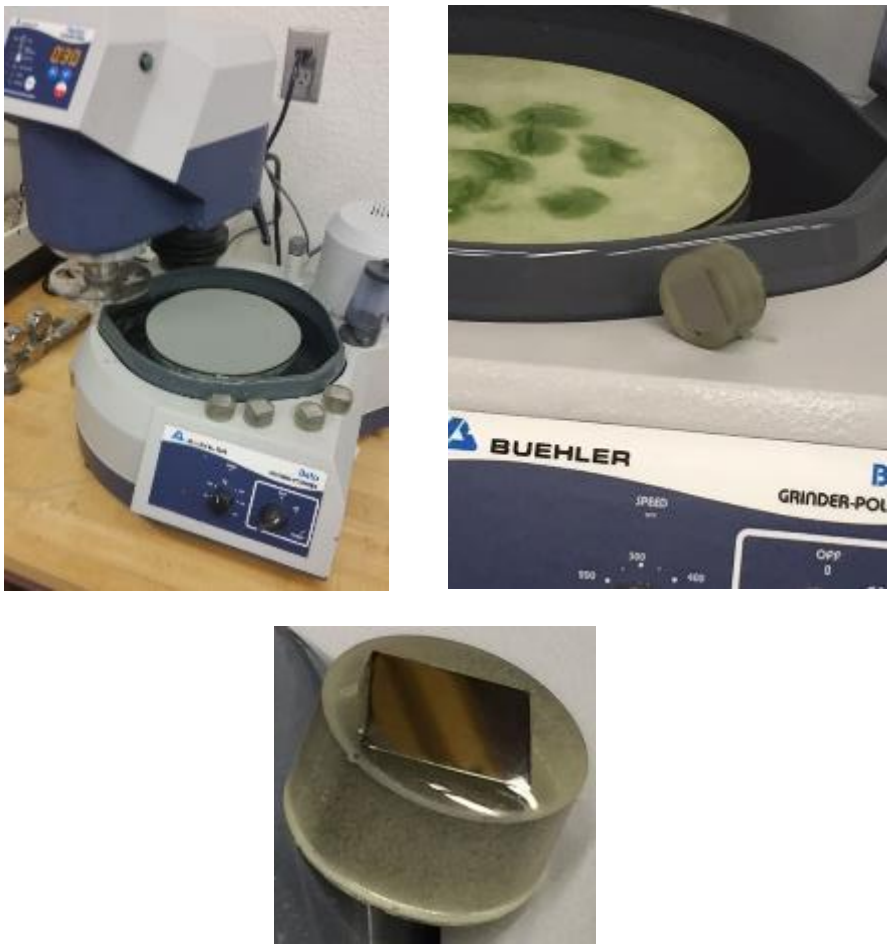

Figure 2.29: Polishing Preparation

3. EXPERIMENTAL RESULTS

Assessment of shock effects on the impacted Titanium plates were performed through two approaches:

1. Measurement of the physical damage to the plate as well as the probe points for velocity on the back surfaces of the plate.
2. Free surface velocity was measured using Photon Doppler Velocimetry (PDV) system.

3.1 PHYSICAL OBSERVATIONS

Physical damage was measured by three parameters; crater diameter, penetration depth, and back surface bulge. Each measurement was taken using slide calipers. An average of three measurements were considered the final value. The distance between the unaffected flat surface of the plate and the peak point was considered to be the height bulge. All measurements were recorded in millimeters.

The shape of the plastically deformed regions were quantified by measuring the crater diameter, penetration depth bulge, and back surface (Table 3.1-3.4). The test number indicated in the tables represent the chronological order the tests were completed in. A portion of the table has the symbol N/A in the field due to complete penetration of the plate or some type of obstacle that prevented a good measurement from being taken. An example of this obstacle would be plastically deformed shards that are inside the crater that prevent proper measurements.

The tables show that these physical measurements generally followed an increasing trend as the impact velocity increased for all target types. The only exception was the crater diameter for the four plates of 3.2 mm thick, which did not follow any specific trend among the various

velocities. This was perhaps due to the first plate undergoing complete penetration and interaction between the individual plates.

Table 3.1: Deformation results single-layer forged targets

Test #	Impact Velocity (km/s)	Crater Diameter (mm)	Penetration Depth (mm)	Back Surface Bulge (mm)
1	4.8	17 ± 1	5.8 ± 0.1	N/A
2	5.2	18 ± 1	6.3 ± 0.1	0.3 ± 0.1
4	5.6	20 ± 1	N/A	1.0 ± 0.1
13	6.1	21 ± 1	6.4 ± 0.1	1.2 ± 0.1
19	6.6	23 ± 1	7.8 ± 0.1	4.2 ± 0.1
24	6.6	22 ± 1	7.7 ± 0.2	N/A

Table 3.2: Deformation results two-layer forged targets

Test #	Impact Velocity (km/s)	Crater Diameter (mm)	Penetration Depth (mm)	Back Surface Bulge (mm)
6,a	5.5	20±1	6.0 ± 0.2	1.8 ± 0.1
6,b	5.5	23±1	1.5 ± 0.2	0.9 ± 0.1
7,a	5.6	20±1	6.3 ± 0.3	2.1 ± 0.1
7,b	5.6	21±1	2.0 ± 0.1	0.7 ± 0.1
20,a	6.2	22 ± 1	7.5 ± 0.2	2.6 ± 0.1
20,b	6.2	23 ± 1	2.6 ± 0.1	1.5 ± 0.1
17,a	6.7	22 ± 1	N/A	N/A
17,b	6.7	28 ± 1	3.1 ± 0.1	2.6 ± 0.4

Table 3.3: Deformation results four-layer plate forged targets

Test #	Impact Velocity (km/s)	Crater Diameter (mm)	Penetration Depth (mm)	Back Surface Bulge (mm)
8,a	5.4	22 ± 1	N/A	N/A
8,b	5.4	26 ± 1	4.1 ± 0.2	3.0 ± 0.1
8,c	5.4	27 ± 1	3.3 ± 0.2	2.4 ± 0.1
8,d	5.4	27 ± 1	2.2 ± 0.2	1.7 ± 0.2
9,a	5.6	25 ± 1	N/A	N/A
9,b	5.6	19 ± 1	4.3 ± 0.2	3.2 ± 0.1
9,c	5.6	17 ± 1	2.7 ± 0.2	3.0 ± 0.1
9,d	5.6	27 ± 1	2.4 ± 0.1	2.2 ± 0.1
21,a	6.2	22 ± 1	N/A	N/A
21,b	6.2	23 ± 1	5.7 ± 0.1	4.3 ± 0.1
21,c	6.2	23 ± 1	4.4 ± 0.1	3.2 ± 0.1
21,d	6.2	25 ± 1	3.7 ± 0.4	3.1 ± 0.1
18,a	6.8	22 ± 1	N/A	N/A
18,b	6.8	22 ± 1	6.8 ± 0.3	5.6 ± 0.2
18,c	6.8	25 ± 1	5.5 ± 0.1	4.4 ± 0.1
18,d	6.8	23 ± 1	4.9 ± 0.1	3.4 ± 0.2

Table 3.4: Deformation results of AM targets

Test #	Impact Velocity (km/s)	Target Material	Crater Diameter (mm)	Penetration Depth (mm)	Back Surface Bulge (mm)
5	5.2	AM ‘A’	20x21± 1	6.16 ±0 .1	0.9± 0.1
10	5.6	AM 'A'	20x21 ± 1	8.6 ±0 .1	1.0 ± 0.1
14	6	AM 'A'	21x23 ± 1	8.1 ± 0.2	4.5 ± 0.1
22	5.3	AM 'B'	19x20 ± 1	5.9 ± 0.1	1.2 ± 0.1
11	5.6	AM 'B'	20x21 ± 1	5.9 ± 0.2	2.1 ± 0.2
15	6.1	AM 'B'	21x22 ± 1	8.2 ± 0.1	5.2 ± 0.1
23	5.1	AM 'C'	18x20 ± 1	6.0 ± 0.1	1.0 ± 0.2
12	5.6	AM 'C'	20 ± 1	6.3 ± 0.3	3.2 ± 0.1
16	5.9	AM 'C'	20x23 ± 1	8.0 ± 0.1	4.9 ± 0.1

Figures 3.1 through 3.4 show the cross-sections of typical forged 12.7 mm Ti and AM 'A', ‘B’, and ‘C’ targets, respectively. These figures help illustrate the differences in response of these two target types. In both cases, as impact velocity increases, internal fracturing occurs, leading to spalling at the higher impact velocities. It is noted that spalling became evident at Figure 3.1(d) with a velocity of 6.612 km/s in the case of the forged material. On the other hand, AM material exhibits spalling at lower velocities as shown in Figure 3.2(c) at 5.976 km/s, Figure 3.3(c) at 6.08 km/s, and Figure 3.4(c) at 5.907 km/s.

Additionally, the discontinuities in crystal structure due to the continuous process of melting and solidification may affect the performance of the AM materials, even after undergoing heat treatment. It is also observed that the AM plates under higher velocity impacts exhibit non-uniform crack propagation throughout the material along with brittle and fragmentation failure mechanisms that are occurring simultaneously, Figure 3.4(c). The same figure shows that the material is exhibiting shear plugging. Figure 3.5 reveals a plugging failure mode which was not as severe in other specimens at equal velocities.

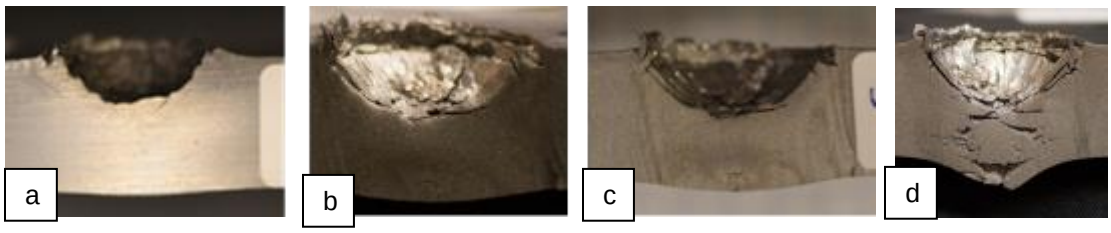

Figure 3.1: Deformation vs. impact velocity for forged 12.7mm Ti plate at velocities of (a) 4.838 km/s, (b) 5.655 km/s, (c) 6.145 km/s, and (d) 6.612 km/s

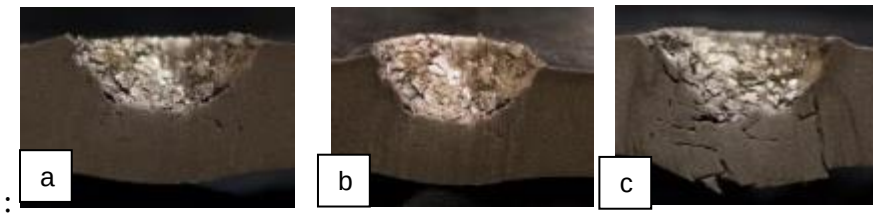

Figure 3.2: Deformation vs. impact velocity for AM 'A' 12.7 mm Ti plate at velocities of (a) 5.175 km/s, (b) 5.552 km/s, and (c) 5.976 km/s

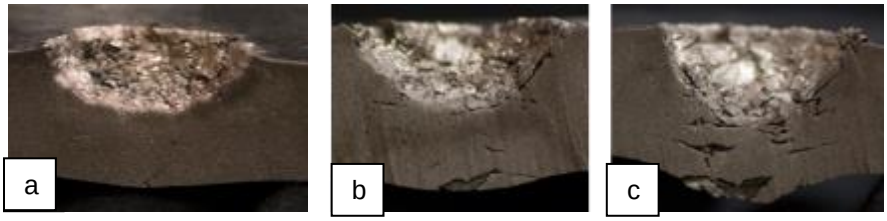

Figure 3.3: Deformation vs. impact velocity for AM ‘B’ 12.7 mm Ti plate at velocities of (a) 5.255 km/s, (b) 5.613 km/s, and (c) 6.08 km/s

Figure 3.4: Deformation vs. impact velocity for AM ‘C’ 12.7 mm Ti plate at velocities of (a) 5.14 km/s, (b) 5.634 km/s, and (c) 5.907 km/s

Figure 3.5: AM ‘A’ shows severe shear failure at 5.976 km/s

In the 2-layer case, the first layer also showed material pull back causing the first and second plate to deform differently as shown in Figure 3.6. It is noted that at the highest velocity

for the 2-layer experiment, material spall and separation on the first plate was evident. It is noted that the 4-layer forged titanium alloy experienced first-layer penetration at all tested velocities. The first-layer also experiences material pull back causing the first-layer and second-layer to deform in different directions, which creates a gap between the first- and second-layer, as shown in Figure 3.7. An interesting feature of the 4-layer is that it shows material spring back. Since the material undergoes intense compression followed by decompression where the projectile and the target material are ejected off the front surface of the target as a solid or is lost as a vapor, the cavity sides spring back. It was also found that the performance of the in-contact multi-layered plates experienced more damage, than that of a single-layer plate of equal thickness.

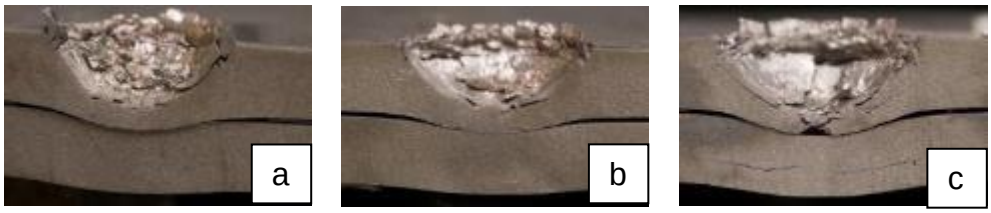

Figure 3.6: Deformation vs. impact velocity for 2-layer plates at velocities of (a) 5.6 km/s (b) 6.2 km/s (c) 6.7 km/s

Figure 3.7: Deformation vs. impact velocity for 4-layer plates at velocities of (a) 5.1 km/s, (b) 5.603 km/s, (c) 6.773 km/s

Overall, the AM material showed more signs of failure at slower velocities than that of the multi-layered plates. The additive manufactured material had macroscopic cracks at lower velocities and had spalled at much lower velocities. The forged plates had the least amount of

damage at comparable velocities. The forged material showed no apparent signs of spall or macroscopic cracks until about 6.6 km/s.

Figure 3.8 shows the regression for the single forged and AM plates of velocity versus crater diameter. The results show a linear relationship between permanent deformation and impact velocity. There was not a similar trend in the 4-layer plate configuration. It is believed to be because a portion of the impact energy is spent on the spring back of the front plate. The slopes of each of the samples are fairly similar except for the AM ‘C’ plate, which had a significantly higher slope, and the 4-layer having a negative slope. This implies that the AM ‘C’ plate had significantly more deformation at the higher velocities than that of the lower velocities. More in-depth analysis of microstructure could reveal different failure mechanisms in the lower velocities than in the higher velocities. No trend was found for the 4-layer case, this could be due to more energy being spent on the material pull back and vibrations between the plates.

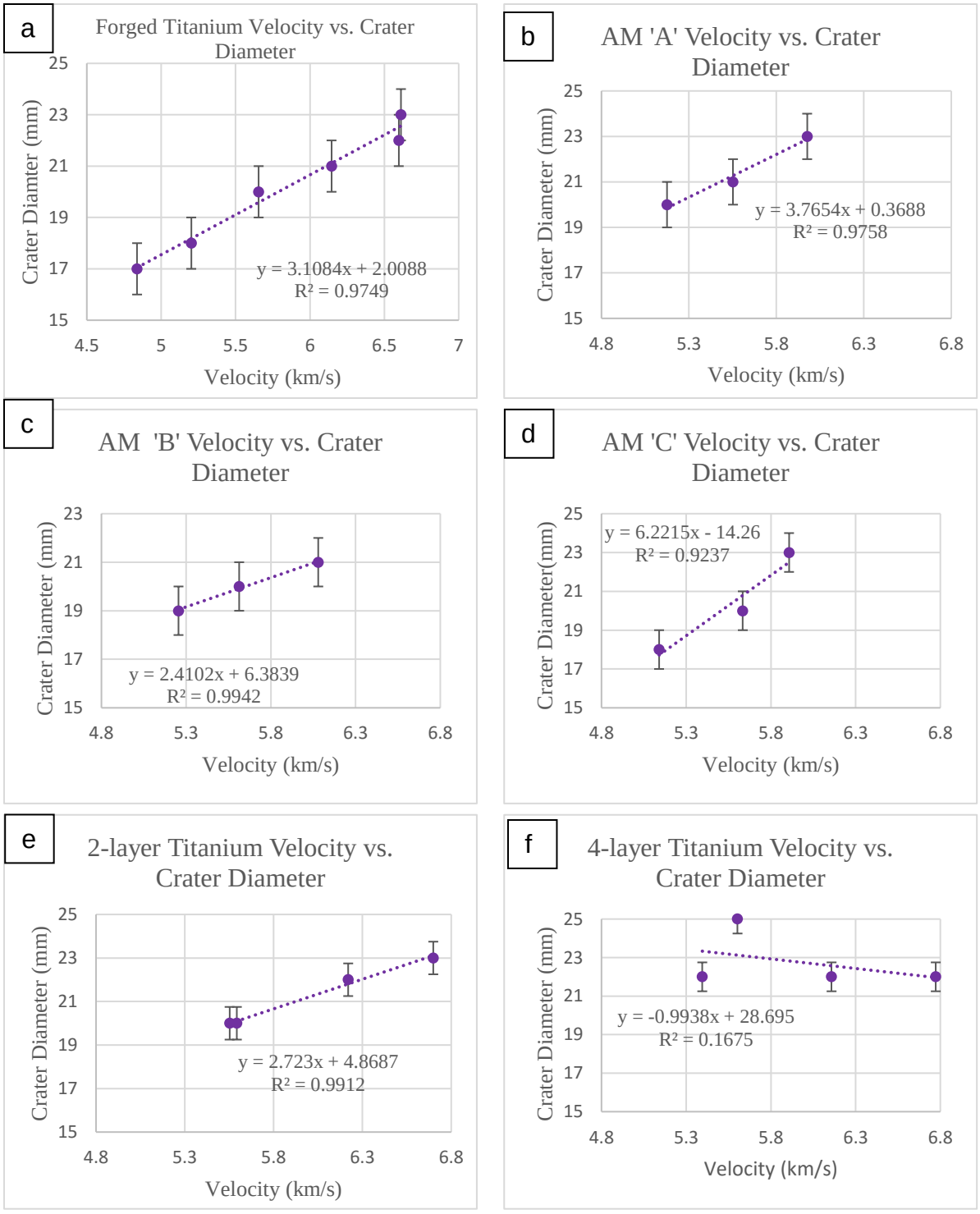

Figure 3.8: Velocity vs. crater diameter trends (a) Forged Ti, (b) AM 'A' Ti, (c) AM 'B' Ti, (d) AM 'C' Ti, (e) 2-layer (f) 4-layer

Figure 3.9 shows the trends in the impact velocity and the crater penetration depth. This data also shows a linear trend for penetration depth with increasing impact velocity. There is one anomaly that might be explained by the uneven properties of inside the impact crater. Since the inside of the crater is not perfectly cut out during impact, it sometimes becomes difficult to measure the inside of the crater. The slopes of all the AM titanium are very comparable. The forged titanium, however, has a less steep of a slope translating to less damage occurring at comparable velocities.

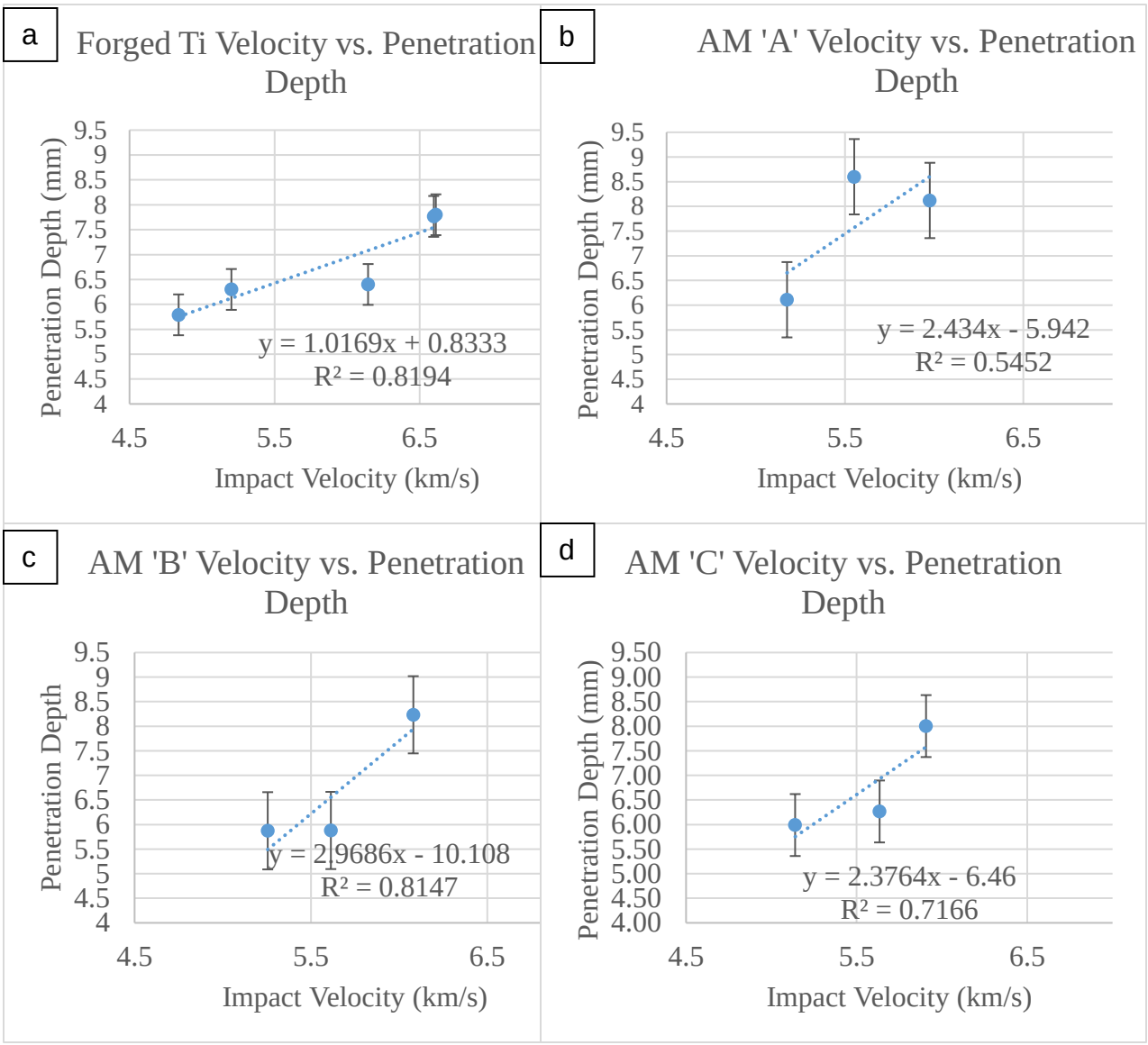

Figure 3.9: Single layer plate velocities vs. penetration depth (a) Forged Ti (b) AM 'A' Ti (c) AM 'B' Ti (d) AM 'C' Ti

Figure 3.10 shows the multi-layer plate velocities and the penetration depth measurement. This data set also shows a linear trend with increasing velocity. For the 4-layer configuration, the first plate is not shown due to complete penetration of the first plate. The variation for the 2-layer plate configuration may be due to the variation on the inside the crater.

The negative slope in the first plate of the 2-layer experiment could be due to energy being spent on material spring back and vibrations between the plates. The 4-layer case all of the plates have similar slopes, which indicated failure occurred at the same rate in all the plates.

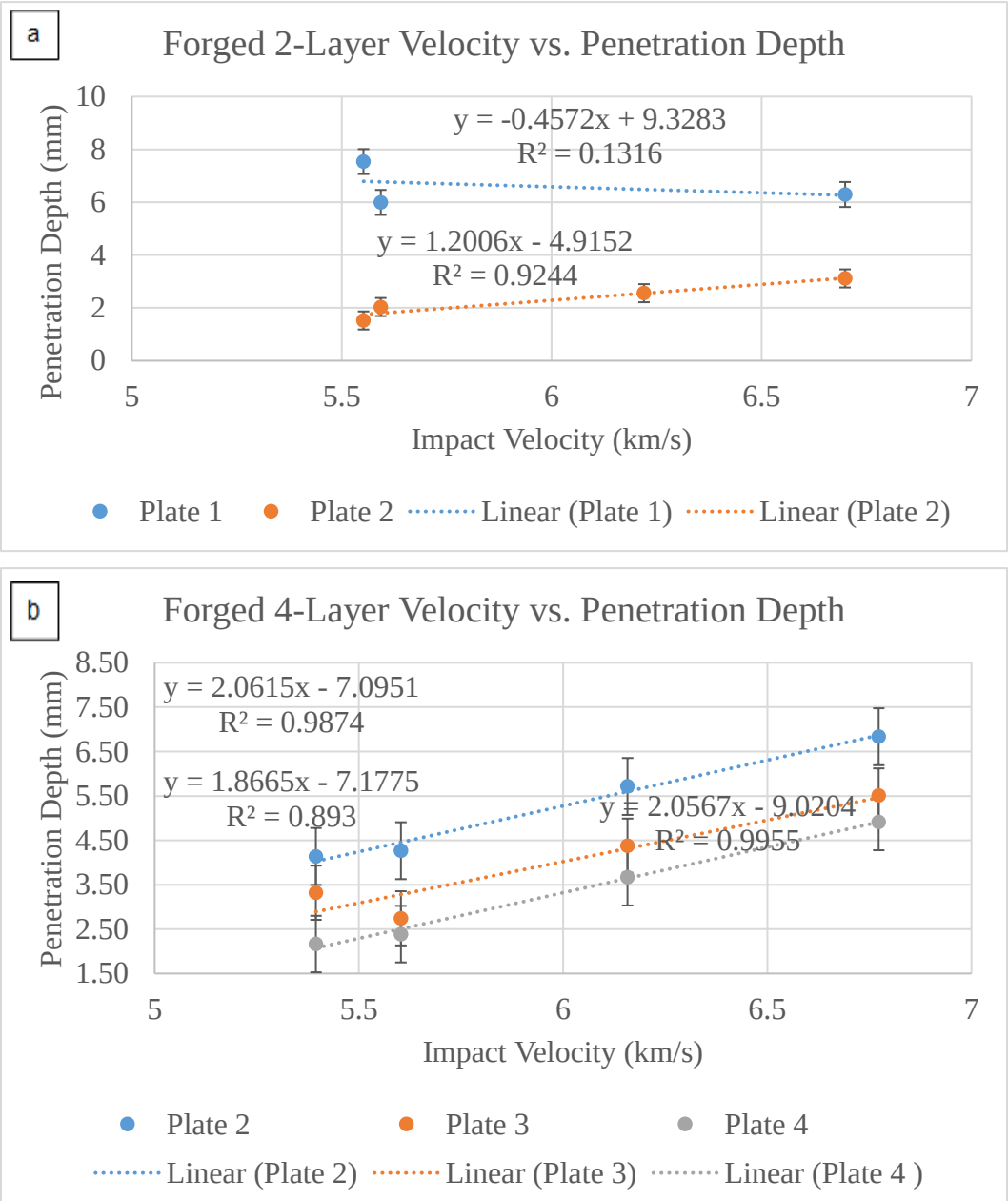

Figure 3.10: Multi-layer sample velocities vs. penetration depth (a) 2-layer (b) 4-layer

Figure 3.11 shows the trends for impact velocity and back surface bulge. Unsurprisingly, the data also shows a linear trend with an increase of impact velocity; there is an increase in the bulge on the back surface. The outliers from the forged and ‘A’ material can be due to spall separation during impact that resulted in a loss of material on the back surface. The slopes of the AM material are very similar, showing that damage occurs at close to the same rate. However, the forged material has a different, less steep, slope displaying that the damage occurs at a much slower rate than the AM titanium.

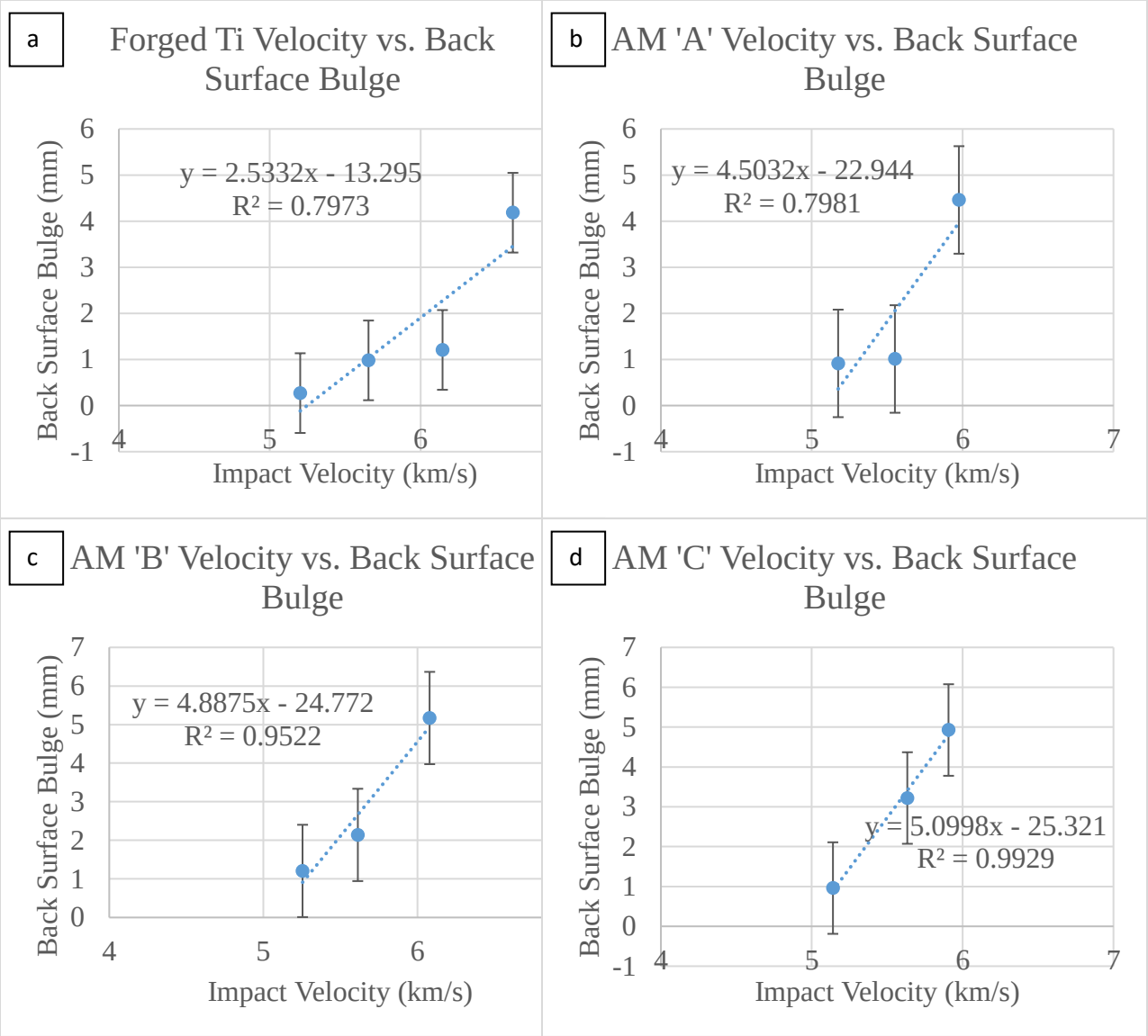

Figure 3.11: Single layer plate impact velocities vs. back surface bulge (a) Forged Ti (b) AM 'A' Ti (c) AM 'B' Ti (d) AM 'C' Ti

Figure 3.12 shows the multi-layer plate trends for impact velocities and back surface bulge. An important thing to note for this data, the middle plates experienced spall and separation and could result in variations to bulge data. Still, the data shows a linear trend and for

larger impact velocities, the larger the bulge will become. Both the plates in the 2-layer case show similar slopes indicating that the damage occurs at nearly the same rate. Also, the plates in the 4-layer experiments have nearly the same slope. The second plate in the 4-layer experiments has a steeper slope indicating that damage increased faster with increasing velocity than in the other plates.

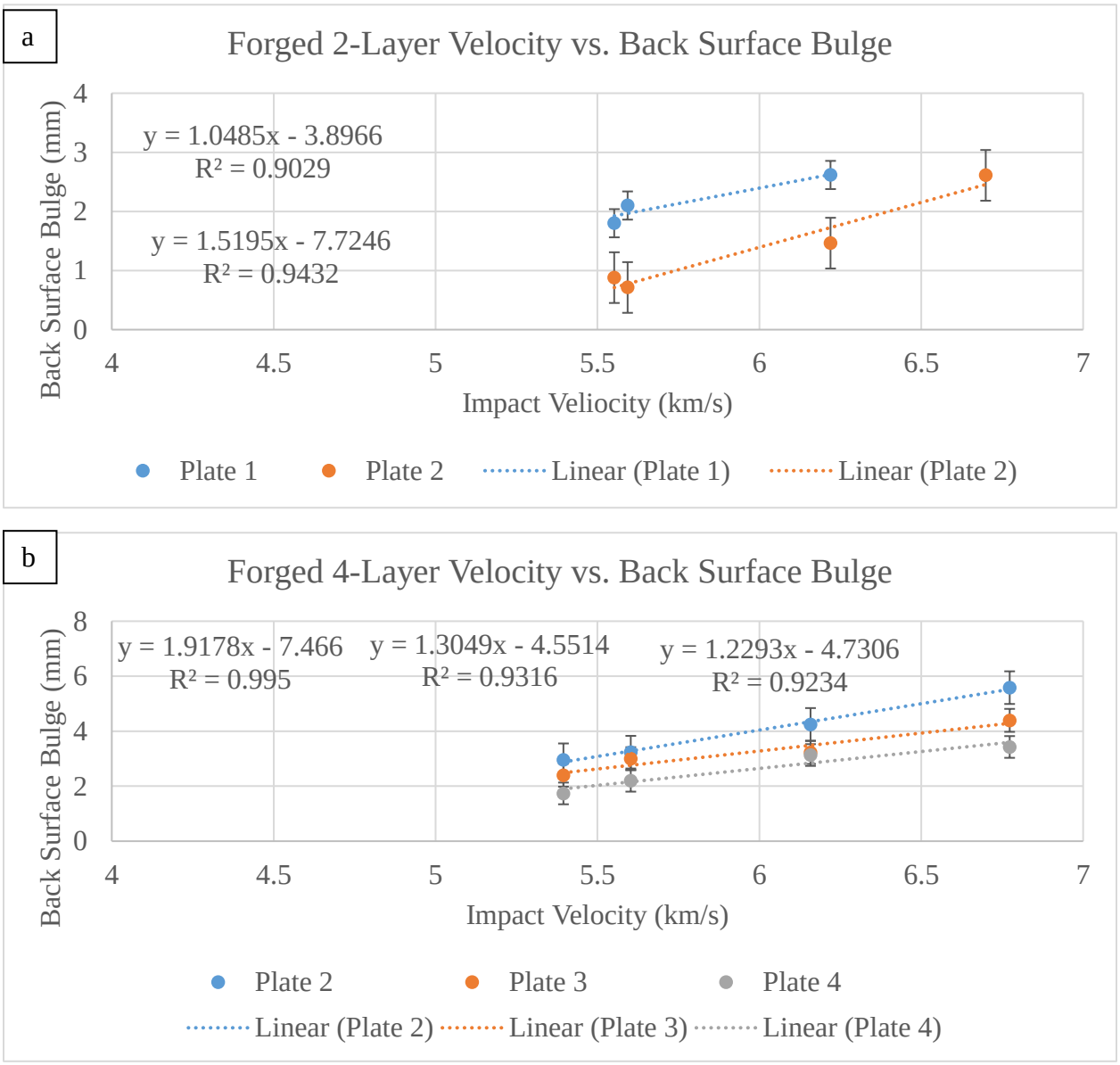

Figure 3.12: Multi-layer plate impact velocities vs. back surface bulge (a) 2-layer (b) 4-layer

3.2 MICROSCOPIC RESULTS

After approximately 20+ hours of sanding and polishing, two samples were prepared to view under a Scanning Electron Microscope (SEM). Figure 3.13, shows the AM ‘C’ samples with a scale of 200 μm. Towards the middle on the upper-hand photo of the micrograph you can view something that may be a pore. From the scale you can see that the pore is less than 200 microns in length. This is well within the .02” range of the porosity the manufacturer determined. This was the only pore-like feature on the entire sample.

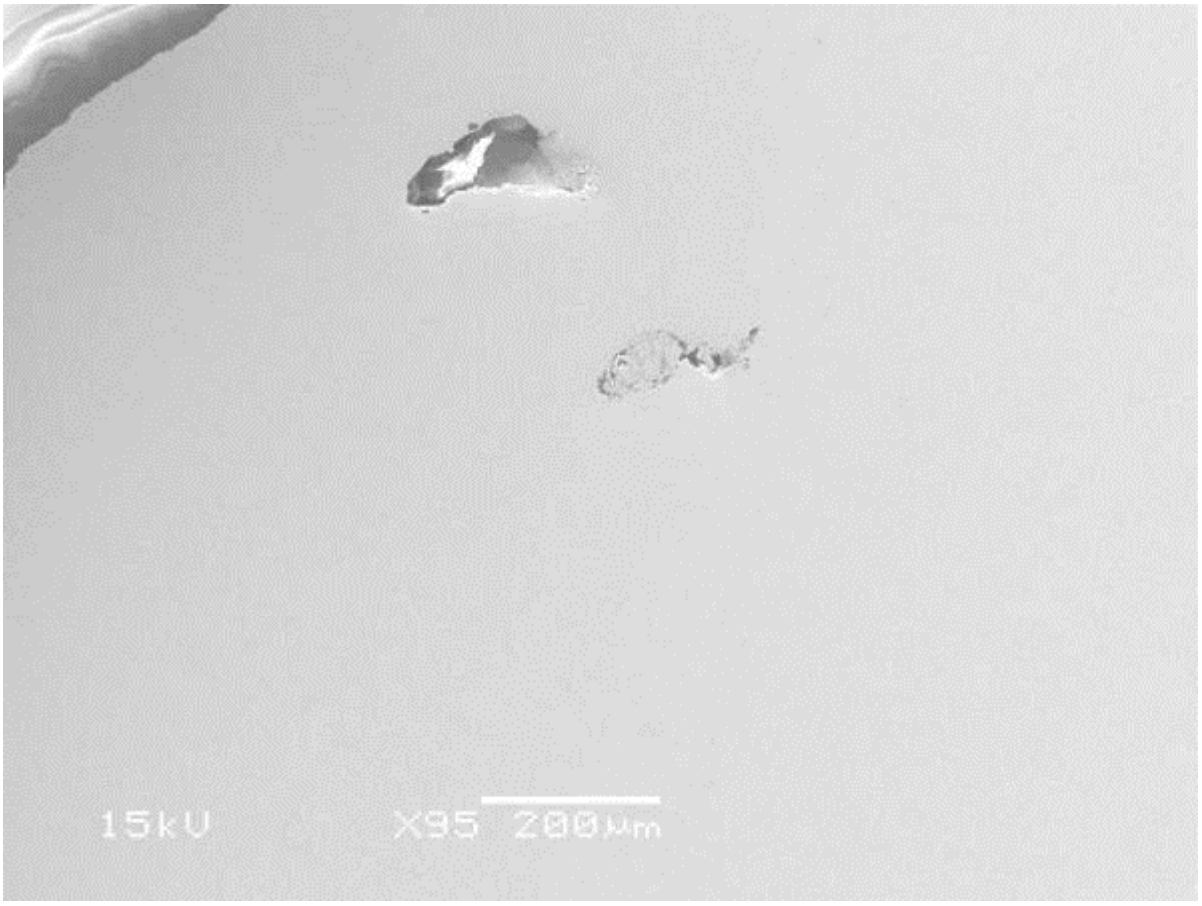

Figure 3.13: AM 'C' sample

Figure 3.14, shows the AM ‘C’ sample at a velocity of 5.6 km/s. In this micrograph there is a significant crack moving radially from the impact center. There are also two pathways that

the crack propagates. This could be due to several things; crack propagations in the crystalline structure, dislocations, and even the titanium may have more of a β-phase than an α-phase.

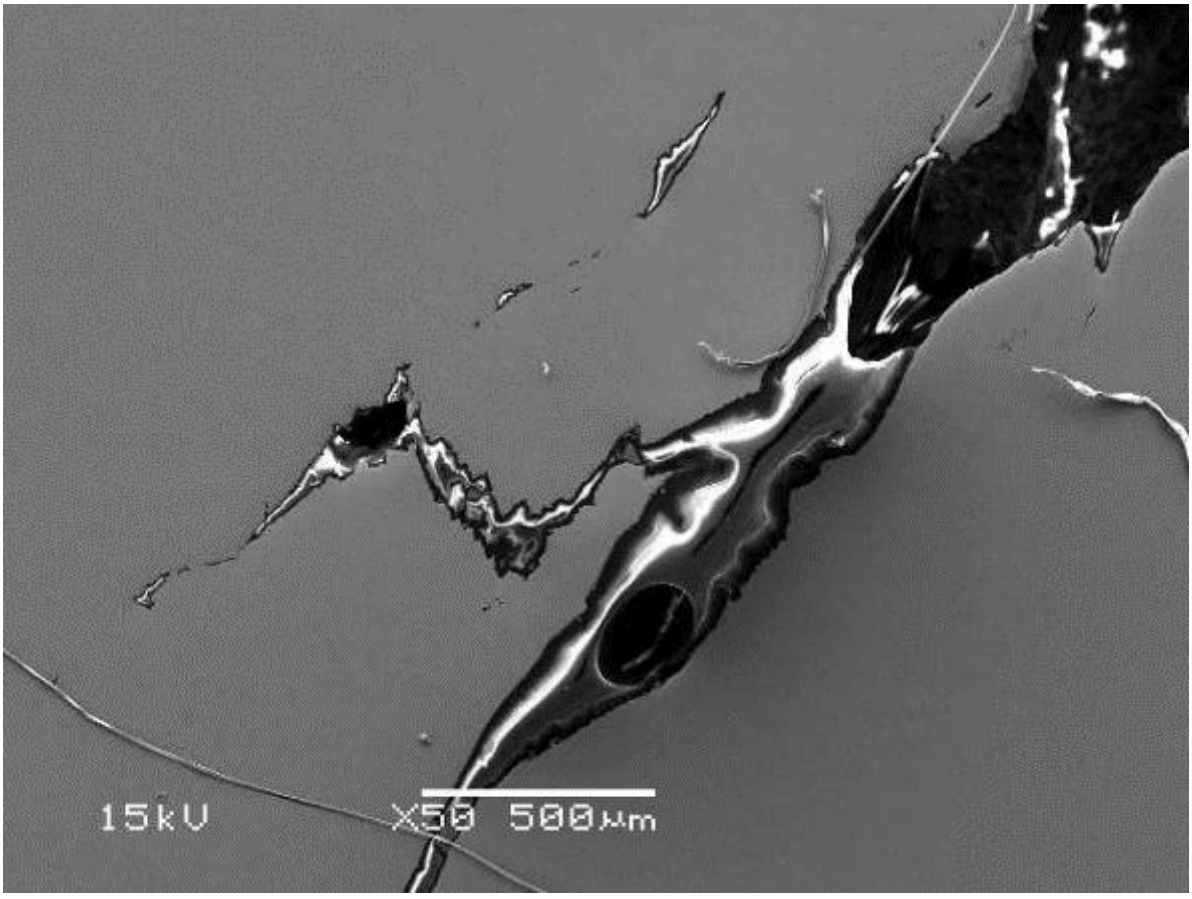

Figure 3.14: Am 'C' Sample at v~5.6 km/s

Due to the inconclusiveness of the results; further microanalysis was not completed. The fact that more pores were not found in the sample; it is believed that the crystalline structure of the α-β phase titanium alloy plays a critical role when trying to determining how the material fails.

3.3 FREE SURFACE VELOCITY

Photon Doppler Velocimetry (PDV) was utilized to collect free surface velocity data. The technique used to extract the data was well outlined in Chapter 1. Typically, PDV captures about

30-40 μs where the first 5 μs contains the most important features related to dynamic material properties.

For these experiments, the PDV probe locations were altered to provide the most valuable data. After the first twelve experiments, it was found that more useful data could be collected with the probes placed further apart. This is due to several factors that occurred during the experimental process. For example, free flight area in the two-stage gas gun setup, which causes a slight variance the location the projectile will impact the target. This is typically undesirable because the most valuable information should be at the impact center. By moving the probes farther out we were able to improve the ability to capture the impact center. Another reason for moving the probes apart was to study the dynamic material properties farther away from the impact center. This will help determine if boundary conditions were needed to be set for simulations. Graphical representations of the probe locations can be found in Appendix A. The probe locations and target descriptions are shown in Table 3.5. This table outlines the progression of changing the probes throughout the experimental series to capture the most valuable data.

Table 3.5: Target descriptions, velocity ranges, and probe locations

Test #	Target Plates	Impact Velocity (km/s)	Probe locations
1	Forged Ti, Single Plate (12.7 mm)	4.838	1 mm – 1 mm – 1 mm
2	Forged Ti, Single Plate (12.7 mm)	5.202	1 mm – 1 mm – 1 mm
3	Forged Ti, Single Plate (12.7 mm)	N/A	1 mm – 1 mm – 1 mm
4	Forged Ti, Single Plate (12.7 mm)	5.655	1 mm – 1 mm – 1 mm
5	AM Ti 'A' (12.7 mm)	5.175	1 mm – 1 mm – 1 mm
10	AM Ti 'A' (12.7 mm)	5.552	1 mm – 1 mm – 1 mm
11	Am Ti 'B' (12.7 mm)	5.613	1 mm – 1 mm – 1 mm
12	AM Ti 'C' (12.7 mm)	5.634	1 mm – 1 mm – 1 mm
6	Forged Ti, Two Plates (6.4 mm each)	5.552	1 mm – 1 mm – 1 mm
7	Forged Ti, Two Plates (6.4 mm each)	5.593	1 mm – 1 mm – 1 mm
8	Forged Ti, Four Plates (3.2 mm, each)	5.395	1 mm – 1 mm – 1 mm
9	Forged Ti, Four Plates (3.2 mm, each)	5.603	1 mm – 1 mm – 1 mm
13	Forged Ti, Single Plate (12.7 mm)	6.145	2 mm – 1 mm – 3 mm
24	Forged Ti, Single Plate (12.7 mm)	6.597	2 mm – 2 mm – 3 mm
22	AM Ti 'B' (12.7 mm)	5.255	2 mm – 2 mm – 3 mm
20	Forged Ti, Two Plates (6.4 mm each)	6.22	2 mm – 2 mm – 3 mm
21	Forged Ti, Four Plates (3.2 mm)	6.158	2 mm – 2 mm – 3 mm
19	Forged Ti, Single Plate (12.7 mm)	6.612	2 mm – 2 mm – 4 mm
14	AM Ti 'A' (12.7 mm)	5.976	2 mm – 2 mm – 4 mm
15	AM Ti 'B' (12.7 mm)	6.08	2 mm – 2 mm – 4 mm
23	AM Ti 'C' (12.7 mm)	5.14	2 mm – 2 mm – 4 mm
16	AM Ti 'C' (12.7 mm)	5.907	2 mm – 2 mm – 4 mm
17	Forged Ti, Two Plates (6.4 mm each)	6.699	2 mm – 2 mm – 4 mm
18	Forged Ti, Four Plates (3.2 mm)	6.773	2 mm – 2 mm – 4 mm

The following figures will show velocity traces of some selected tests; the velocity traces from all the shots will appear in Appendix B. Typically, the probe closest to the impact center has the most displacement and will show the maximum velocity profile. All velocity traces shown are chosen from channel one, which represents the maximum measured velocity profile. Shown in Figure 3.15 (a), (b), and (c) are the velocity profiles of the three different types of AM materials at three different velocities, 5.190 ± 0.059 km/s, 5.608 ± 0.035 km/s, and 5.990 ± 0.087 km/s. The figures show that the velocity profiles are similar for all types of AM materials at these velocities.

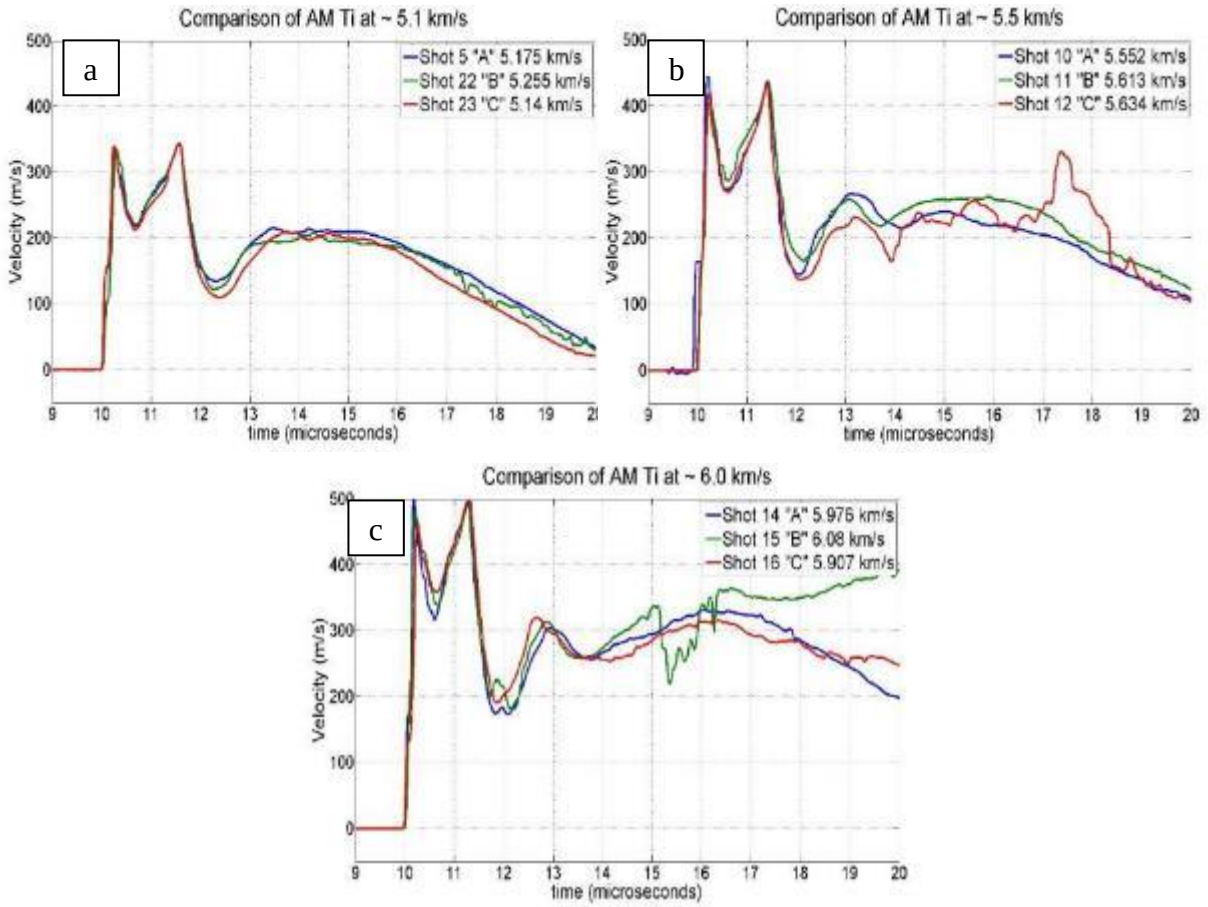

Figure 3.15: a) AM comparison at v ~5.1 km/s b) AM comparison at v~5.5 km/s c) AM comparison at v~6.0 km/s

Figure 3.16 shows a velocity profile for each of the six types of targets tested. At a velocity of 5.608 ± 0.035 km/s the 12.7 mm forged and AM target profiles are similar and both show no or little spall. The stacked targets vibrate more, especially the four stacked plates, which exhibit a significantly different profile, as shown by the red line. The two stacked plates also show a different velocity profile, shown by the green line, since there are not as many plates to vibrate, it becomes more similar to the single layer plates.

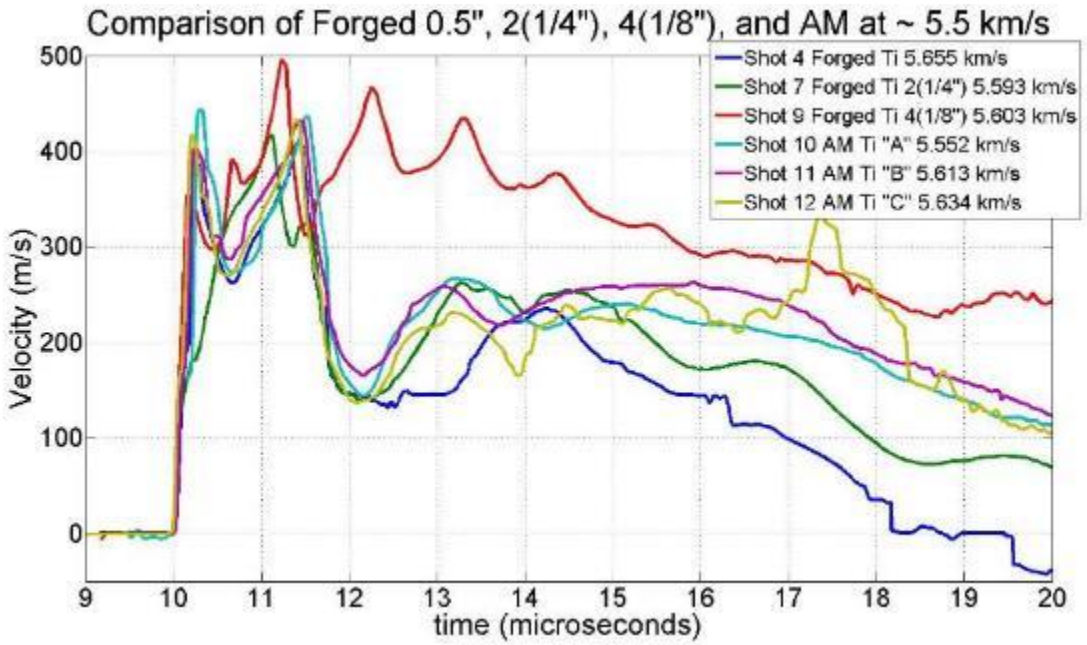

Figure 3.16: Comparison of forged, AM, and layered material at v~ 5.5 km/s

Figure 3.17 compares the 12.7 mm forged and AM targets at a velocity of 6.027 ± 0.106 km/s. All four profiles are similar, especially during the early times of the impact. As the impact progresses, the AM targets begin to spall, however the forged targets do not. No similarities between AM plates and multi-layer stacked plates could be verified. Figure 3.9 (d) shows the PDV results of the Forged Ti and the AM Ti at the same velocity of about 6.0 km/s. The shape of the curve looks similar, but the materials' elastic precursor wave and Hugoniot Elastic Limit has different values shown at this first bend in the data. The elastic wave and spall signature in both materials is pretty much the same, as well, as the elastic unloading. However, the spall ringing found at 12 μs and 13 μs is not the same for both materials. This could possibly be due to the porosity of the AM materials.

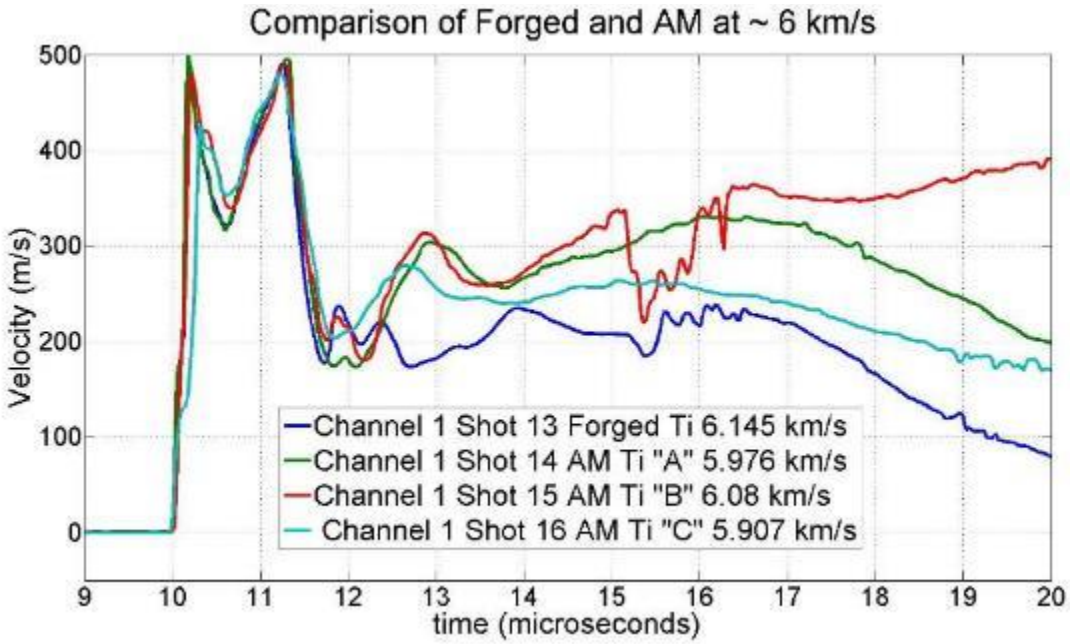

Figure 3.17: Comparison of forged and AM titanium alloy at v~ 6 km/s

4. FINITE ELEMENT ANALYSIS

During two-stage light gas gun experiments, there is a myriad of sophisticated instrumentation suites that are utilized to collect valuable data. Utilizing this instrumentation can become very costly, that is why predictive modeling has become more prevalent in this field. However, due to the complexity of the experiment, significant efforts have to be made to develop these refined computational models. One of the key objectives of this work is to create an advanced computational model to simulate projectile impact and the plastic deformation on the back surface of the target in different titanium targets, with a focus on the AM samples and layered samples. Simulating dynamic material properties in additive manufactured metals has not been done before. Developing an approach to create a predictive simulation for these unique materials will be a major contribution to the field. All computational results were formulated in LS-DYNA®.

4.1 SOFTWARE AND HARDWARE

All of the simulation analysis was accomplished on a 64 GB, 48-core CentOS 4.5 server located at UNLV, which is proficient at parallel processing. This is critical for advanced simulations due to the lengthy computational time needed. Parallel processing allows the servers to simultaneously use all of the computing power available, cutting down the computational time. A commercially available dynamic FEA package, LS-DYNA® version 8.0, was used to computationally analyze the experiments. Simulation models were created with LS-DYNA® pre-processor version 977 [41]. All simulation models were created using the metric standard unit system; with force in Newtons, mass in kilograms, length in meters, and time in seconds.

4.2 SMOOTHED PARTICLE HYDRODYNAMICS (SPH)

The solver used was a smooth particle hydrodynamic code (SPH). SPH is particularly advantageous because the movement of the particles mimic the flow of liquids or gases [34-35]. The SPH particles are capable of moving in space, unlike elements, and transport the computational information. During hypervelocity impact, normally meshed models are sometimes unable to perform properly due to the severe deformation. Since there is a substantial number of considerations that are needed to simulate hypervelocity impact; being able to transport information easily is critical. The reason SPH is able to calculate these unique properties is because each particle is an interpolation point representing displacement, acceleration, density, strain-rate, etcetera. The solution of the entire system is then analyzed on all of the particles with a regular interpolation function, considered the, "smoothing length". The way SPH is able to define the 'region of interest' is through the space and time dependent variables. This creates the rudimentary equations to calculate the partial differential equations (PDEs) illustrating the conservation law of continuum fluid dynamics [36].

4.3 MODEL DESIGN

As previously mentioned, all the models were developed using a Lagrangian particle method, SPH in LS-DYNA®. Initial development of the simulations was created using LS-PREPOST 4.2 Beta. All models were designed as 2-D axis-symmetric to reduce computational time. This had been previously used with relatively good success [7-9]. The axis-symmetric design was able to simulate the impact because the projectile impacted near the center of the plate. Since the number of particles was reduced, the computational run time was also reduced.

SPH particles were used in both the target and the projectile. In the simulations, a range of dimensions were used to model the titanium samples shown in Table 4.1. Great care was taken

such that the mass of the SPH particles in the target approximately matched the mass of the particles in the projectile. To ensure a convergence in data output in the simulation, an expansive particle spacing study was completed. The results of this study showed a particle spacing of 0.1 mm was the best spacing to extract the most data and minimize the run time. Details of the particle spacing can be found in Appendix C. The nature of HVI reveals that no boundary conditions are necessary for the axis-symmetric model, therefore, none were applied. A typical model is shown in Figure 4.1.

Table 4.1: Simulation Dimensions

Titanium Sample	**Dimensions (mm x mm x mm)**
Forged Titanium	152.4 x 152.4 x 12.7
Forged Titanium (6.35 mm) stacked	2 x (152.4 x 152.4 x 6.35)
Forged Titanium (3.175 mm) stacked	4 x (152.4 x 152.4 x 3.175)
AM Titanium 'C'	76.2 x 76.2 x 12.7

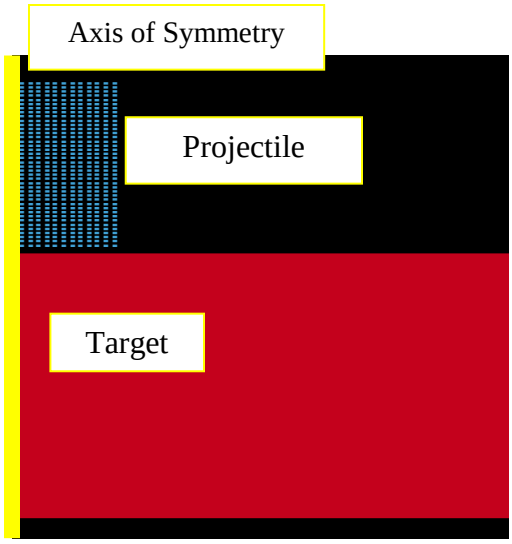

Figure 4.1: Typical 2-D axis-symmetric model

4.4 JOHNSON-COOK MATERIAL MODEL

An important aspect of designing the model for HVI is the material model. Since the aspect of this research is modeling plastic deformation of metal, the Johnson-Cook material model was used. The Johnson-Cook material model was developed specifically for modelling high-strain rate and high temperatures [47]. The Johnson-Cook material model has been widely used to model HVI over the years and is considered the most effective way to simulate these dynamic events [48-51].

The basis of the Johnson-Cook material model is the constitutive equation. The equation calculates the stress as a function of large strains, high strain-rates, and high temperatures [41]. The flow stress is calculated by the following:

$$\sigma_y = (A + B\bar{\varepsilon}^{p\,n})(1 + c \ln \dot{\varepsilon}^*)(1 - T^{*\,m}) \qquad (1)$$

Where A, B, c, n, and m are input constants, $\bar{\varepsilon}^p$ is the effective plastic strain, $\dot{\varepsilon}^*$ is the strain rate normalized for plastic or total strain, and T^* is the homologous temperature. The homologous temperature is defined as:

$$T^* = \frac{T - T_{room}}{T_{melt} - T_{room}} \quad (2)$$

LS-DYNA® uses a simplified version of the Johnson-Cook; no damage parameter was chosen. This lack in damage parameters was accounted for by including a spall parameter (P_{min}) in the LS-DYNA® Johnson-Cook model. This calculation will be discussed fully in section 4.5. The specific parameters used for the Lexan™ projectile [52] and Ti-6Al-4V target [53] are listed in Table 4.2.

Table 4.2: Johnson-Cook Material Properties

Material	A (MPa)	B (MPa)	c	m	n	Tmelt (°K)	ν†
Lexan™	75.8	68.9	0	1.85	1.004	533	0.34
Ti-6Al-4V	1098	1092	0.014	1.1	0.93	1878	0.342

†ν is Poisson's Ratio

4.5 MIE-GRÜNEISEN EQUATION OF STATE (EOS)

According to Çengel and Boles, "Any equation that relates the pressure, temperature, and specific volume of a substance is called an equation of state" [54]. Naturally, all computational models require an equation of state to relate these properties; specifically in this case it needs to account for the adiabatic changes experienced at high strain rates. The EOS and the material model combined can help simulate the shock wave propogation through a material.

The particular EOS that was chosen for these simulations was the Mie-Grüneisen. The Mie-Grüneisen is unique because it is well known to be used for shock-compressed solids [55]. This particular EOS is used to determine the pressure in a solid under extreme dynamic loading

conditions, using the polynomial Hugoninot curve. LS-DYNA®'s expression of the Mie-Grüneisen [41] is,

$$P = \frac{\rho_0 c_0^2 \mu\left(1+\left(1-\frac{\gamma_0}{2}\right)\mu-\frac{a}{2}\mu^2\right)}{\left(1-(S_1-1)\mu-S_2\frac{\mu^2}{\mu+1}-S_3\frac{\mu^3}{(\mu+1)^2}\right)^2} + (\gamma_0 + a\mu)E, \qquad (3)$$

where P is the pressure; ρ is the instantaneous density, C_0 is the Hugonniot intercept, a is the correction factor for volume, γ_o is the Grüneisen coefficient, S_1, S_2, and S_3 are the coefficients of slope of the shock velocity-particle curve: E is the internal energy; and finally μ is defined as $(\rho/\rho_o - 1)$ where ρ_o is the reference density. For materials under intense compression a temperature corrected equation has to be used. This form is given as [41],

$$P = \frac{\rho_0 C_0^2\, \mu\left(1+\left(1\frac{\gamma_0}{2}\right)\mu\right)}{(1-(S_1-1)\mu)^2} + \gamma_0 E \qquad (4)$$

This can be adapted if there is a negligible change in internal energy and density and is as follows;

$$P = \frac{\rho_0 C_0^2 (2-\frac{\gamma_0}{2})}{(1-S_1)^2}. \qquad (5)$$

The following Grüneisen EOS parameters, shown in Table 4.3, for Lexan and Ti-6Al-4V were used in the simulations.

Table 4.3: Mie- Grüneisen parameters

Material	ρ_0 (kg/m^3)	C_0 (m/s)	S1	γ_0
Lexan™	1190	1993	1.42	0.61
Ti-6Al-4V	4428	5130	1.028	1.23

4.6 HUGONIOT ELASTIC LIMIT (HEL) AND SPALL STRENGTH ESTIMATION CALCULATION

During HVI, materials undergo plastic deformation. There is a point in this process when the material changes from a purely elastic state to an elastic-plastic state. It is this transition point that is called the Hugoniot Elastic Limit (HEL). Anything above the HEL, the material begins to drop in shear strength and the material starts to behave more fluid like. Spall strength is defined as the amplitude of the tensile waves induced by shock that causes the material to fail [5]. This value is defined in the LS-DYNA® computational simulations in the Johnson-Cook material model as Pmin, as previously mentioned. Both the HEL and the spall strength can be calculated through analysis of free-surface velocimetry data.

The experimental Hugoniot Elastic Limit, $\sigma_{HEL,}$ and spall strength, σ_{spall} of the titanium was calculated from the extracted velocity curves by determining that the impact is one-dimensional and localized and has the resulting relations [56],

$$\sigma_{HEL} = \frac{1}{2}\Delta U_H \rho_0 C_l \quad (6)$$

$$\sigma_{spall} = \frac{1}{2}\Delta U_{fs} \rho_0 C_b \quad (7)$$

where ΔU_H is the free-surface velocity in the elastic precursor wave, ΔU_{fs} is the pullback velocity of the free-surface depicted in Figure 4.2; and C_l and C_b is the longitudinal and bulk speed of sound.

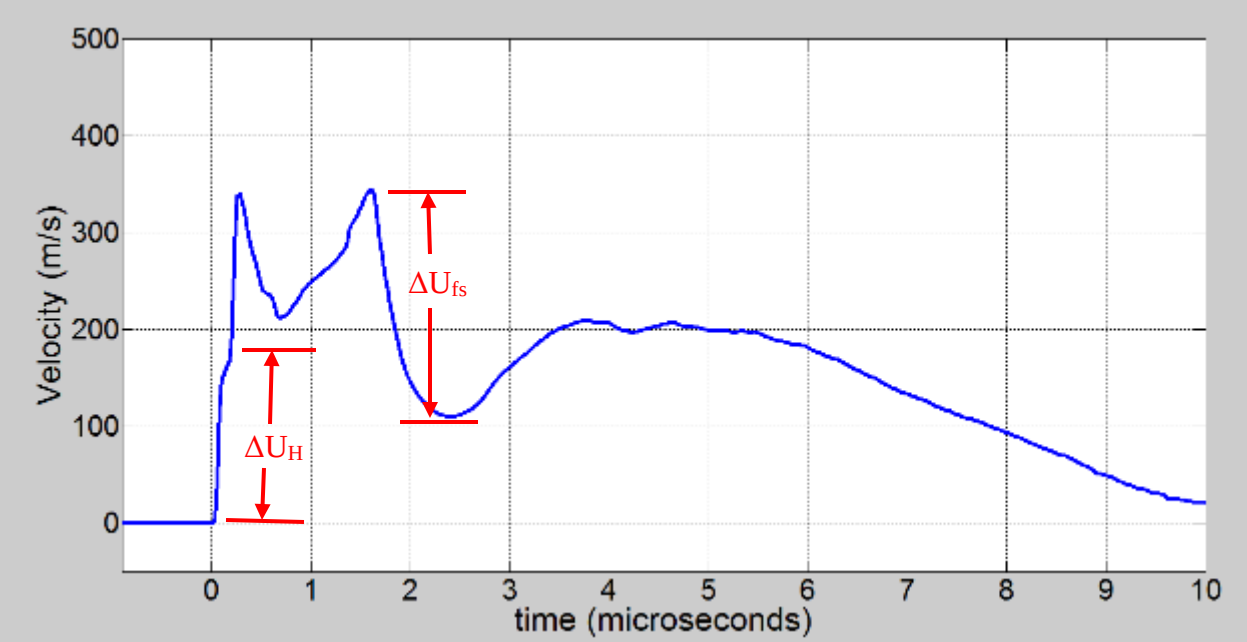

Figure 4.2: Experimental HEL and spall strength calculation from velocimetry curve

The speeds, previously mentioned, are dependent on the mechanical properties of the material. Specifically, Young's Modulus, E, and the bulk modulus, G, are the properties needed to calculate the longitudinal and bulk speed of the sound in the titanium alloy. The following equations represent the speeds;

$$C_l = \sqrt{\frac{E}{\rho}} \qquad (8)$$

$$C_b = \sqrt{\frac{G}{\rho}} \qquad (9)$$

Utilizing these equations, the experimental values for spall strength and the Hugniot Elastic Limit were estimated. The samples that were estimated included forged titanium, AM 'C', and 2-layer. The results of these findings have been recorded in Table 4.4, Table 4.5, and Table 4.6.

Table 4.4: Forged titanium HEL and spall strength estimation

Impact Velocity (km/s)	Average σHEL (GPa)	Average σspall (GPa)
4.8	1.48	1.13
5.2	1.77	1.56
5.5	1.65	1.77
5.7	1.93	1.85
6.1	1.86	2.07
6.6	2.12	2.04
Total Average	1.80	1.74

Table 4.5: AM 'C' HEL and spall strength estimation

Impact Velocity (km/s)	average σHEL (GPa)	average σspall (GPa)
5.1	1.70	1.33
5.6	1.76	2.02
5.9	1.31	1.92
Total Average	1.59	1.76

Table 4.6: Forged 2-layer HEL and spall strength estimation

Impact Velocity (km/s)	average σHEL (GPa)	average σspall (GPa)
5.5	1.77	1.16
5.6	1.90	1.17
6.2	1.63	1.44
6.7	1.80	2.11
Total Average	1.78	1.47

Although the average measured value for spall strength in the forged material was found to be 1.74 GPa, the value used in the simulations for P_{min} was taken from the manufacturer, Altemp Alloys Inc., to be 0.98 GPa (Table 2.2). The value of P_{min} was changed to represent the experimental values for spall strength. The value of spall strength given by the literature

performed more closely to the velocity curve of the experimental data, shown in Figure 4.3. Estimated spall strength in the experimental data is not found under uniaxial strain. The simulations' spall strength is calculated using uniaxial strain conditions and therefore using the estimated spall strength is not a good match. The value from the literature was also used for the 2-layer simulation experiments. Finally the value used for the AM 'C' material is 0.93 GPa which is 5% lower than the forged counterpart as explained by the manufacturer.

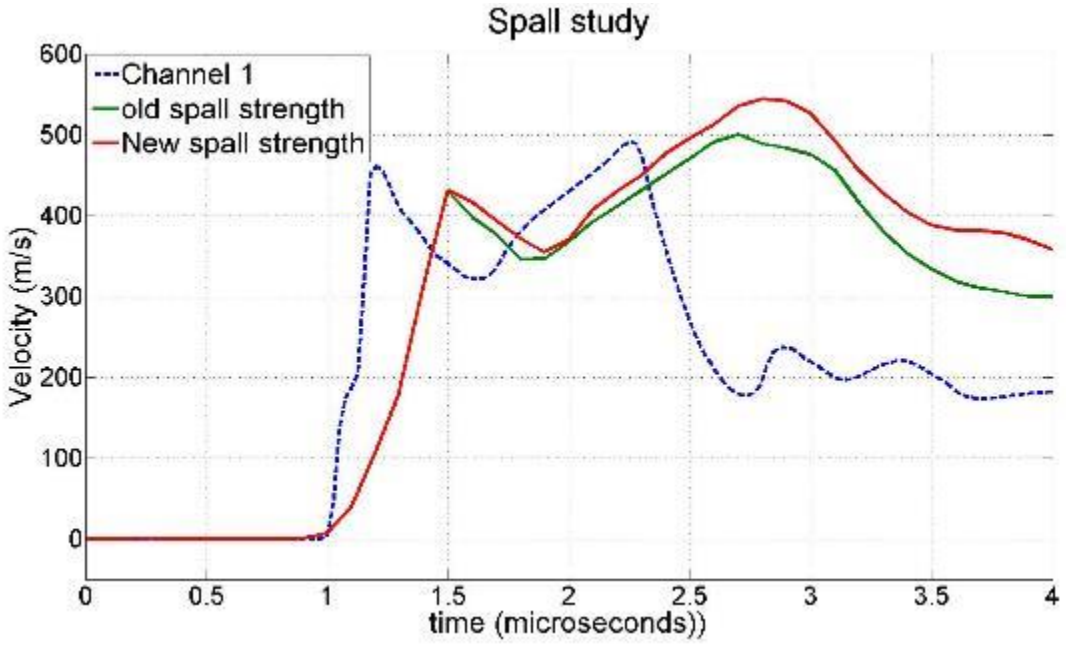

Figure 4.3: Spall study on forged titanium alloy

4.7 SIMULATION DAMAGE RESULTS

In all of the LS-DYNA® simulations it is not unusual for the projectile to completely dissolve into the target plate (Figure 4.4). In the simulation, the target plates develop a crater, and a bulge on the back surface just like the real experiments. The simulation also develops spall cracks (Figure 4.5).

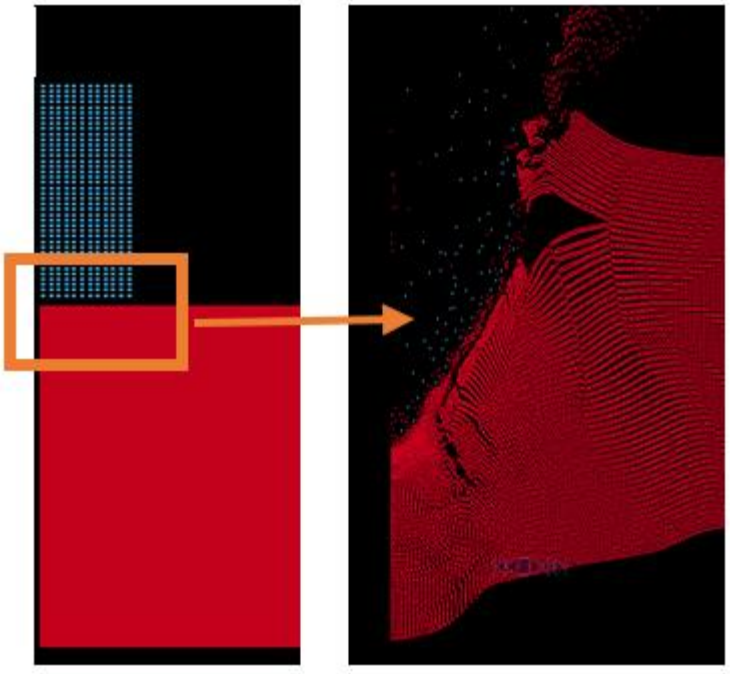

Figure 4.4: Typical damage results in single-layer simulation

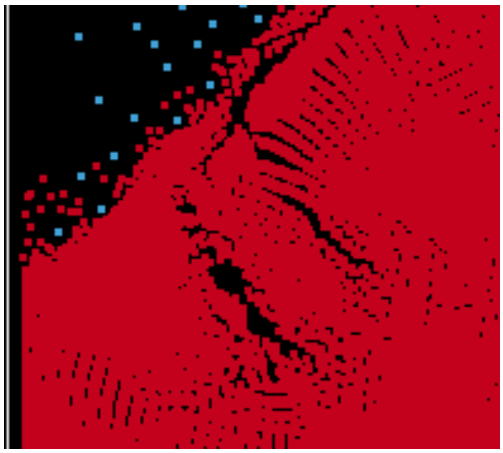

Figure 4.5: Spall formation in single layer simulation

In order to completely characterize the simulations; crater diameter, depth, and bulge were measured. In order to measure the crater diameter in the simulation, the top left node on the target was chosen for the reference location. Then three subsequent nodes, after damage

occurred, were chosen by where there was a crater. These values were averaged and then multiplied by two; because it is a 2-D axis-symmetric model. For the depth measurement a node was chosen on the top of the plate as the reference node. After the simulation ran, three nodes were chosen to the depth of the crater. Finally, an average of these values was taken to be the depth of the simulation. For the bulge measurement, the reference node was chosen to be a node on the bottom of the plate where there was no damage. After, three nodes were chosen at the peak of the bulge. The values were averaged and taken to be the bulge measurement. These measurements are then compared to the experimental values obtained. The results for the forged titanium simulation and experiment have been tabulated into Table 4.7. Due to the nature of simulations, the extensive time and the number of input variables, it is extremely difficult to perfect all aspects of the experiment. However, the simulation and experiment are well matched. In Figure 4.6, the results for crater diameter for the forged titanium alloy are graphically shown. The linear trend in the data have very similar slopes, however the magnitudes have some variance.

Table 4.7: Simulation and experimental deformation values for forged titanium alloy

Experiment	**Impact Velocity (km/s)**	**Crater Diameter (mm)**	**Penetration Depth (mm)**	**Back Surface Bulge (mm)**
Forged Ti Simulation	5.2	26	8.5	0.5
Experimental Forged Ti	5.2	18	6.3	0.3
Forged Ti Simulation	6.1	31	10.7	2.7
Experimental Forged Ti	6.1	21	6.4	2.6

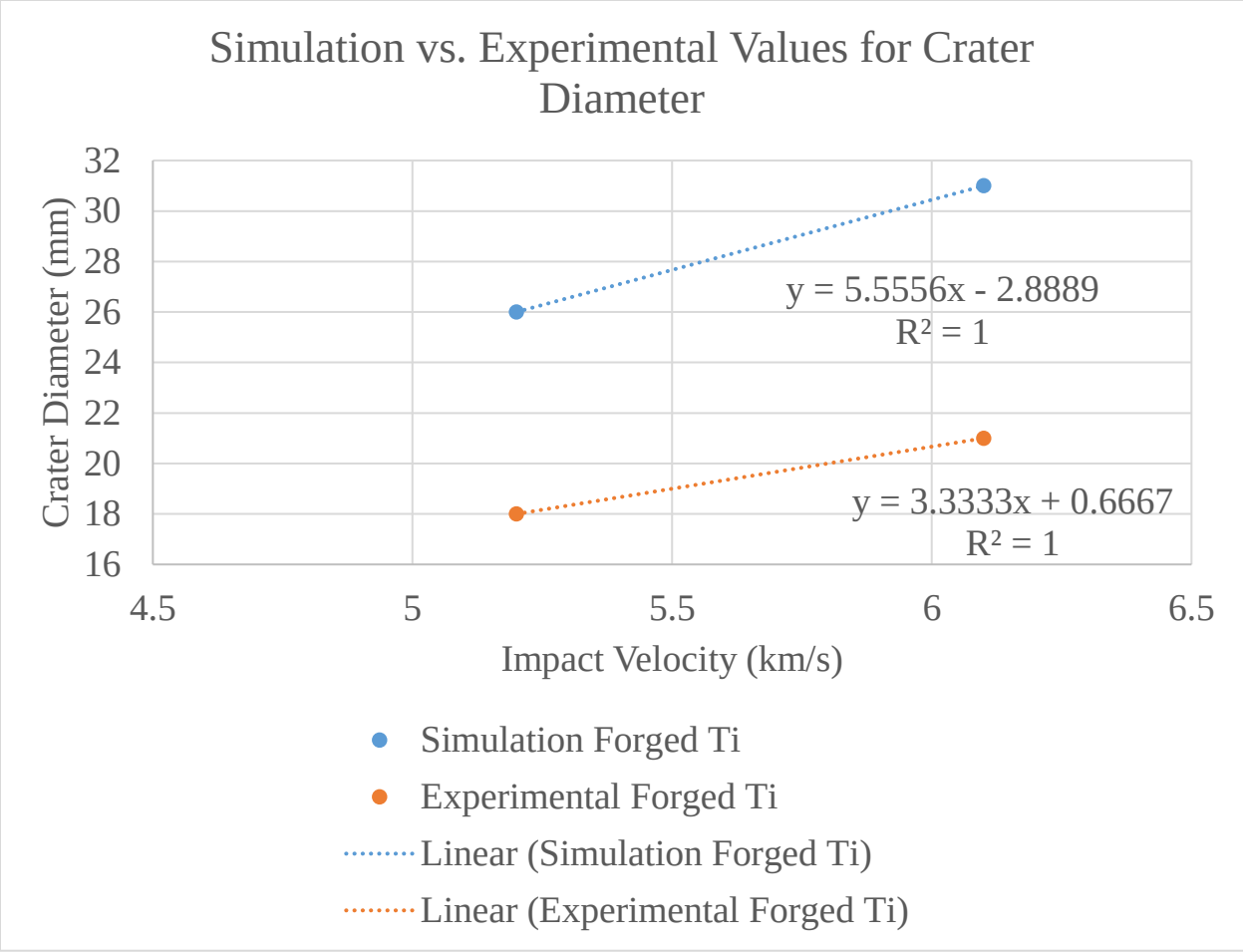

Figure 4.6: Simulation vs. experimental values for crater diameter for forged titanium alloy

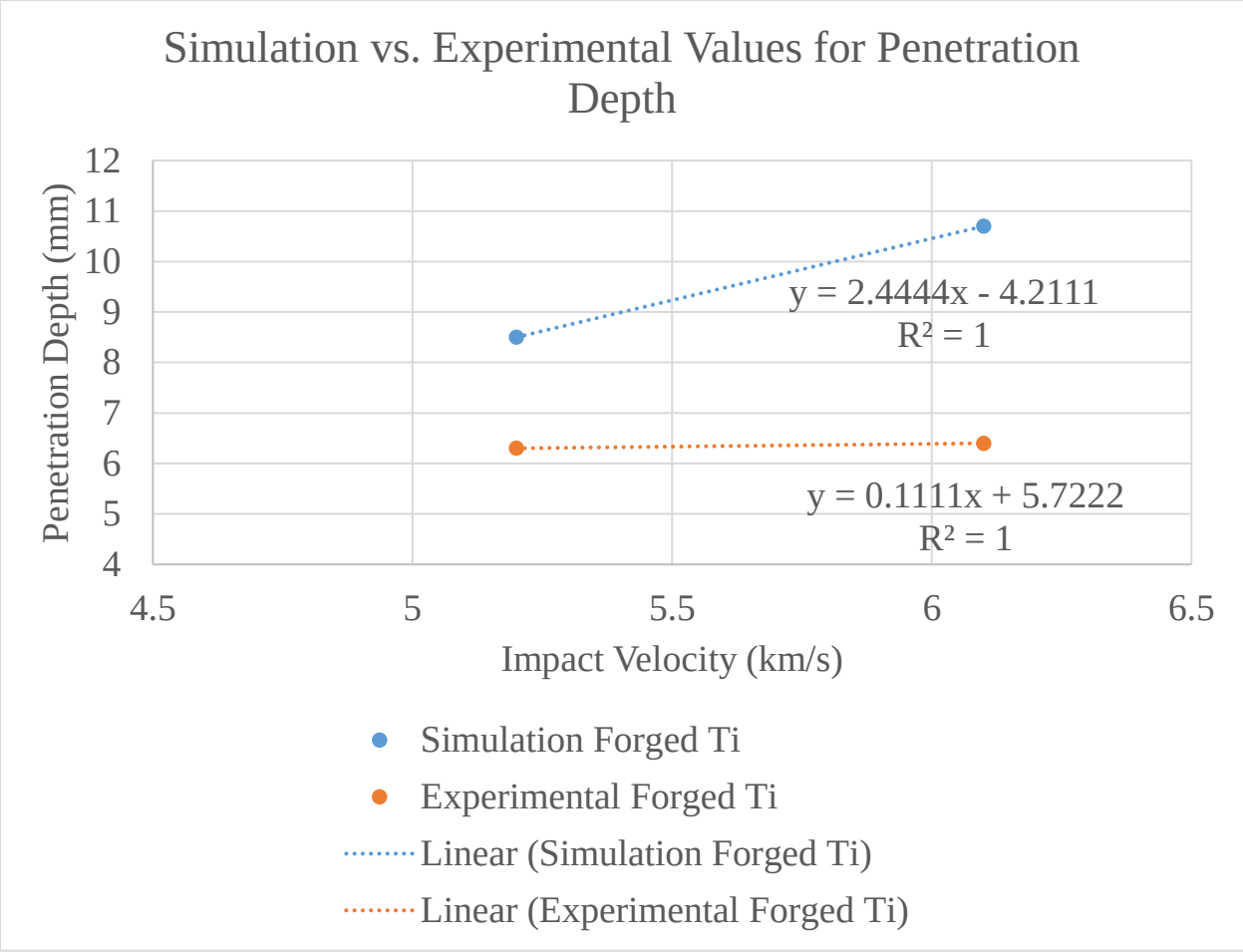

Figure 4.7: Simulation vs. experimental values for penetration depth of forged titanium alloy

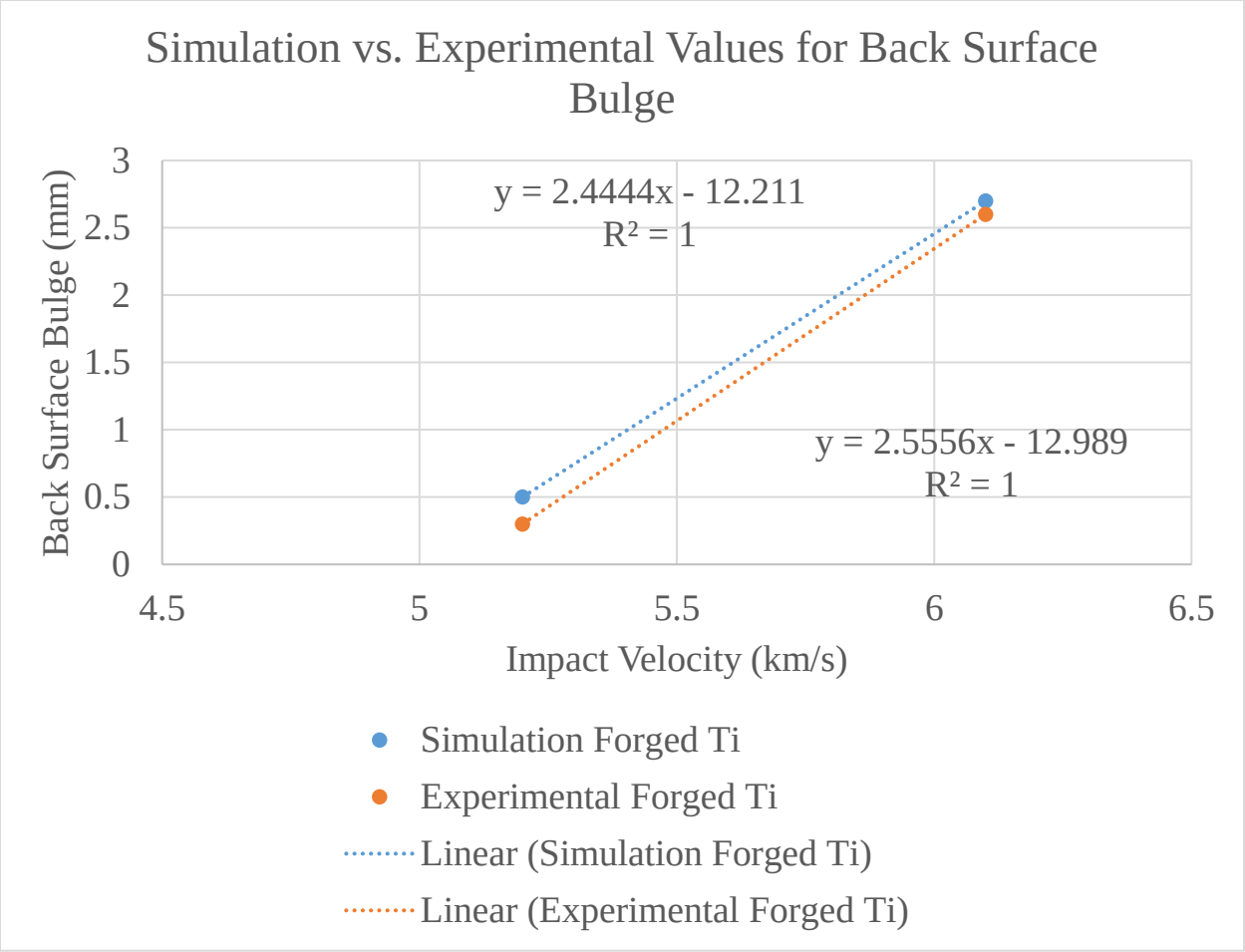

Figure 4.8: Simulation vs. experimental values for back surface bulge for forged titanium alloy

To simulate the AM titanium alloy, all mechanical properties in the models were reduced by 5%. This value was chosen from the manufacturer. The results of these finding are organized in Table 4.8. These results have some discrepancies. Since the AM material is very new and there are no documented dynamic material properties available, the results are reasonably matched. In order to fully understand the material, the properties measured in the experiment and in the simulation have been shown in Figure 4.9, Figure 4.10, and Figure 4.11. All the graphs have very similar slopes, with the back surface bulge having exactly the same slope. This means

the simulation results match reasonably well considering there is a lot to learn about these unique materials.

Table 4.8: Simulation and experimental deformation values for AM 'C'

Experiment	**Impact Velocity (km/s)**	**Crater Diameter (mm)**	**Penetration Depth (mm)**	**Back Surface Bulge (mm)**
AM 'C' Simulation	5.1	30	16	1.5
Experimental AM 'C'	5.1	20	6	1
AM 'C' Simulation	5.9	34	17	5.4
Experimental AM 'C'	5.9	23	8	4.9

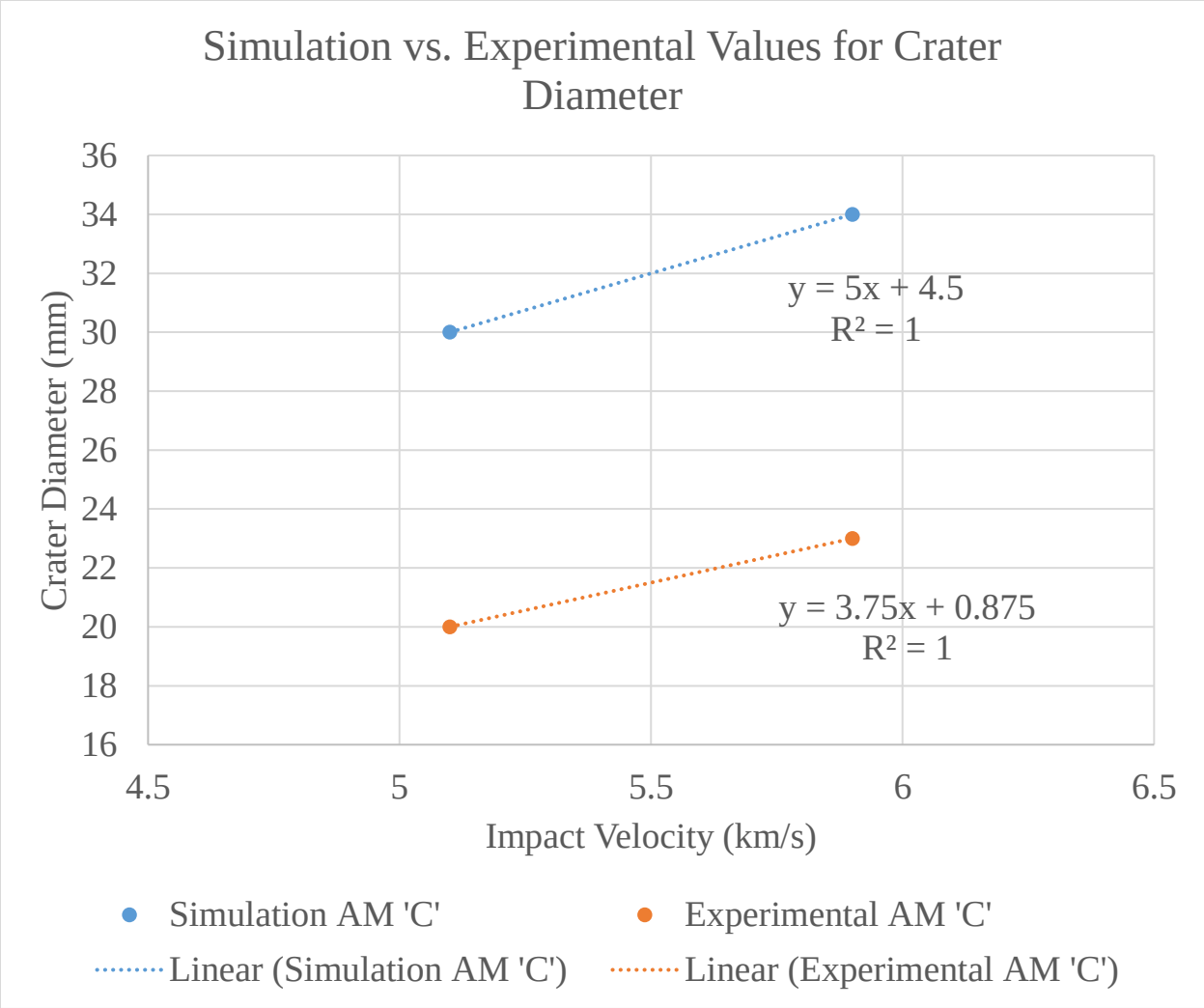

Figure 4.9: Simulation vs. experimental values for crater diameter for AM 'C'

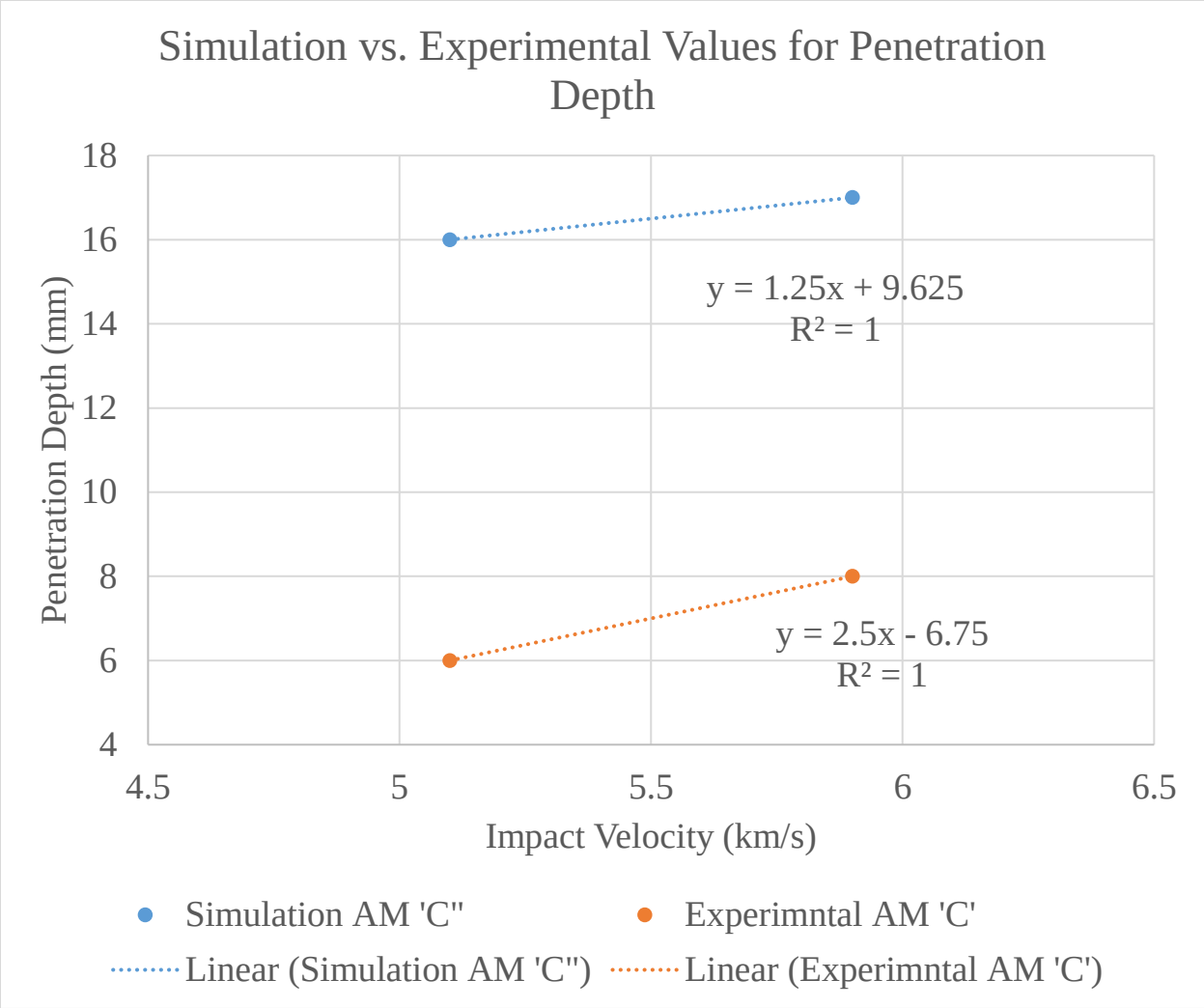

Figure 4.10: Simulation vs. experimental values for penetration depth for AM 'C'

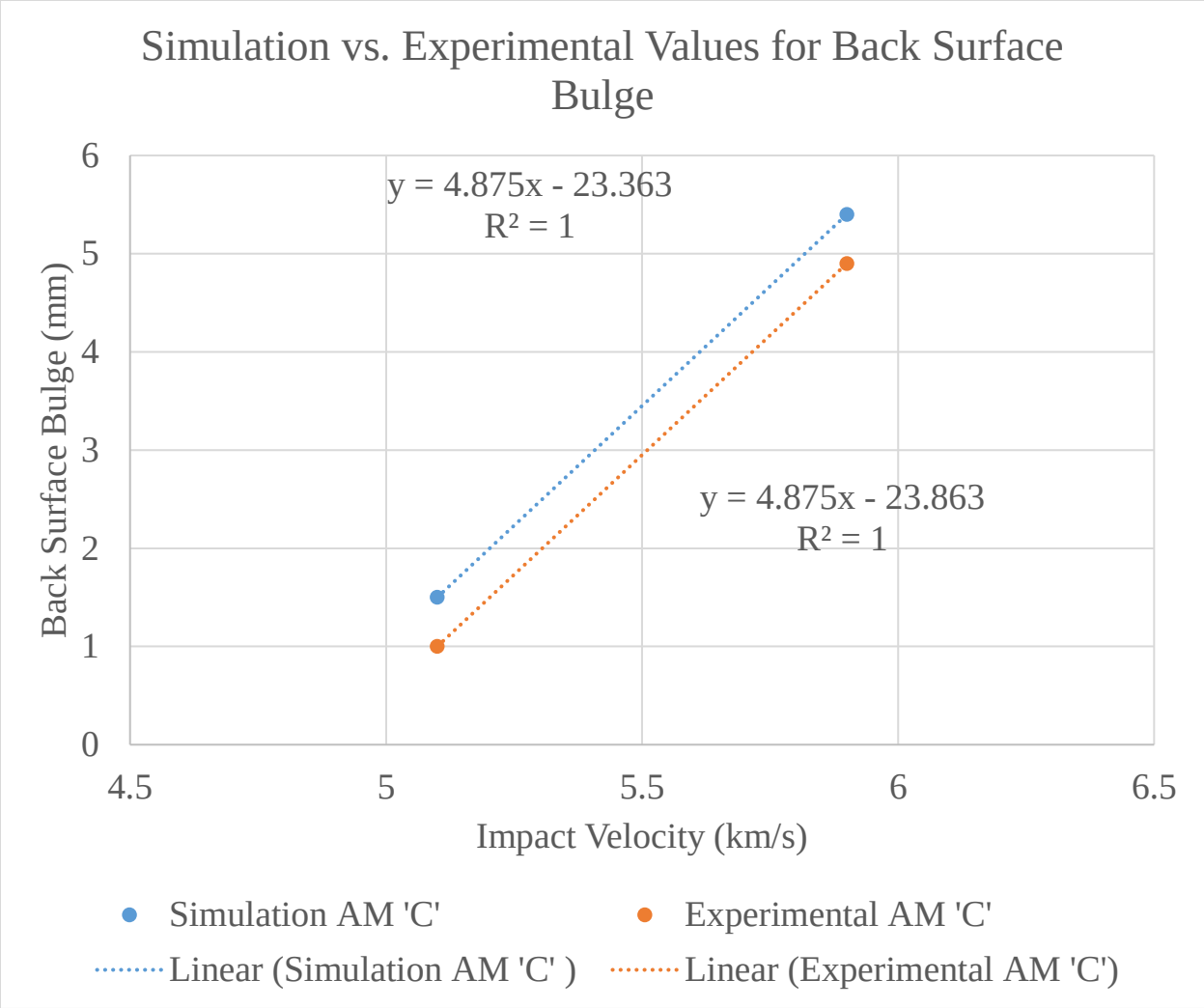

Figure 4.11: Simulation vs. experimental values for back surface bulge for AM 'C'

In the layered simulations, the plates deformed together, as if there was no gap between the plates at all. Figure 4.12 shows the typical results of the 2-layer simulation. The results show that there are some cracks that have formed similar to that of the real experiment; however, the simulation did not capture the way the top layer deformed in a separate manner. An increase in run time could possibly result in more deformation between the plates and also more crack formation.

Figure 4.13 shows the typical 4-layer simulation results. Although the results show there is more damage in the first plate and shows the gap in between the plates more than the 2-layer simulation, it did not capture how the first plate was completely penetrated by the projectile. A more in depth study on the computational code is needed to correct these simulations. The layered material became more complex to simulate. After many iterations with contact cards, the results still did not yield desirable results. Since the material does not have perfectly localized deformation, due to the small gap in between the plates, the simulation cannot mimic the experiment well. There is energy spent on the ringing in the plates and the material will spall in the first layers more easily than in the second layers and the simulation cannot capture this phenomenon. Instead in the simulations, the plates deformed together, as if there was no gap between the plates at all. Figure 4.12 shows the typical results of the 2-layer simulation. The results show that there are some cracks that have formed similar to that of the real experiment; however, the simulation did not capture the way the top layer deformed in a separate manner. An increase in run time could possibly result in more deformation between the plates and also more crack formation. Figure 4.13 shows the typical 4-layer simulation results. Although the results show there is more damage in the first plate and shows the gap in between the plates more than the 2-layer simulation, it did not capture how the first plate was completely penetrated by the projectile. However, there is no way to experimentally determine if there is particles from the first plate embedded into the second plate. A more in depth study on the computational code is needed to correct these simulations.

Table 4.9: Experimental and simulation deformation values for layered forged titanium alloy

Experiment	Impact Velocity (km/s)	Crater Diameter (mm)	Penetration Depth (mm)	Back Surface Bulge (mm)
Forged 2-layer Simulation (a)	5.5	14	6.6	3.1
Forged 2-layer Simulation (b)	5.5	20	6.0	1.8
Experimental Forged 2-layer (a)	5.5	10	2.1	2.7
Experimental Forged 2-layer (b)	5.5	23	1.5	0.9
Forged 4-layer Simulation (a)	5.6	18	NA	NA
Forged 4-layer Simulation (b)	5.6	14	9.0	4.0
Forged 4-layer Simulation (c)	5.6	13	6.0	3.3
Forged 4-layer Simulation (d)	5.6	26	6.0	3.0
Experimental Forged 4-layer (a)	5.6	25	NA	NA
Experimental Forged 4-layer (b)	5.6	19	4.3	3.2
Experimental Forged 4-layer (c)	5.6	17	2.7	3.0
Experimental Forged 4-layer (d)	5.6	27	2.4	2.2

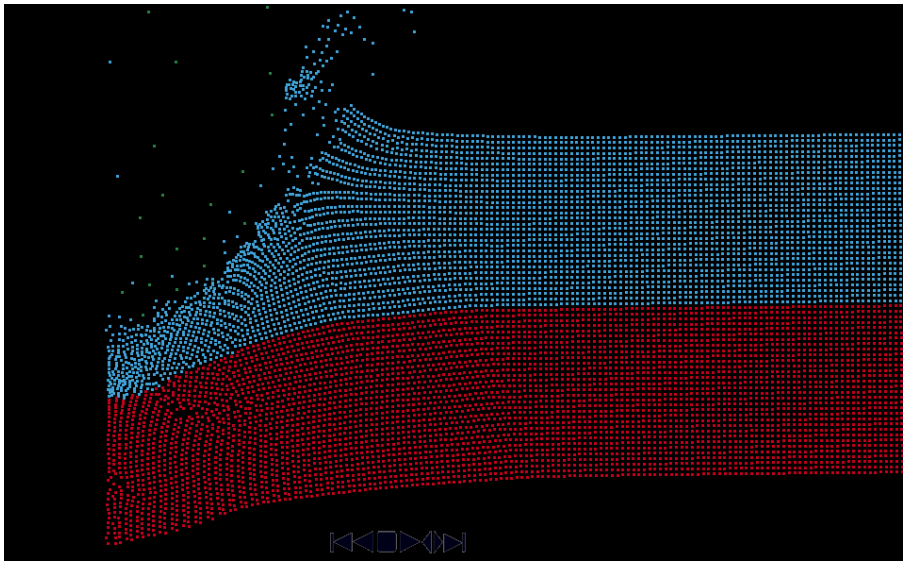

Figure 4.12: 2-Layer simulation

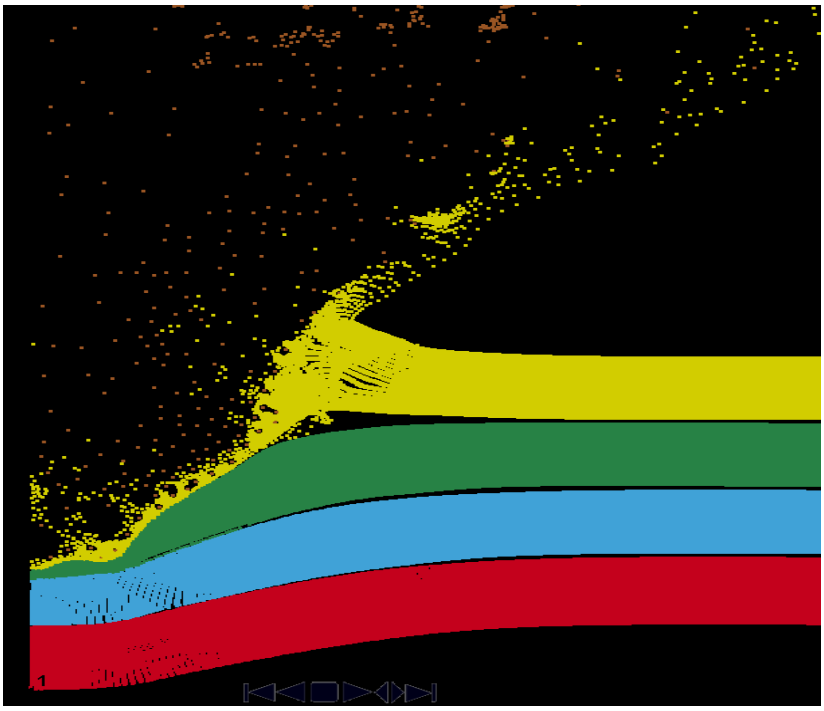

Figure 4.13: 4-Layer simulation

4.8 SIMULATION VELOCIMETRY RESULTS

Another aspect of the simulation that can be compared to the experimental results is the free surface velocity profiles. The velocity profile of the simulation was collected by using the node at the center of the impact. The experiment was set up with the hope that one of the four probes of the PDV was pointed at the impact center. This probe was typically probe number 1. It is probe number one's velocity trace that is compared to the simulation velocity trace. The velocity trace for the forged material at 6.1 km/s is shown in Figure 4.14. LS-DYNA® is able to resolve the shape and magnitude of the velocity curve but does not do well in the first few microseconds. It does not capture the elastic precursor wave nor the HEL. The plastic wave and the elastic unloading have the same shape, but slightly different magnitudes. Figure 4.15, shows the simulation for the AM 'C' material. This also has the same critical flaws as the forged titanium alloy simulation. It is able to capture the magnitude and the shape of the curve, but does

not capture the elastic precursor wave nor the HEL.

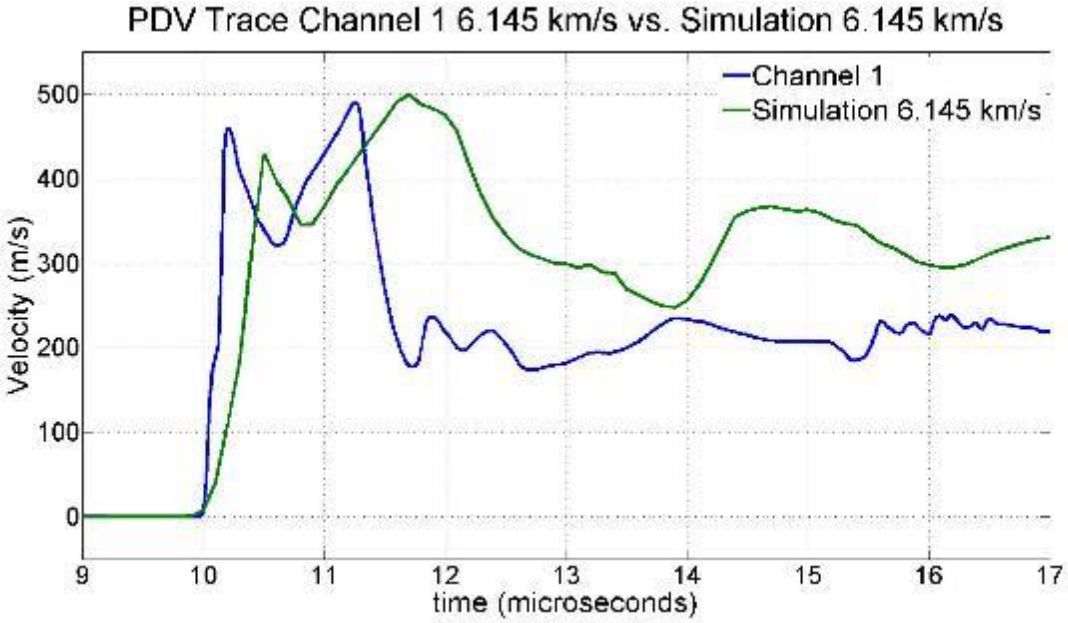

Figure 4.14: Simulation of forged 12.7 mm free surface velocity trace

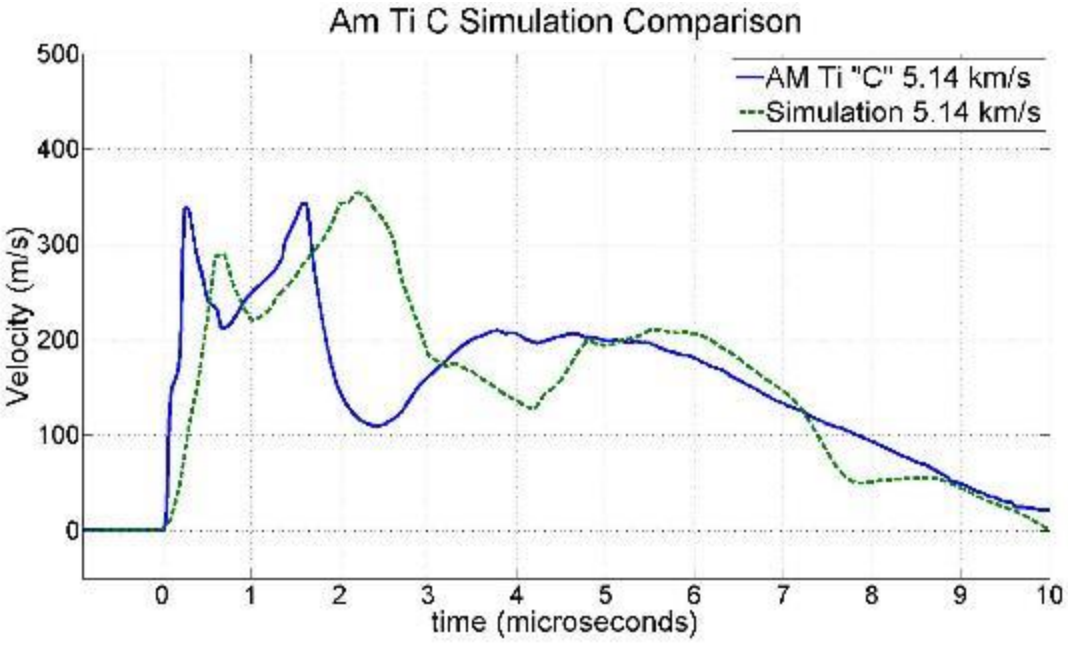

Figure 4.15: Simulation of AM 'C' free surface velocity trace

Since the experimental data revealed that the velocity profiles of the forged titanium alloy and the AM material were very similar it became of interest to plot the simulations and the experimental data. The simulation of the velocity at around 5.1 km/s is depicted in Figure 4.16. To see if velocity had an effect on the material damage and velocity trace, a higher velocity of about 5.9 km/s was chosen. The free surface velocity results are shown in Figure 4.17. At the higher velocity the simulations were able to capture the slope of the elastic wave better than at the lower velocity. However, the simulation did not capture the elastic precursor wave nor the HEL. Shape and the magnitude of the free surface velocity curves at the higher velocity are very similar.

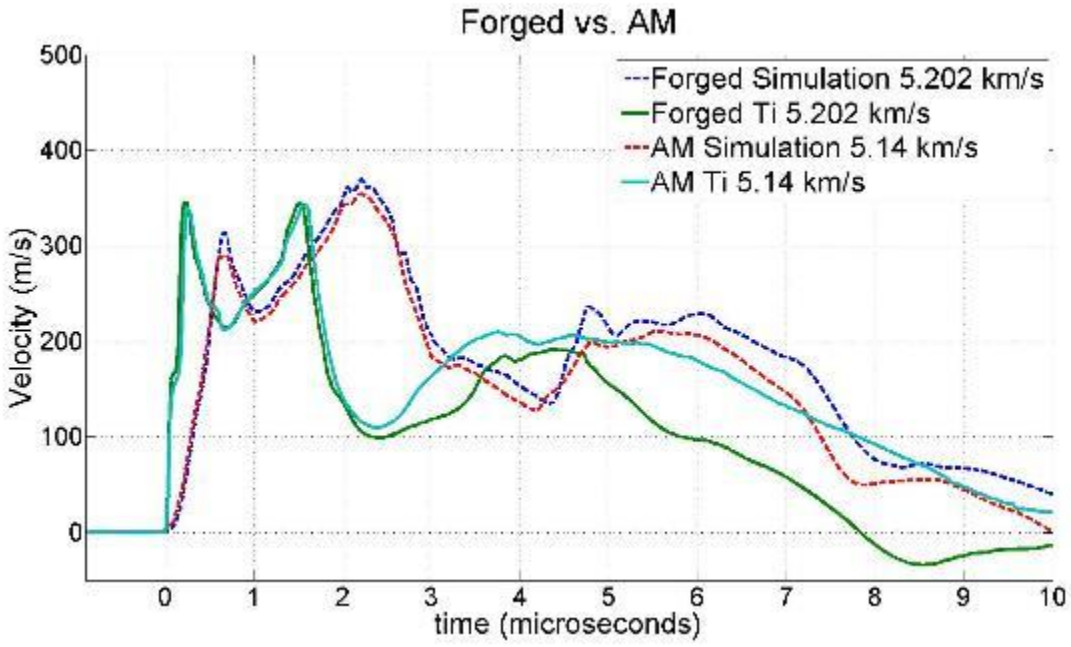

Figure 4.16: Forged and AM 'C' simulation comparison of free surface velocity at about 5.1 km/s

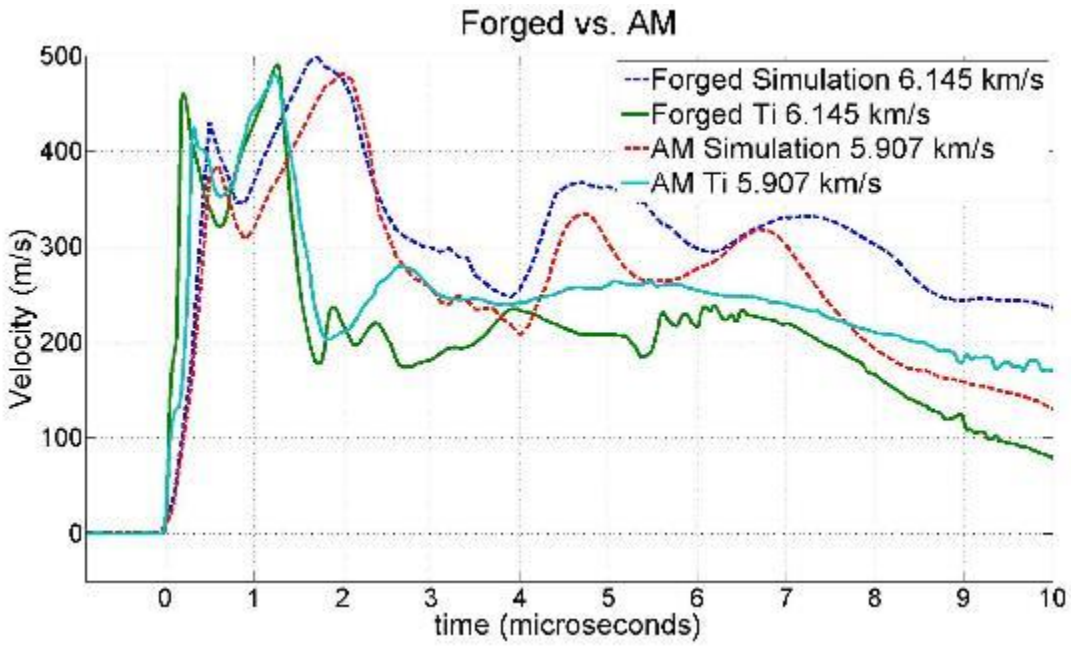

Figure 4.17: Forged and AM 'C' simulation comparison of free surface velocity at about 5.9 km/s

The layered material's simulated velocity data was chosen in the same fashion as with the single-layered data. That is, taking a node at the center of the impact crater to compare to the experimental data. Figure 4.18 shows the results of the 2-layer simulation of free surface velocity and compares it to the experimental results of the first probe of the PDV. Just like in the single-layer material the simulation performed well at capturing the shape and magnitude of the curve, but the simulation did not have the elastic precursor wave. Figure 4.19, shows the free surface velocity results of the 4-layer simulation. During the experiment it was hard to interpret the velocimetry data. The curve did not have a distinguished elastic precursor nor did it have the typical two wave velocity profile like with the other materials. Instead, it is thought that the vibration in the plates were interfering from collection of good data. The simulation shows a severe failure in the code, represented by the curve not returning to zero. This code failure typically means that the spacing between the nodes is too large. An attempt at decreasing the

spacing size, or increasing the amount of nodes, was conducted however, there was not enough computational power. Trying to start the simulation of the more dense code resulted in the servers crashing. Increasing the computing power to run the simulations could yield better results.

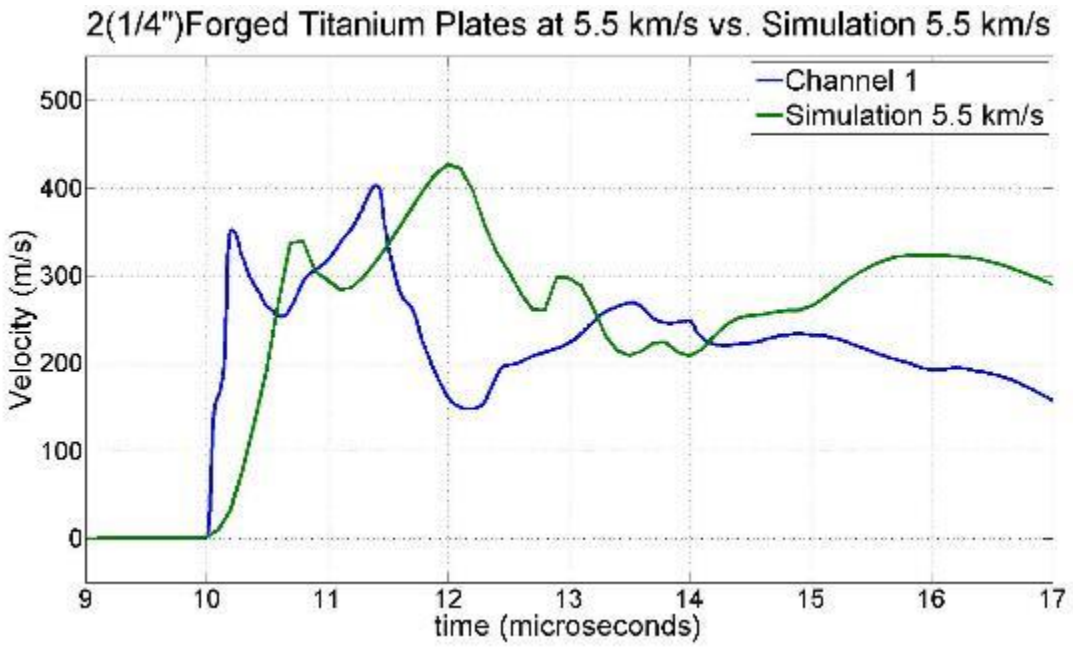

Figure 4.18: 2-layer simulation of free surface velocity results

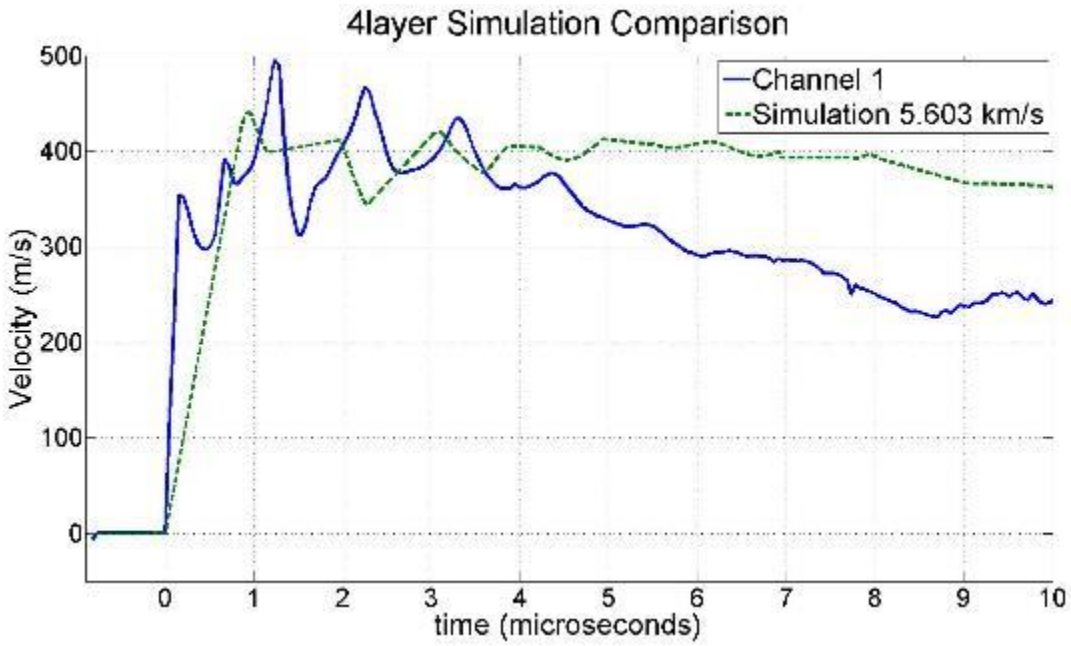

Figure 4.19: 4-layer simulation of free surface velocity results

5. DISCUSSION

5.1 PHYSICAL CHARACTERISTICS COMPARISON BETWEEN TARGETS

The main goal of this work was to compare the impact characteristics of forged, layered, and additively manufactured titanium alloy. The reason these types of targets were analyzed is due to the way that the AM material was manufactured. It was originally thought that the AM material would exhibit both forged and layered material characteristics. However, it was determined that the AM material did not exhibit any of the features of the layered material. The layered material revealed unique results that may be attributed to the freedom of the layers to move with respect to each other, even though they were bolted together. A better experiment may be to bond the plates together.

Ti-6Al-4V is an $\alpha + \beta$ phase material at room temperature [57]. At higher temperatures, the β-phase increases [58]. The method used to produce the AM parts may increase the percentage of β-phase present. β-phase is considered to have lower strength at elevated temperatures than the α-phase [59]. If the AM target had more β-phase; then under hypervelocity impact conditions it would cause faster failure of the material. Microscopic analysis of phase transitions in these materials was beyond the scope of this effort. Additional microscopy is needed to fully understand the complexities of the microstructure of the AM target.

Another interesting failure mode that was observed in the forged and AM targets is adiabatic deformation. From chapter 3, the cross-sectional images of the damage results show these white bands against the dark grey bands. The term “adiabatic” is used, although not completely true, to describe the behavior of plastic deformation where most of the energy is converted to heat [60]. This phenomena is most apparent in phase transformation steels, as a white band against a dark grey band and described as adiabatic shear bands [61]. It was shown

that titanium alloys exhibit these adiabatic shear bands and is what has been described as shearing or plugging. These adiabatic shear bands have been well characterized for Ti-6Al-4V. In more β-phase titanium, adiabatic shear is a leading failure mode [61]. When the AM 'A' material in Figure 3.5 showed the severe shear failure, which is understood now as adiabatic shear, this observation supports the hypothesis that AM targets may have developed more β-phase crystals.

5.2 FREE SURFACE VELOCITY PROFILE COMPARISON BETWEEN TARGETS

During the shock experiments, free surface velocity data was collected using the PDV. This velocity data can reveal dynamic material property behaviors. The single-layer forged titanium alloy and additively manufactured titanium alloy targets had velocity traces with similar shapes, but the magnitudes of the elastic precursor wave and the plastic wave varied for similar impact velocities. With the highest variations in the magnitudes being less than 50 m/s. The 2-layer target with an impact velocity of 5.5 km/s showed a velocity trace similar to the single-layer and AM targets, but a repeat of the same experiment shows completely different results. The 4-layer experiments had similar erratic results. This could have been improved by perhaps having the plates bonded together

LS-DYNA® SIMULATION PHYSICAL DAMAGE COMPARISON

The physical damage results from all of the target simulations were well documented. Then these damage results were compared to the experimental data. Unfortunately, the physical damage characteristics varied from simulation to simulation. Sometimes the simulation would have good correlation to the experimental data; in other cases it did not. The back surface bulge in the forged simulation experiments varied about 0.2 mm; whereas the crater diameter varied 10 mm. The penetration depth varied about 4 mm. Then in the AM simulation, the back surface

bulge varied 1 mm, the crater diameter varied 10 mm, and the penetration depth varied 10 mm. The back surface bulge in both cases had the least amount of variance. Due to the complexity of the simulations and the run time constraints, it became a bottle necking issue for more accurate simulations. However, a modified Johnson-Cook material card could be the most useful for future studies. This new Johnson-Cook could have a modified temperature equation that could account for the phase-transformation and adiabatic transformation. Additional microscopy could help reveal how the spall forms at the grain boundaries and experts can modify the material models by understanding the physics better to get more accurate simulation results.

5.3 LS-DYNA® SIMULATION FREE SURFACE VELOCITY COMPARISON

The free surface velocity trace was extracted on the point in the center of the crater. This point was used to correspond to the probe closest to the center of the crater from the PDV. The single-layer and AM target's velocity traces had good correlation to the simulation. The magnitude and the shape of the velocity curve were similar. The only feature that was not captured was the elastic precursor wave. This elastic precursor wave can detail the Hugoniot Elastic Limit. Since the simulation could not capture this precursor wave, focusing on how to improve the slope of the precursor wave may improve the overall results of the simulation. Changing the 'A' node in the Johnson-Cook model could improve the first phase of the simulation. The HEL, as previously mentioned, is the point the solid material behaves more like a fluid. Trying to improve the velocity trace could lead to more accurate simulation results.

6. CONCLUSIONS AND FUTURE WORK

This chapter provides a summary of all the research completed to accomplish the objectives of this work. Suggestions to further ascertain new challenges these unique materials provide are also presented.

Hypervelocity impact experiments are difficult to conduct and can be very expensive. Due to the complexity of the experiment, sophisticated diagnostic instrumentation is needed to provide data. The experimental data collected, deliver dynamic material behavior characteristics that can be used to design components that operate in extreme conditions. This research concentrated on studying plastic deformation of forged, layered, and additively manufactured titanium alloy, Ti-6Al-4V. This particular alloy is extensively used in the aerospace and defense industries.

In order to explore these unique materials, an experiment was designed where plates of these three materials were subjected to non-penetrating impact by projectiles accelerated by a two-stage light gas gun. The velocities explored ranged from 5.0 – 6.6 km/s. The experiment was created, such that, the projectile impact would produce a bulge on the back surface. Post-mortem analysis of crater diameter, penetration depth, and bulge height were documented.

To enhance understanding of failure mechanisms, it is important to study the behavior of these materials, during the experiment. This requires unique diagnostic equipment. There have been several efforts to develop diagnostics in this field. The diagnostic system used in these experiments was a Photonic Doppler Velocimetry (PDV) system. PDV systems have been shown to provide extremely useful data that can provide insight to the material's dynamic behavior.

The main focus of this work was to characterize the dynamic behavior of additively manufactured (AM) titanium alloy. AM techniques have only recently been utilized and have the potential for tailoring geometry and optimizing structural performance. Since this manufacturing technique is unique and fairly recent, not much was known about the behavior of AM components compared to forged titanium alloy and layered targets. The research hypothesis was that the AM plates may have mechanical characteristics that are somewhere between forged and layered counterparts. All experiments were conducted to characterize the impact properties in forged, layered, and additively manufactured titanium alloy. This included both physical damage properties and free surface velocity results. This data revealed details about these materials that help scientists and engineers alike to understand the plastic deformation of the AM materials under shock loading.

Another critical objective of this work was to simulate the impact of the Ti-6Al-4V plates. A 2-D axis-symmetric model, that had previously been used to study impact on steel plates, was utilized with an SPH solver in LS-DYNA®. SPH was employed because of its ability to simulate large localized deformation by simulating the fluid-like behavior of solids under hypervelocity impact. This can be advantageous to meshed FEA solvers. A well-known shock material model called Johnson-Cook was implored to capture the high strain rate and deformations of the experiment. The Mie-Grüneisen Equation of State was used to simulate the shock properties of the titanium alloy. Even though the spall-strength was estimated using experimental data, the spall-strength found in the literature provided a better correlated material model for the simulations. Estimated spall strength in the experimental data is not found under uniaxial strain. The simulations' spall strength is calculated using uniaxial strain conditions and

therefore using the estimated spall strength is not a good match. The limitation of the computer hardware did not allow for a decent model of the layered material.

The SPH simulations were compared to the experimental results. The simulation results included both physical damage characteristics (crater diameter, penetration depth, and bulge height) and the free surface velocity traces. Back surface bulge height had reasonable agreement with the experimental results and the crater diameter and penetration depth did in only a few of the cases. The layered material model deformed in such a fashion that was unrealistic, that is, the plates deformed together instead of creating gaps seen in the experimental data. For this reason, no comparison should be considered. The free surface velocity extracted from the simulations were able to capture the magnitude and the shape of the single-layer plates. However, the elastic precursor wave did not have good agreement. The velocity traces for the layered case showed a critical failure. This failure is usually associated with not enough nodes in the model. Increasing the amount of nodes resulted in crashing the servers.

The final objective of this work was to develop an approach to modeling the AM titanium alloy. This was completed using the same 2-D axis-symmetric model from the forged simulations. The difference was in the material model and the EOS; the mechanical properties were reduced by 5% reflecting the data provided by the manufacturer. The physical damage characteristic had similar results to the forged part. That is, the back surface bulge had good agreement to the experimental results, but the crater diameter and the penetration had good agreement in only a few cases. The free surface velocity trace results showed good agreement with the magnitude and the shape, but failed to capture the first phase of the experiment.

Retrospectively, there are aspects of the experiments that could be changed and should be changed for future experiments. Maya Angelou said it best, “I did then what I knew how to do.

Now that I know better, I do better." Ultimately, this work was able to meet all of the major objectives. However, there are numerous areas that could be improved and explored further. The following is a list to outline what could possibly be done to further understand the unique materials studied in this work.

1. Testing layered materials showed that they behave in a significantly different manner than AM and forged plates. It is recommended that future studies focus on layered and AM targets.
2. Since Ti-6Al-4V is an α-β phase, additional microscopy to quantify the difference in the AM and forged material would help understand the failure modes better.
3. These experiments only utilized 4-probe PDV arrangement. Additional PDV probes or the additional of MPDV could help to completely understand the AM target.
4. The simulations were completed using an SPH solver. Different meshing solvers should be explored.
5. The material model and the equation of state for the simulations were obtained from the literature. By completing fundamental shock experiments, it is possible to derive the details of the physics models and could produce better outcomes.
6. A more in-depth study of phase transformation and the effects it has on the simulation should be completed to provide more accurate models.

APPENDIX A. GRAPHICAL REPRESENTATION OF PDV PROBE LOCATIONS

After each experiment, an infrared detection card was used to mark the back surface of the plate to indicate the location of the probes. After the experiment, the marked locations were measured with respect to the impact center. The following shows the graphical representations of the probe locations. All axes are in terms of mm, the blue dots represent the probe locations while the orange dots represents the impact center. Shot 1 has been excluded due to inconclusive PDV data and the last shot due to spall damage on the back surface.

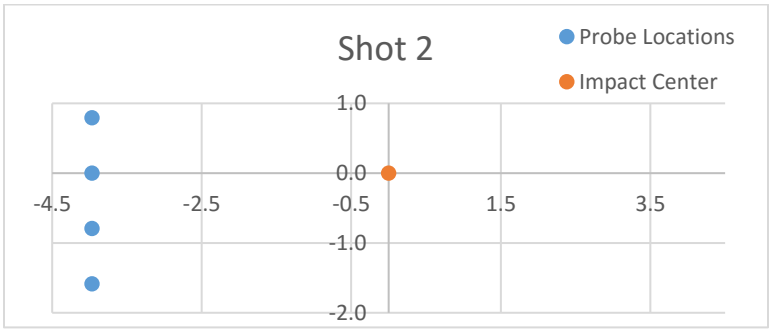

Figure A.1: Shot 2 probe locations

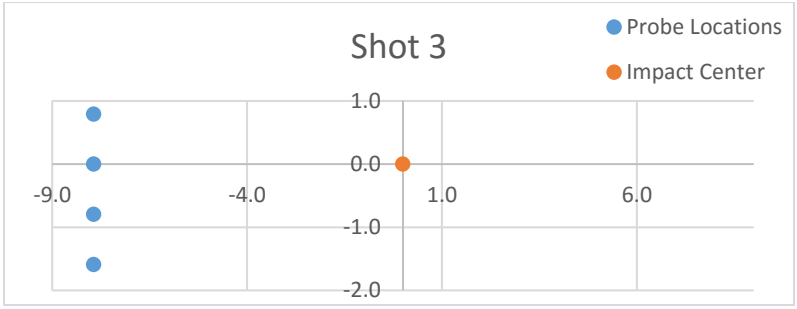

Figure A 2: Shot 3 probe locations

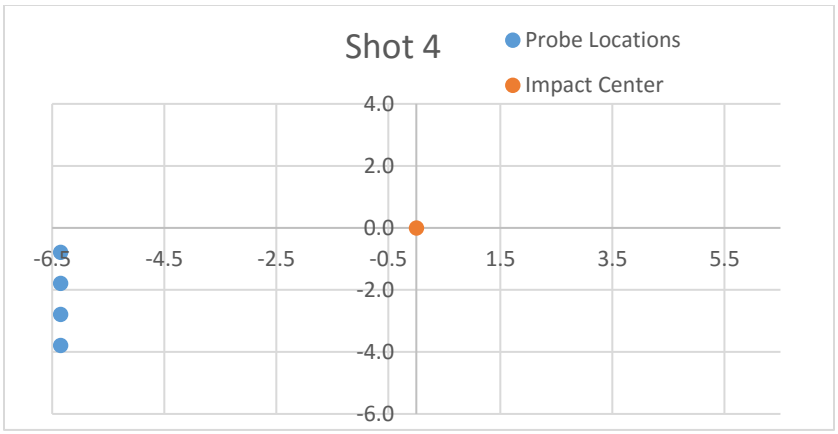

Figure A.3: Shot 4 probe locations

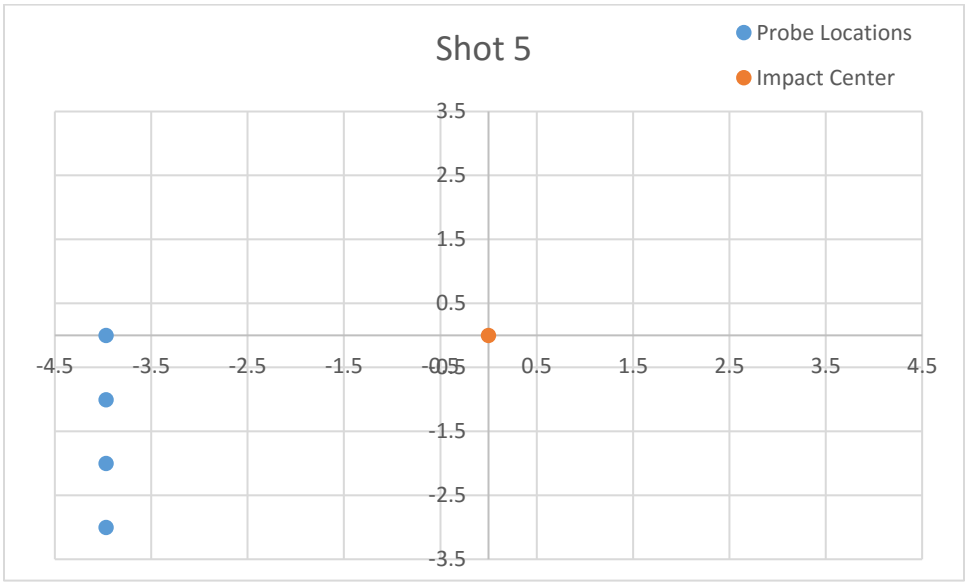

Figure A.4: Shot 5 probe locations

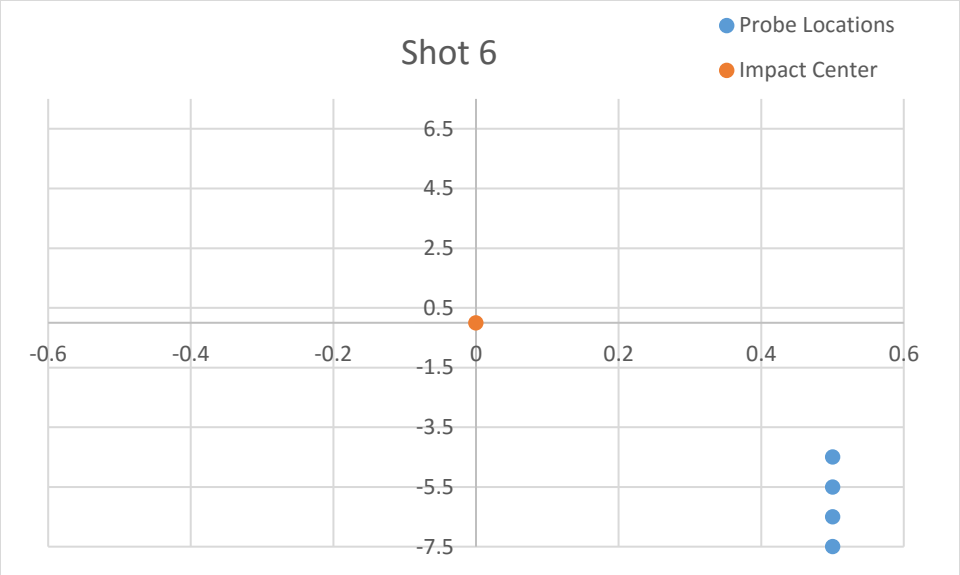

Figure A.5: Shot 6 probe locations

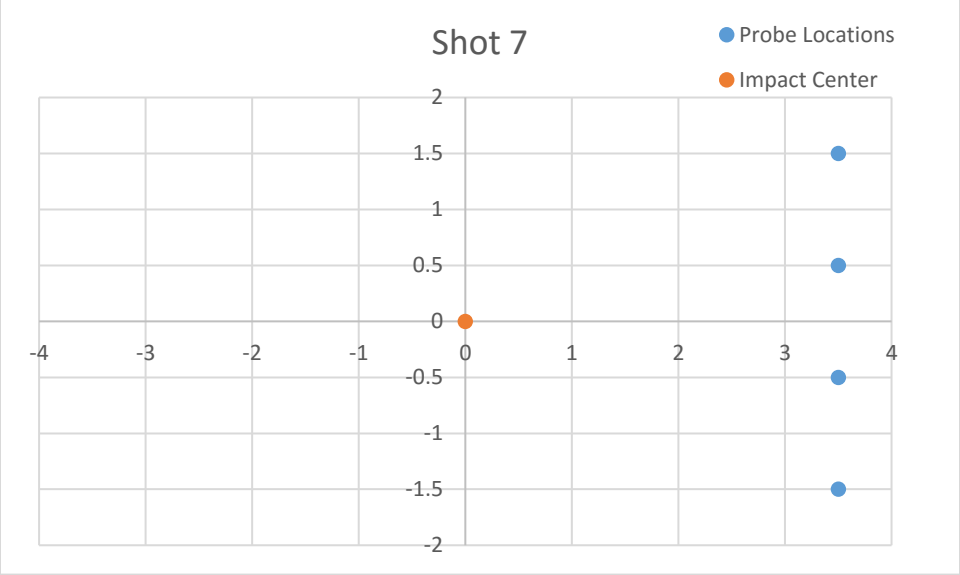

Figure A 6: Shot 7 probe locations

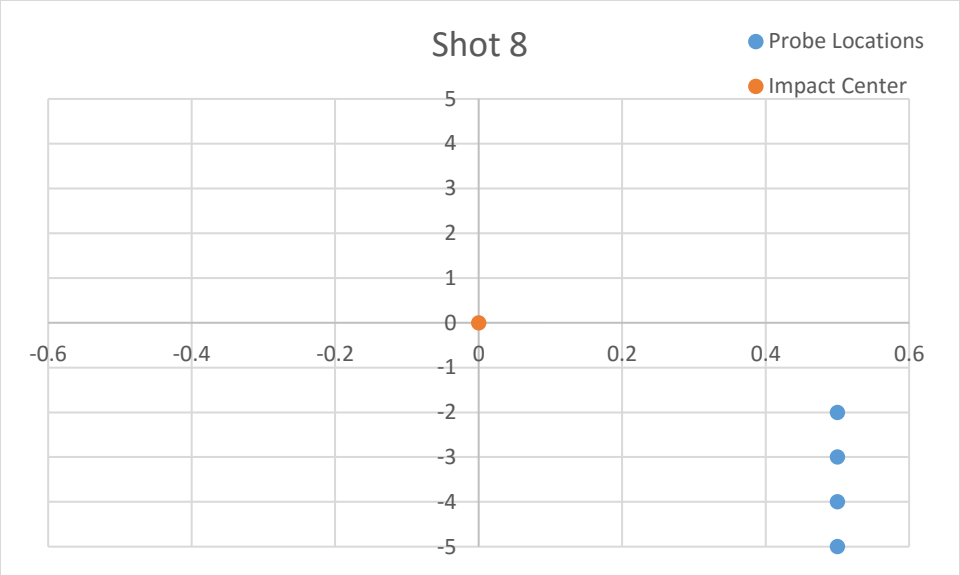

Figure A.7: Shot 8 probe locations

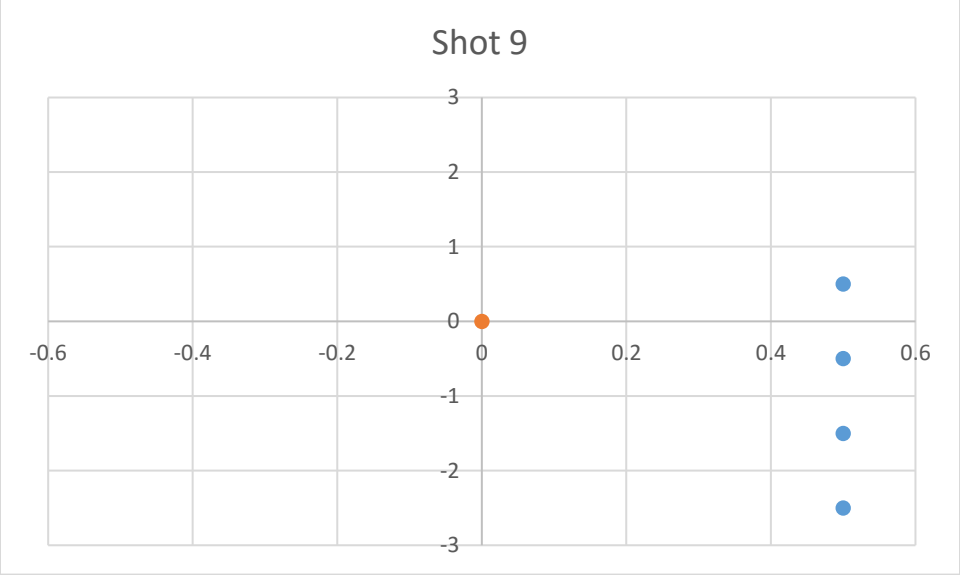

Figure A 8: Shot 9 probe locations

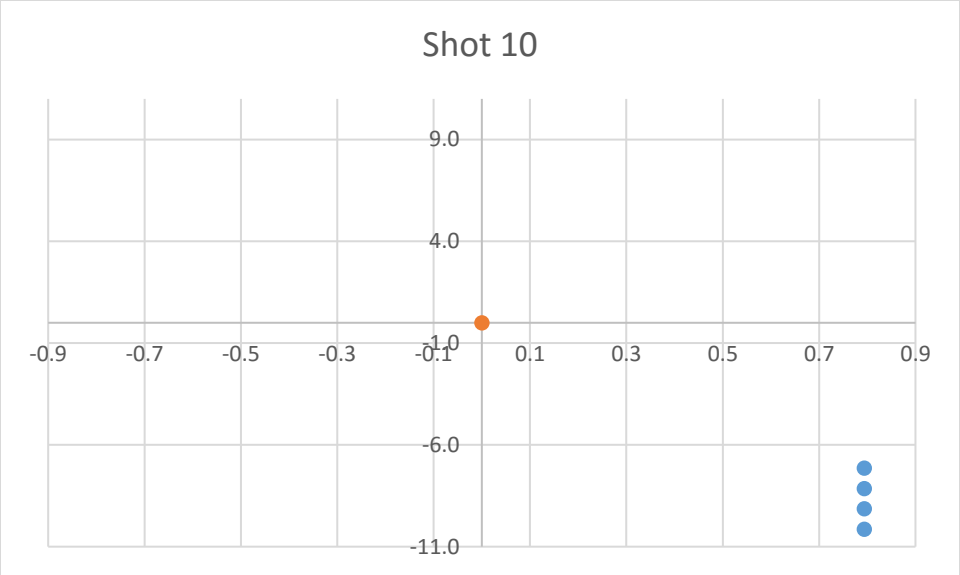

Figure A.9: Shot 10 probe locations

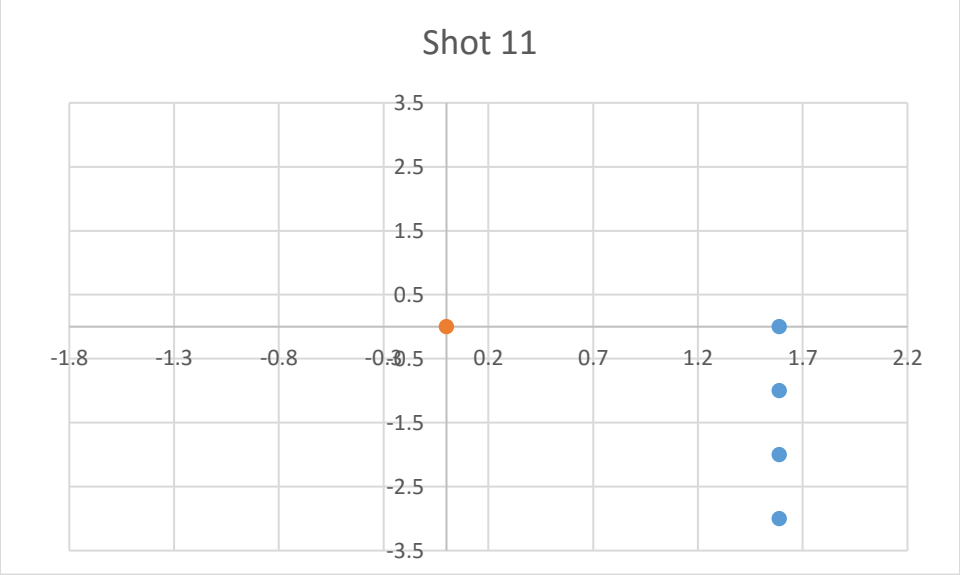

Figure A.10: Shot 11 probe locations

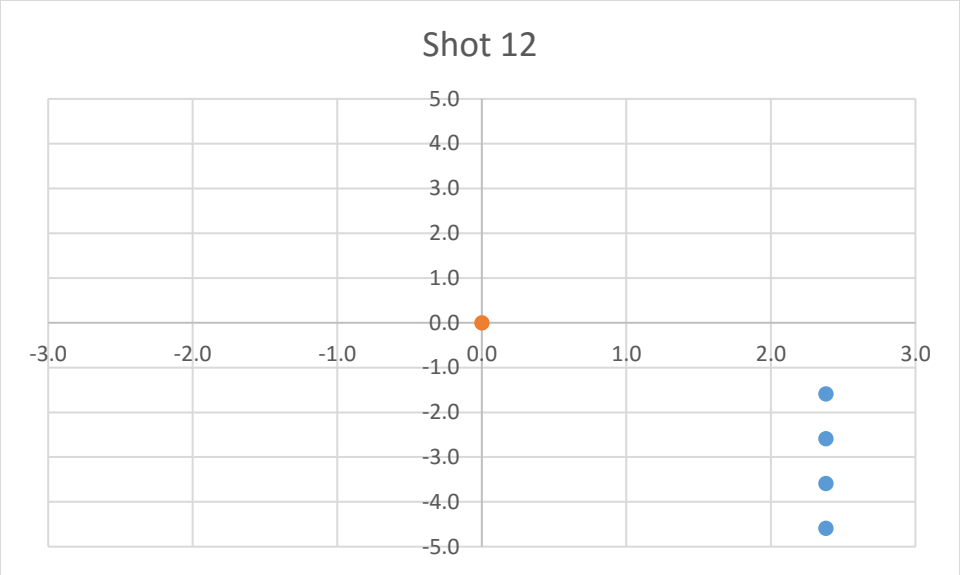

Figure A 11: Shot 12 probe locations

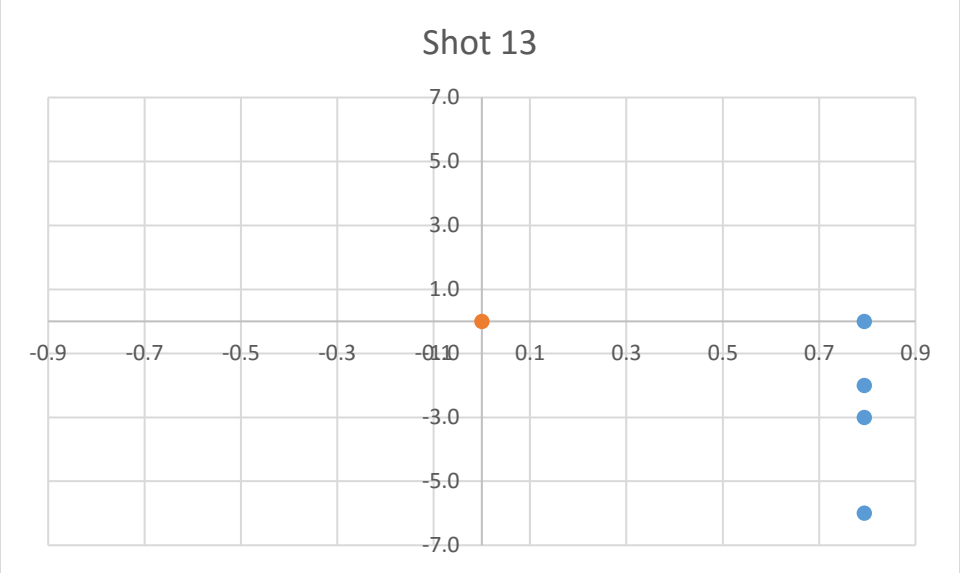

Figure A.12: Shot 13 probe locations

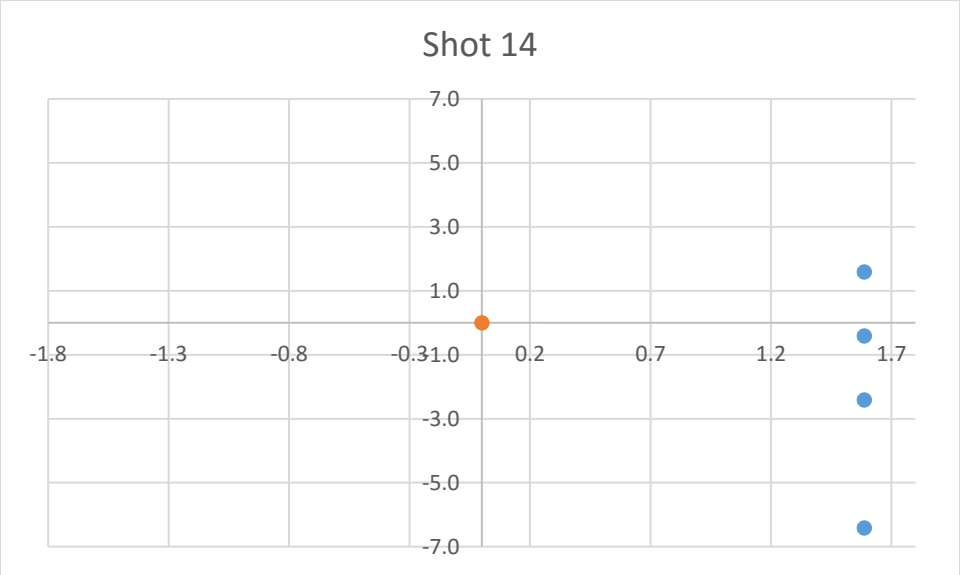

Figure A.13: Shot 14 probe locations

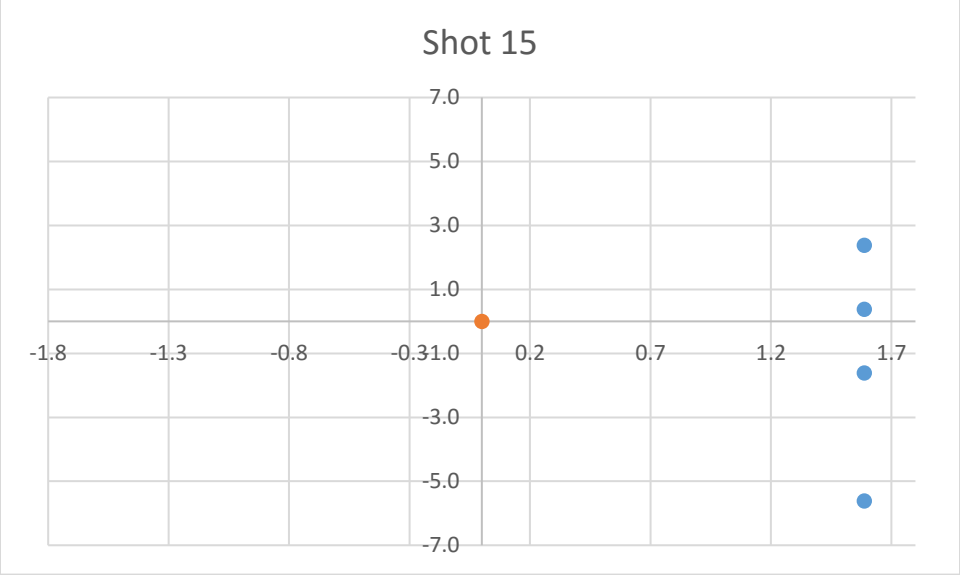

Figure A.14: Shot 15 probe locations

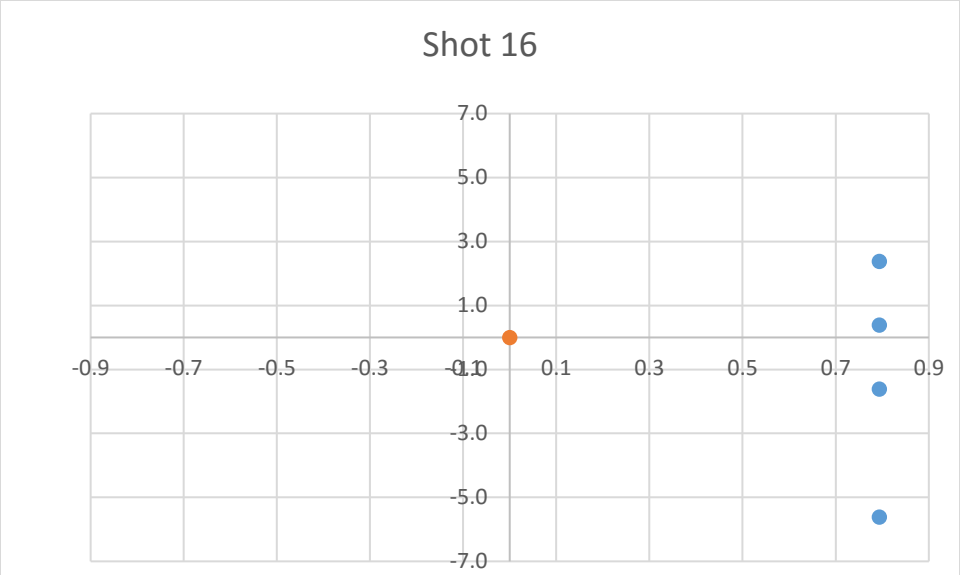

Figure A.15: Shot 16 probe locations

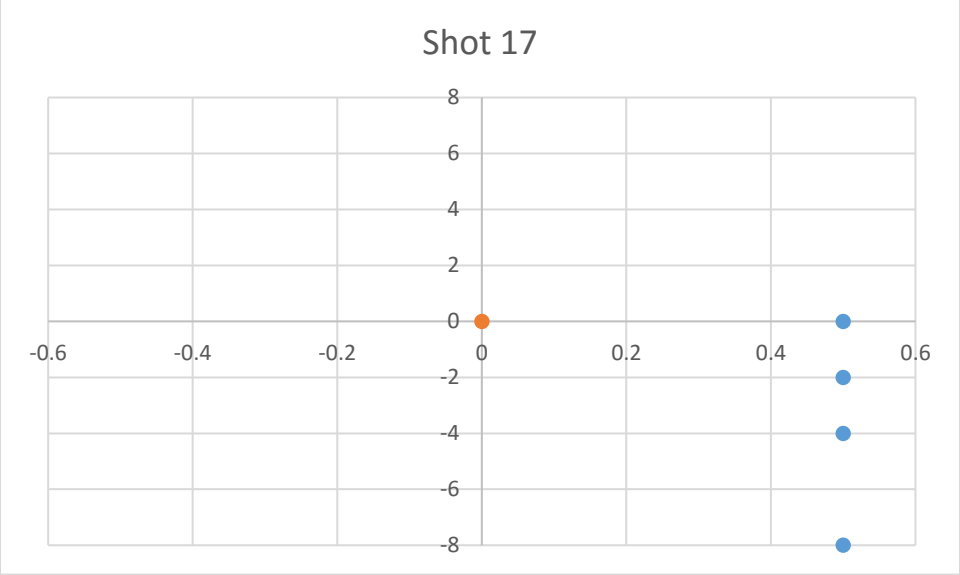

Figure A.16: Shot 17 probe locations

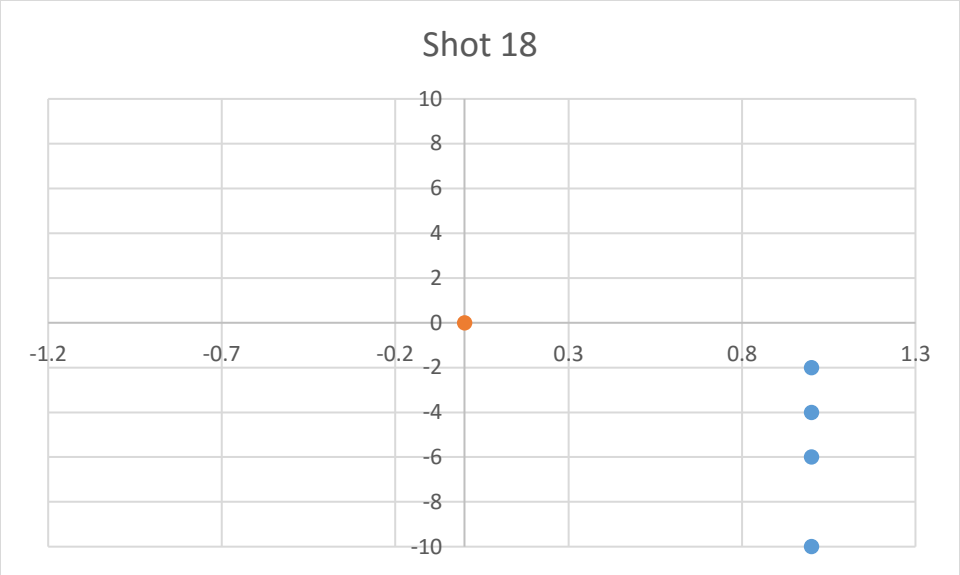

Figure A.17: Shot 18 probe locations

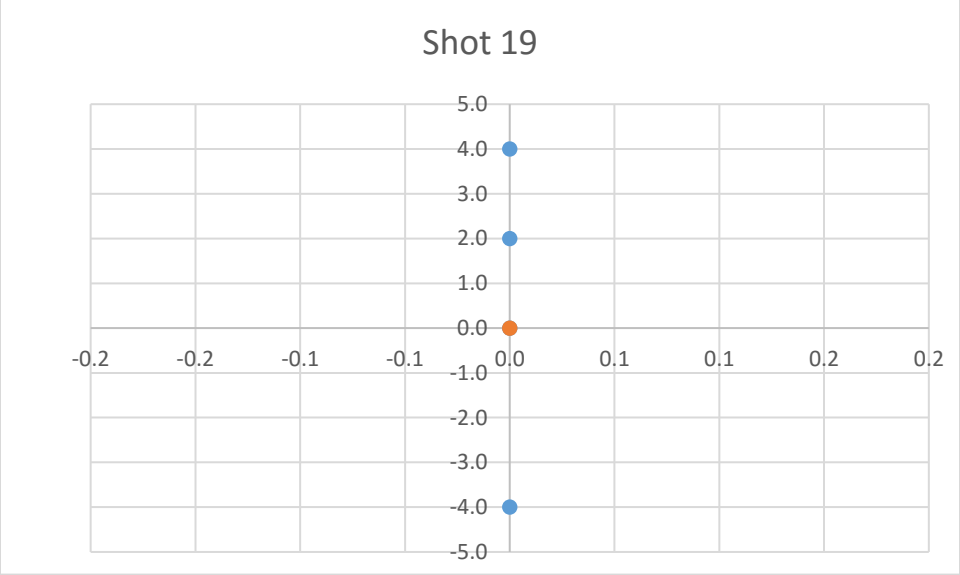

Figure A.18: Shot 19 probe locations

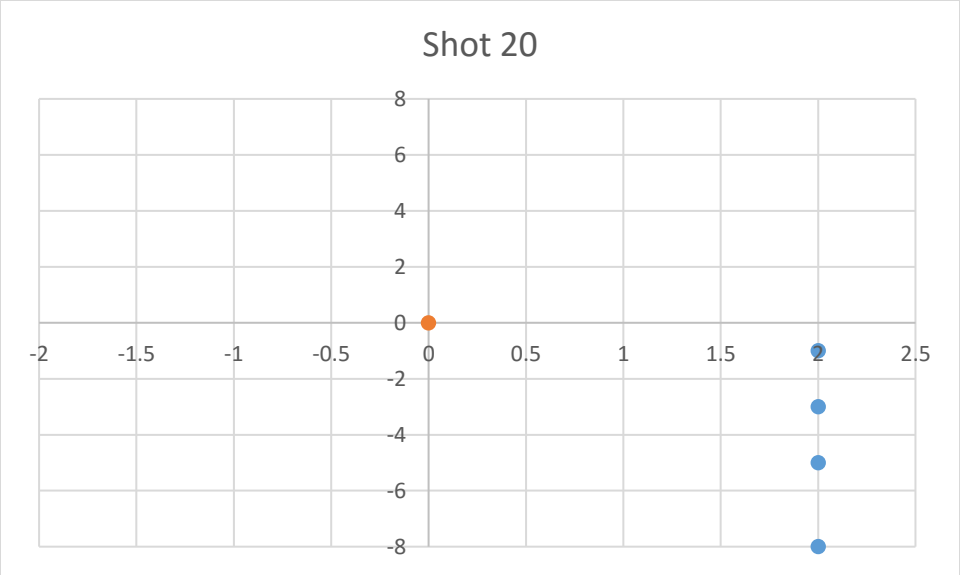

Figure A.19: Shot 20 probe locations

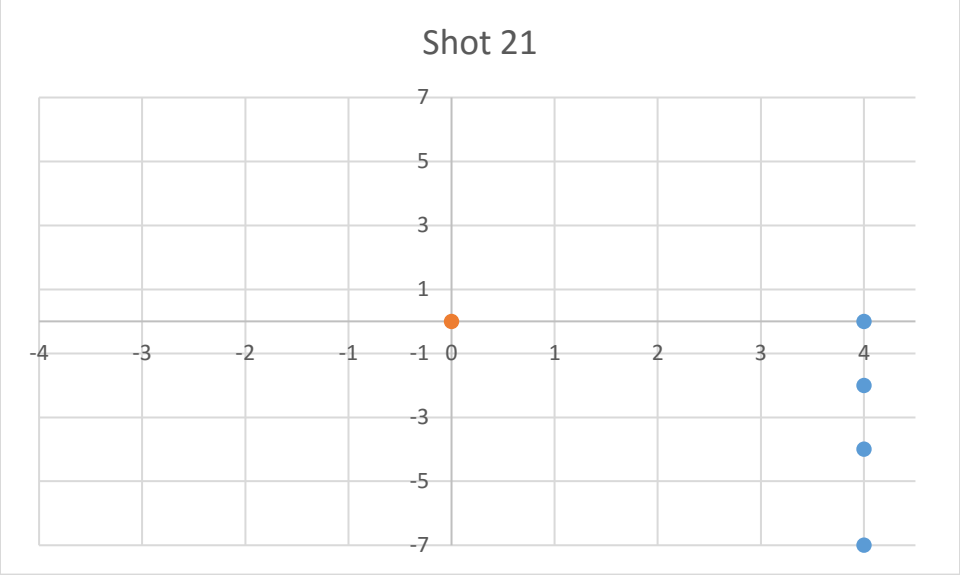

Figure A.20: Shot 21 probe locations

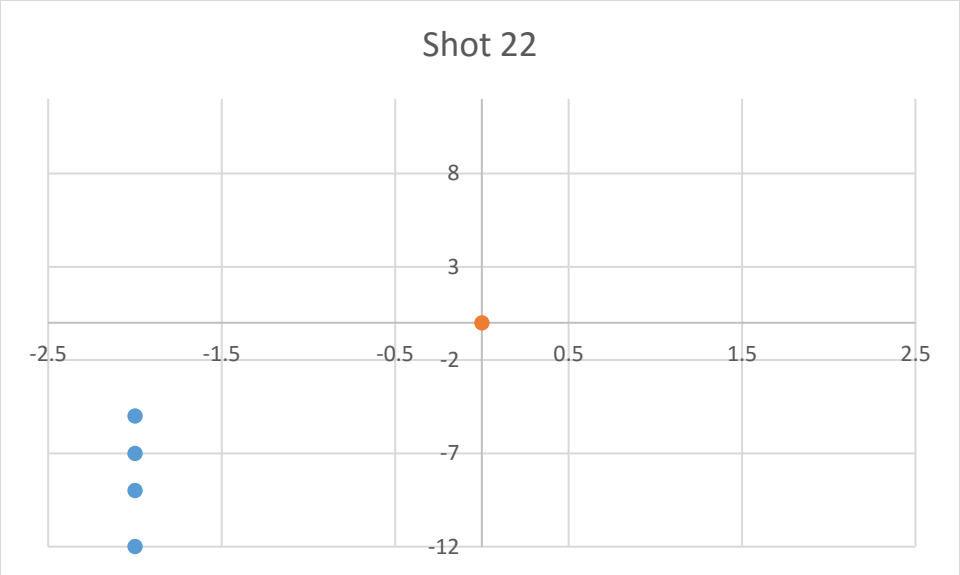

Figure A.21: Shot 22 probe locations

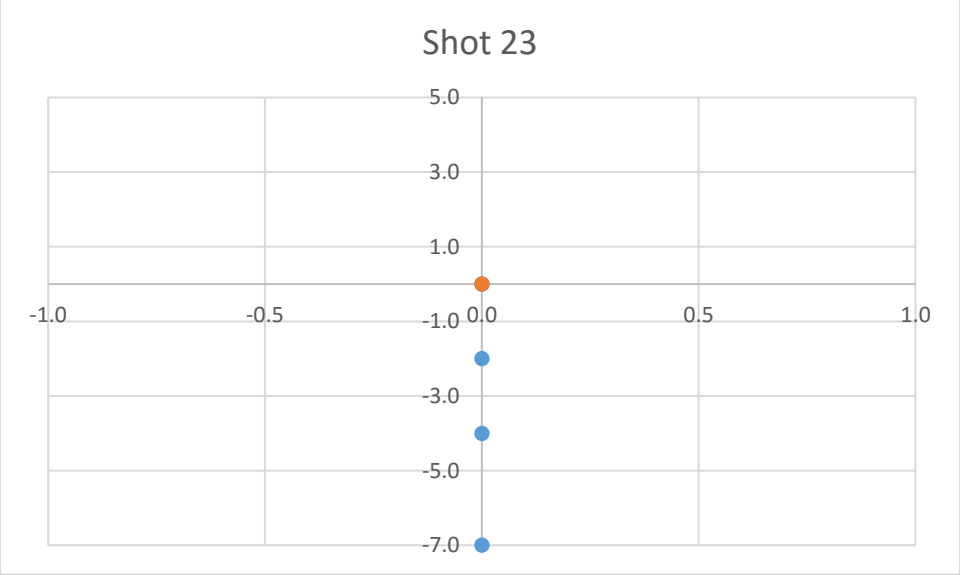

Figure A.22: Shot 23 probe locations

APPENDIX B. ALL VELOCITY TRACES

The following includes velocity traces collected from the PDV diagnostic system.

FORGED TITANIUM- 12.7 MM THICK

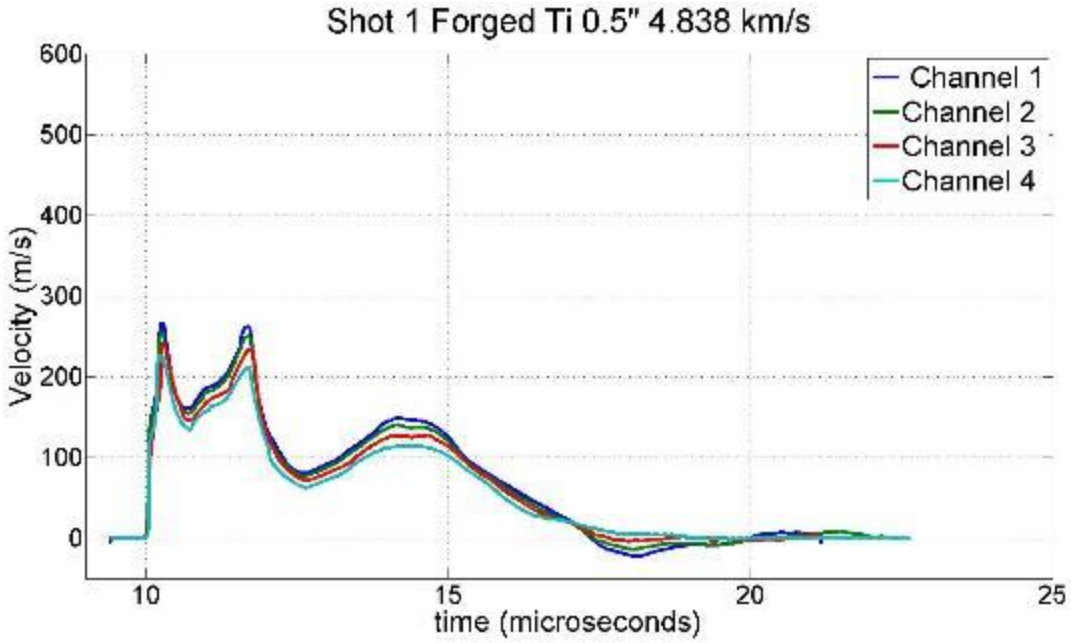

Figure B.1: Shot 1 velocity trace forged titanium 4.8 km/s

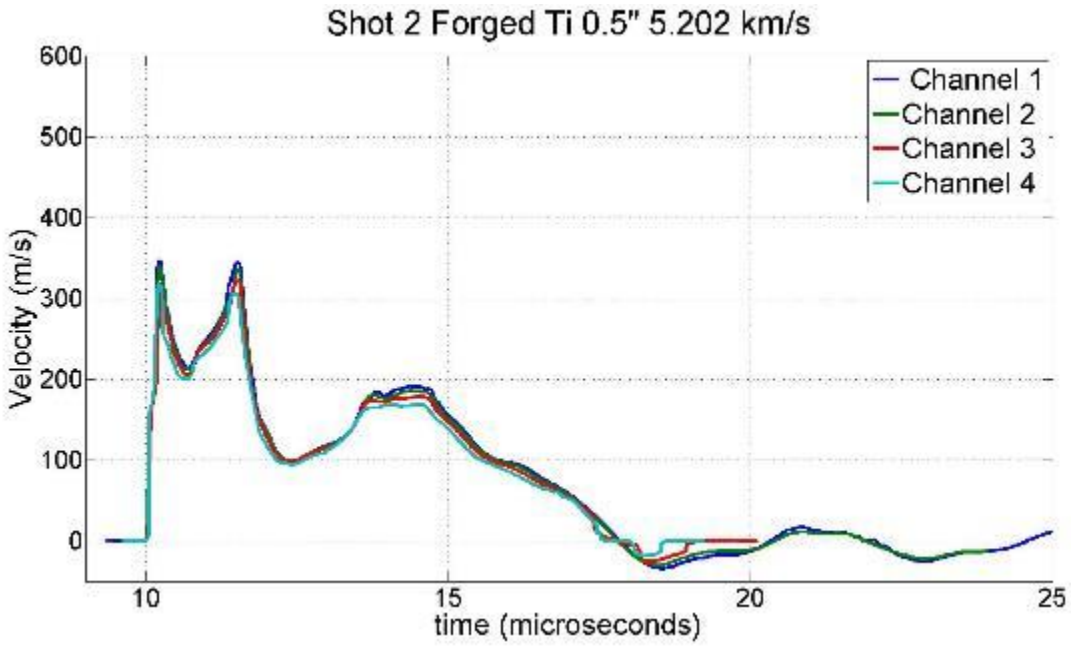

Figure B.2: Shot 2 velocity trace forged titanium 5.2 km/s

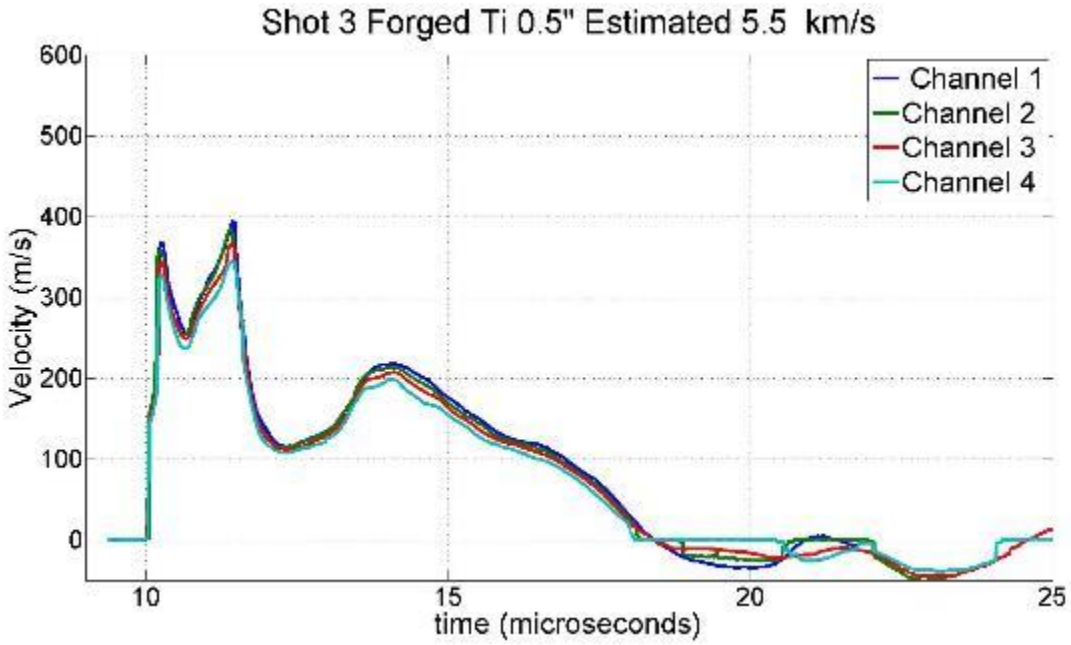

Figure B.3: Shot 3 velocity trace forged titanium 5.5 km/s

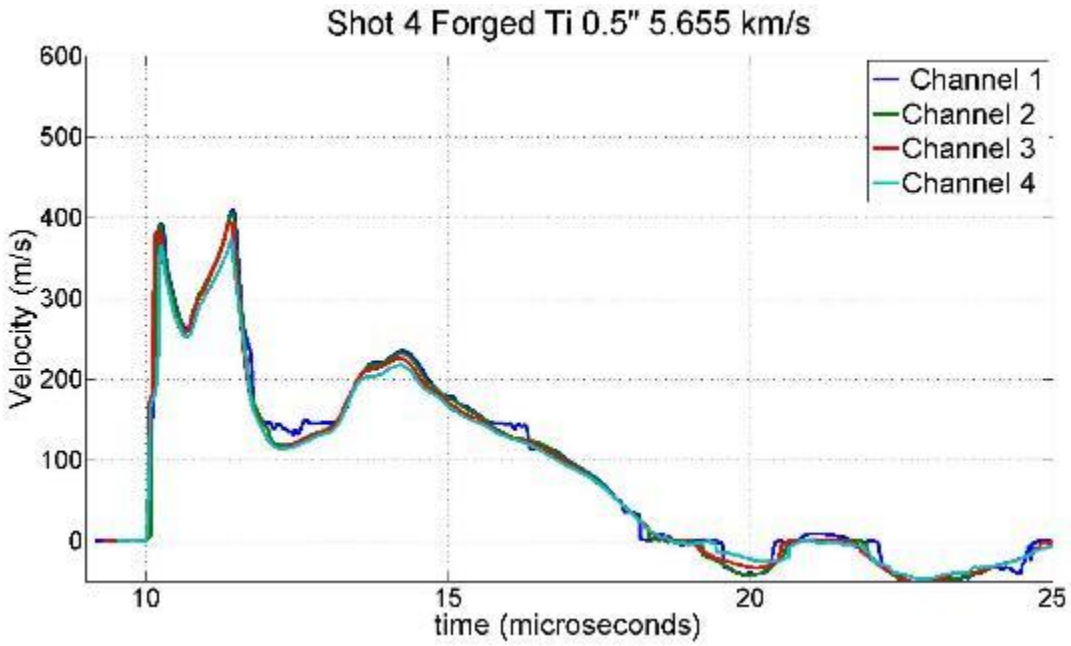

Figure B.4: Shot 4 velocity trace forged titanium 5.7 km/s

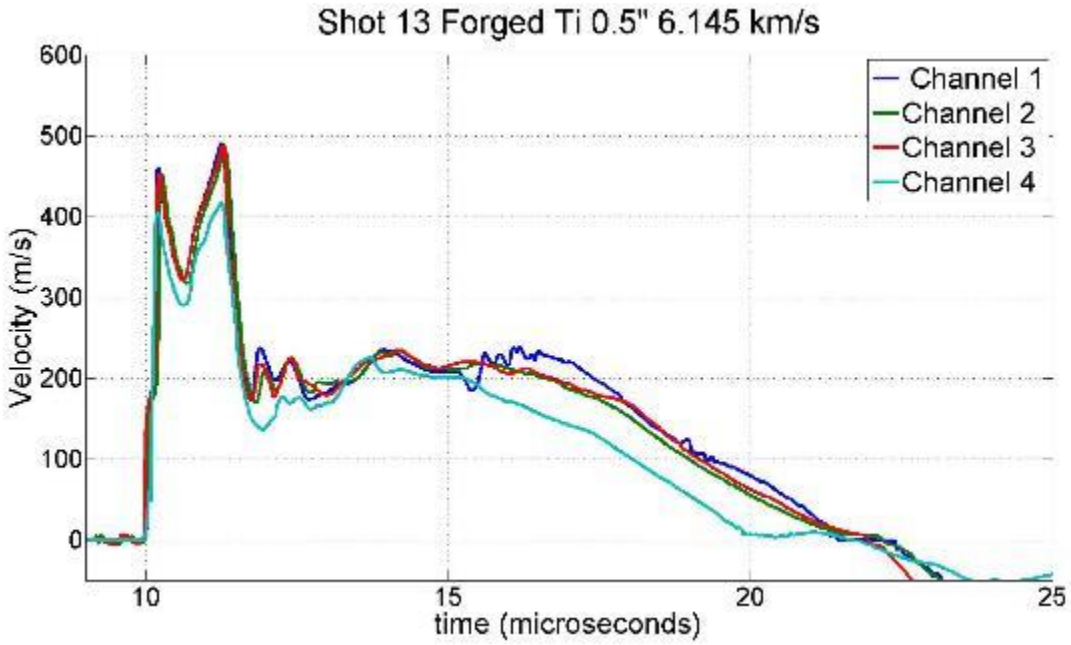

Figure B.5: Shot 13 velocity trace forged titanium 6.1 km/s

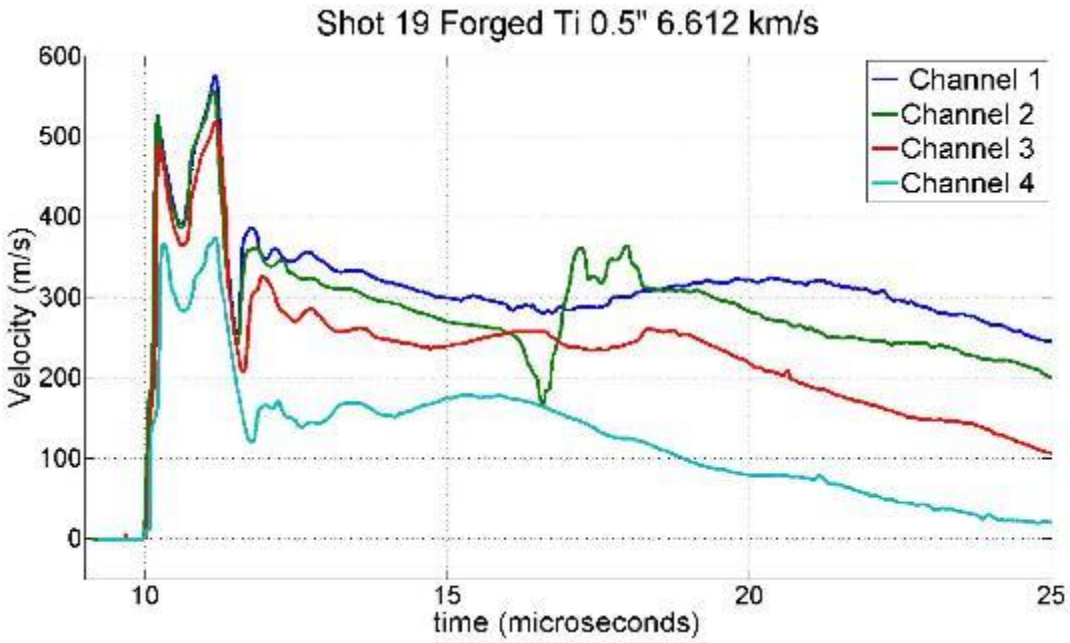

Figure B.6: Shot 19 velocity trace forged titanium 6.6 km/s

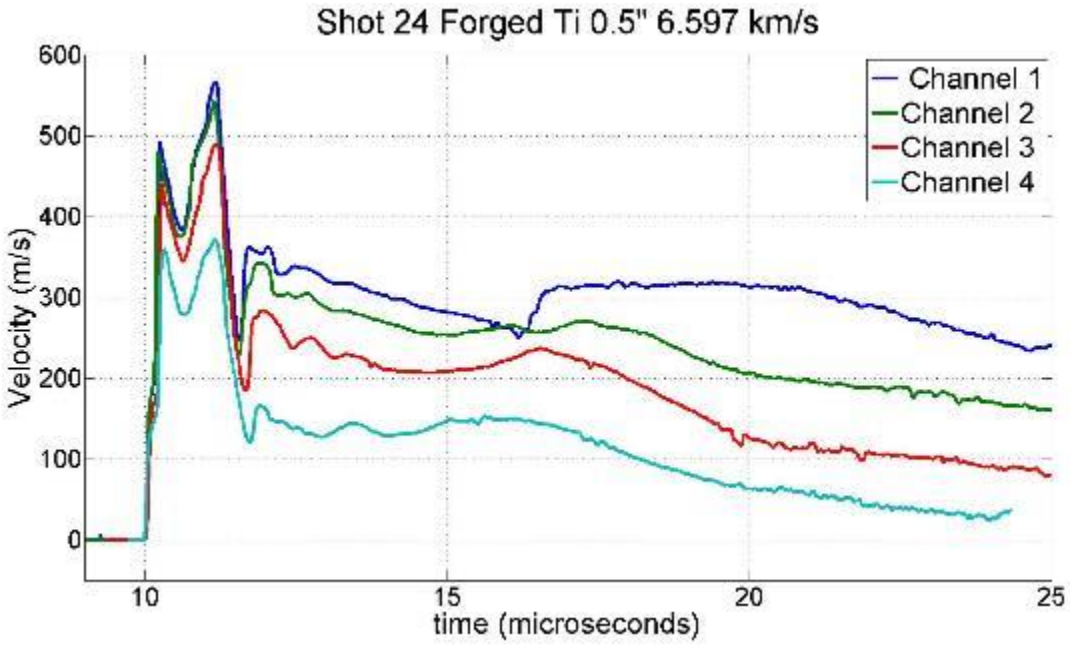

Figure B.7: Shot 24 velocity trace forged titanium 6.6 km/s

FORGED TITANIUM-TWO 6.35 MM STACKED PLATES

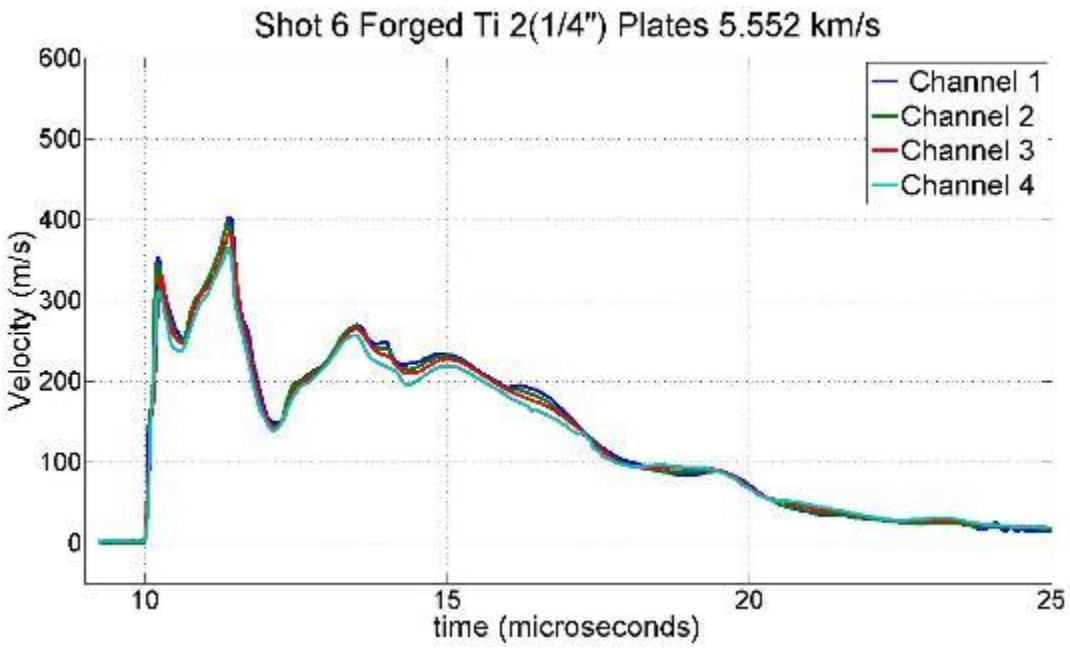

Figure B.8: Shot 6 velocity trace 2-layer 5.6 km/s

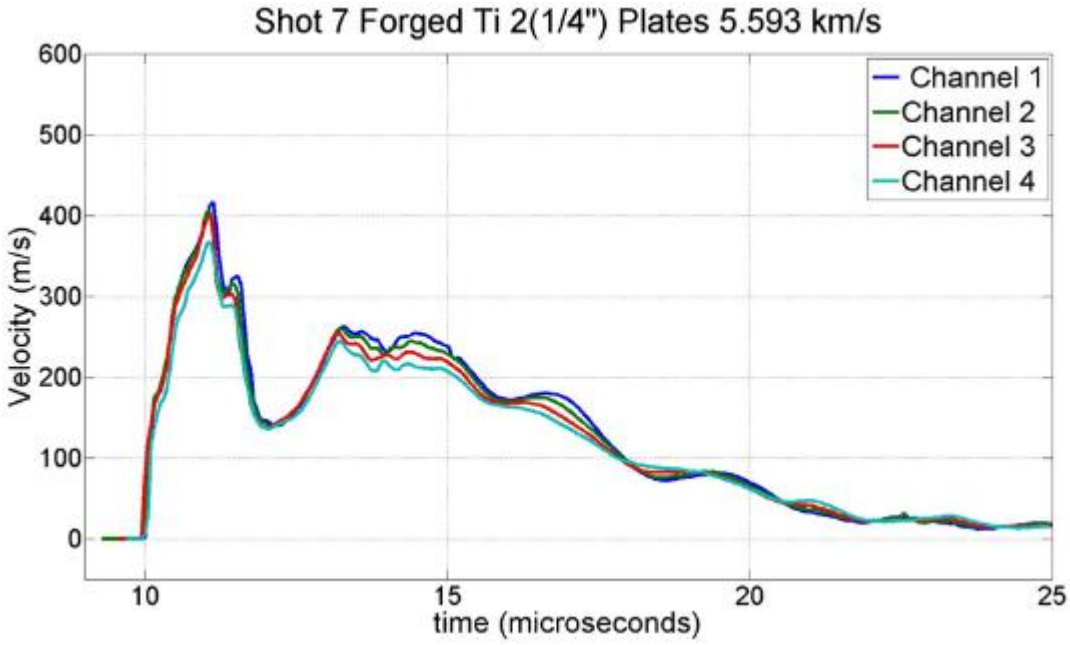

Figure B.9: Shot 7 velocity trace 2-layer 5.6 km/s

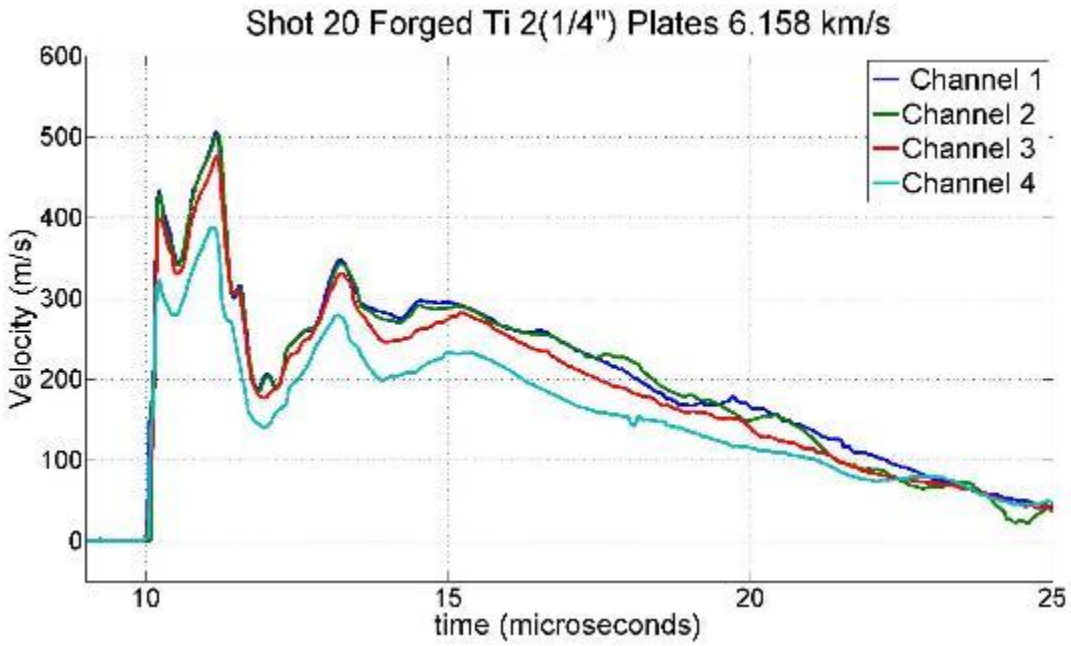

Figure B.10: Shot 20 velocity trace 2-layer 6.2 km/s

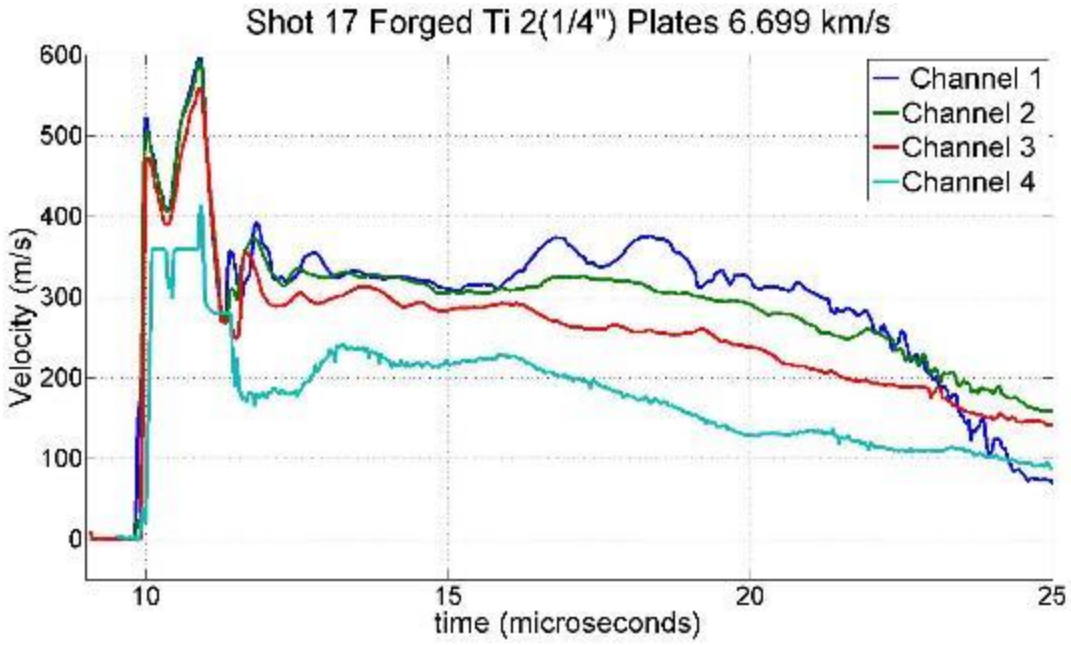

Figure B.11: Shot 17 velocity trace 2-layer 6.7 km/s

FORGED TITANIUM-4 3.2 MM STACKED PLATES

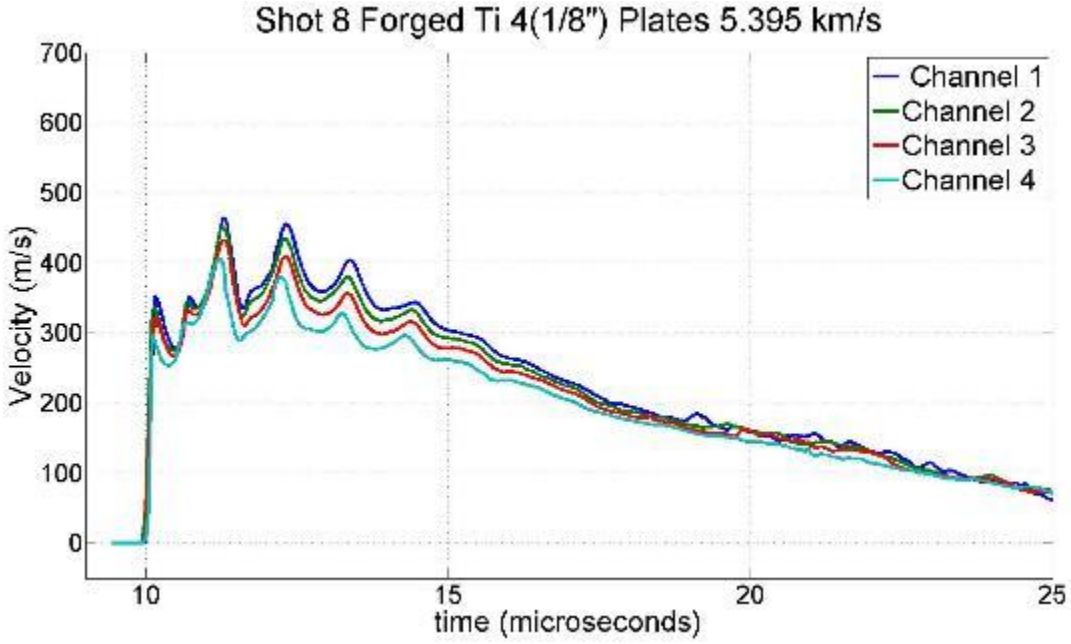

Figure B.12: Shot 8 velocity trace 4-layer 5.4 km/s

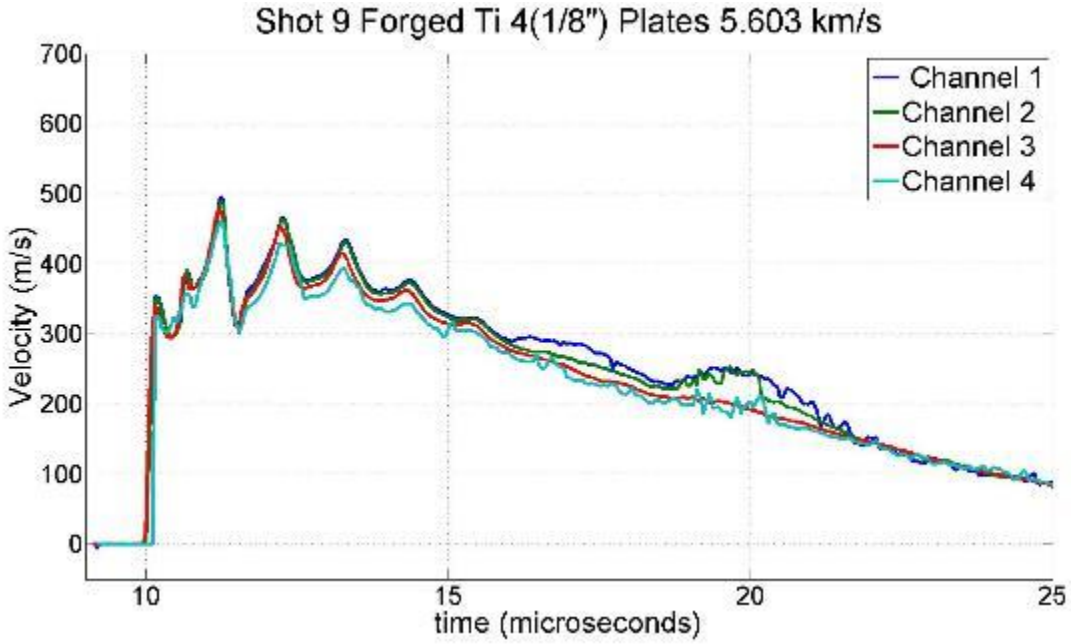

Figure B.13: Shot 9 velocity trace 4-layer 5.6 km/s

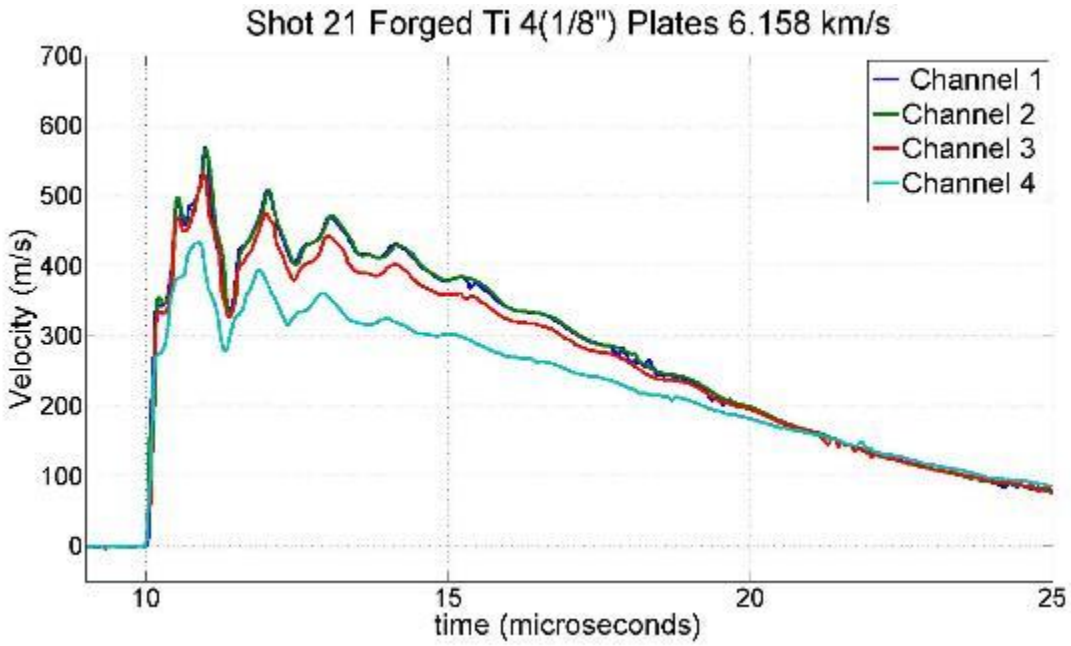

Figure B.14: Shot 21 velocity trace 4-layer 6.2 km/s

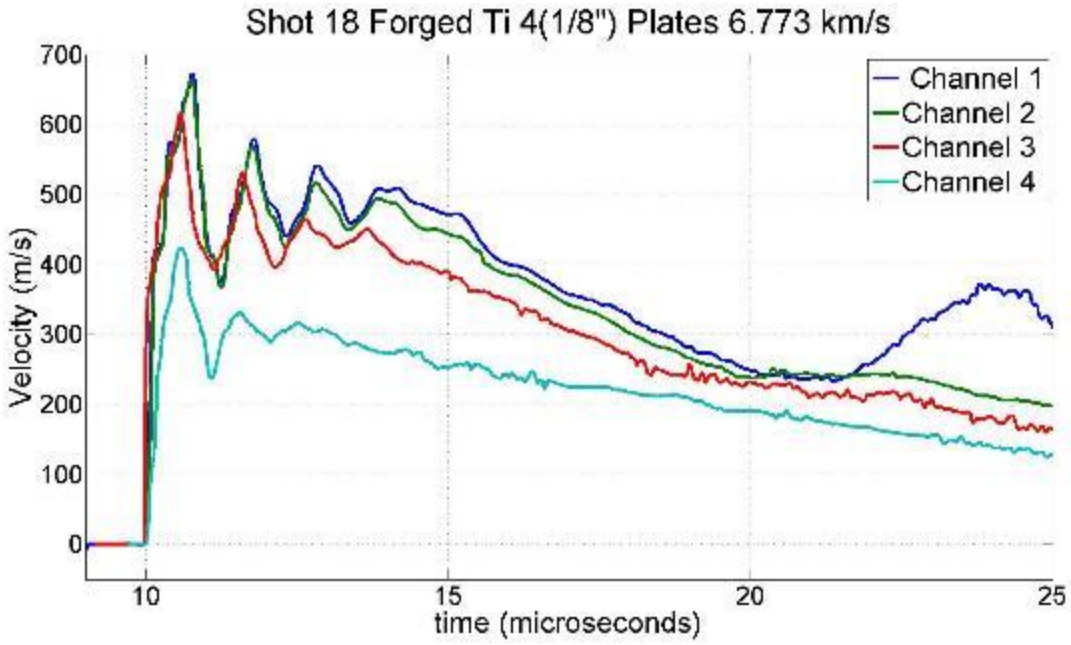

Figure B.15: Shot 18 velocity trace 4-layer 6.8 km/s

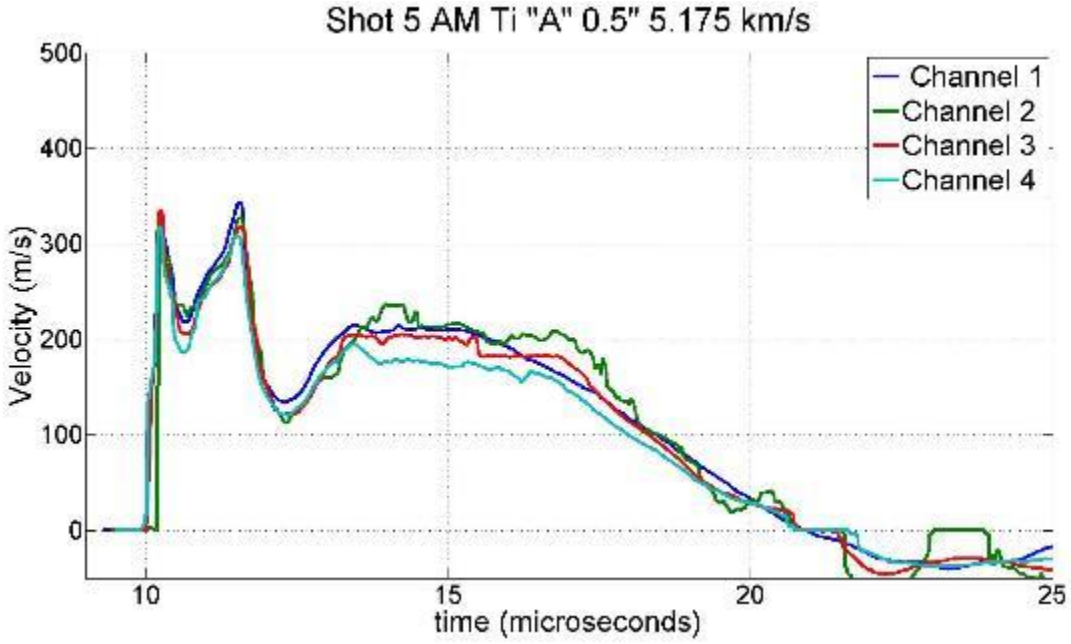

Figure B.16: Shot 5 velocity trace AM 'A' 5.2 km/s

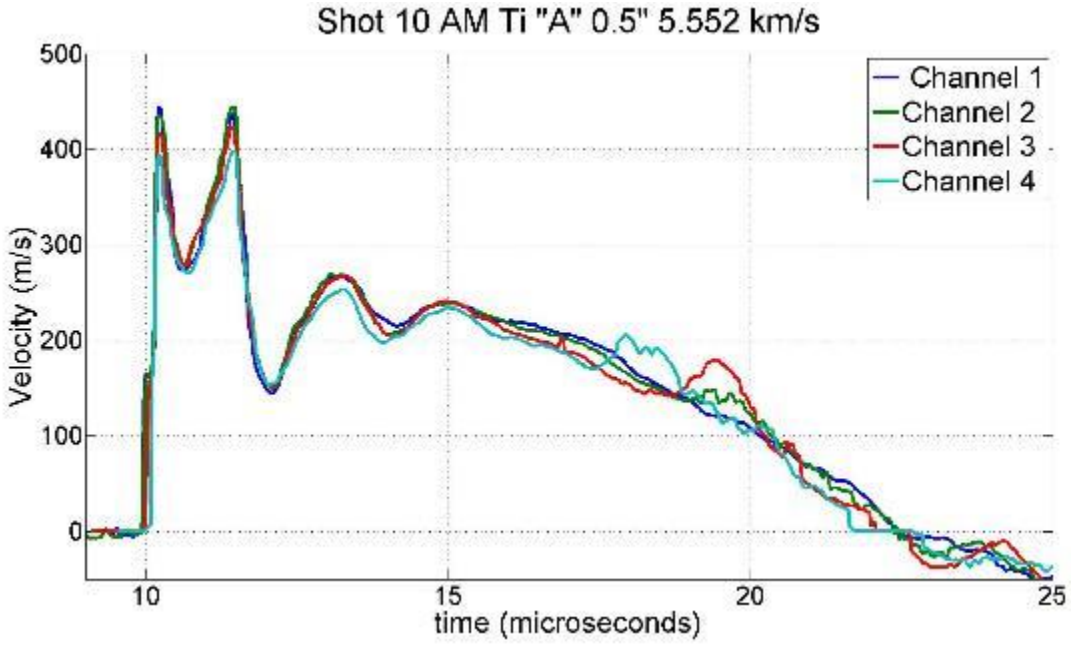

Figure B.17: Shot 10 velocity trace AM 'A' 5.5 km/s

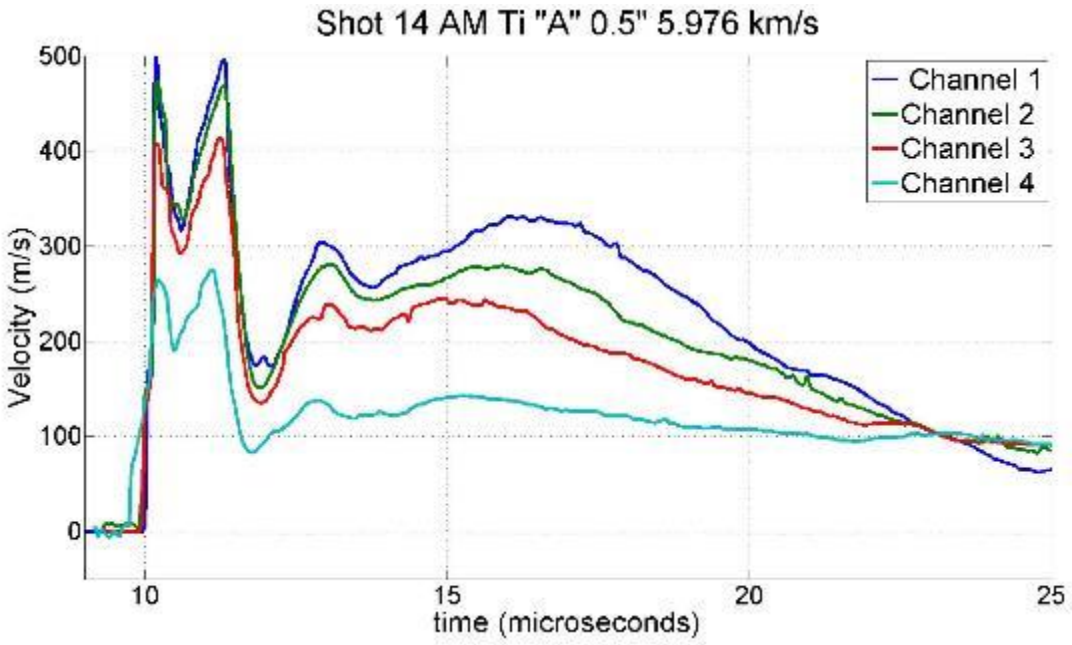

Figure B.18: Shot 14 velocity trace AM 'A' 6.0 km/s

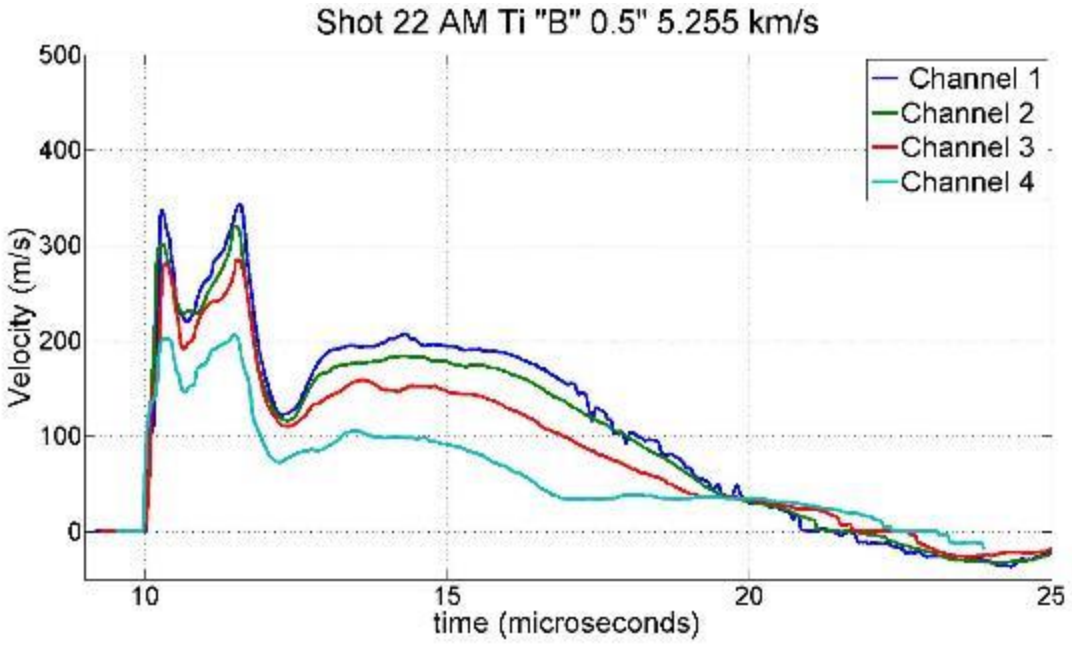

Figure B.19: Shot 2 velocity trace AM 'B' 5.3 km/s

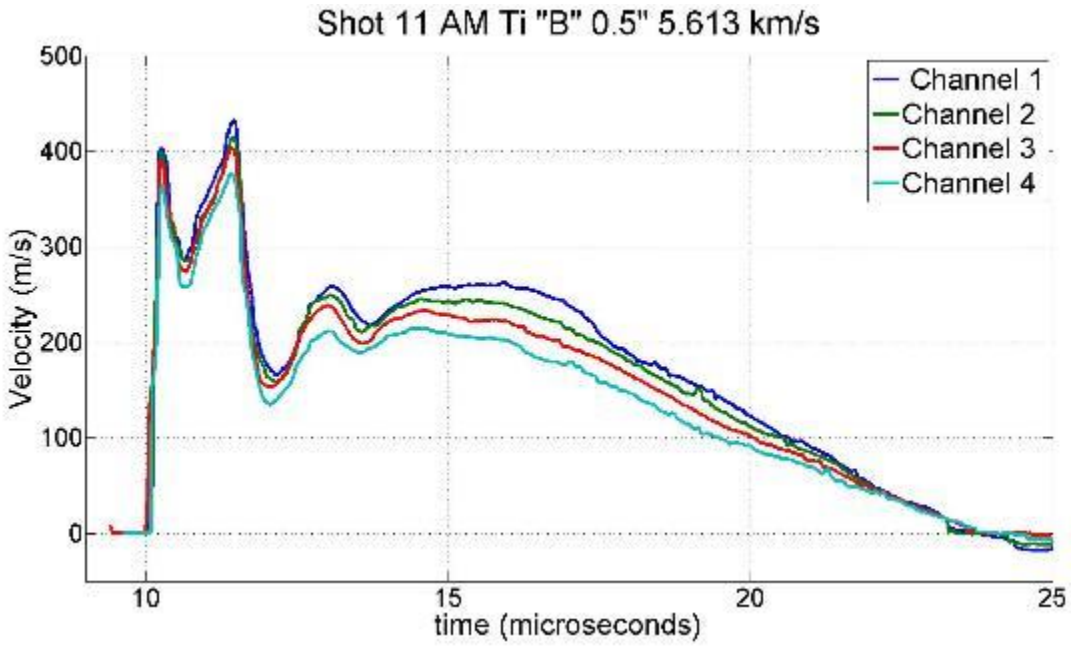

Figure B.20: Shot 11 velocity trace AM 'B' 5.6 km/s

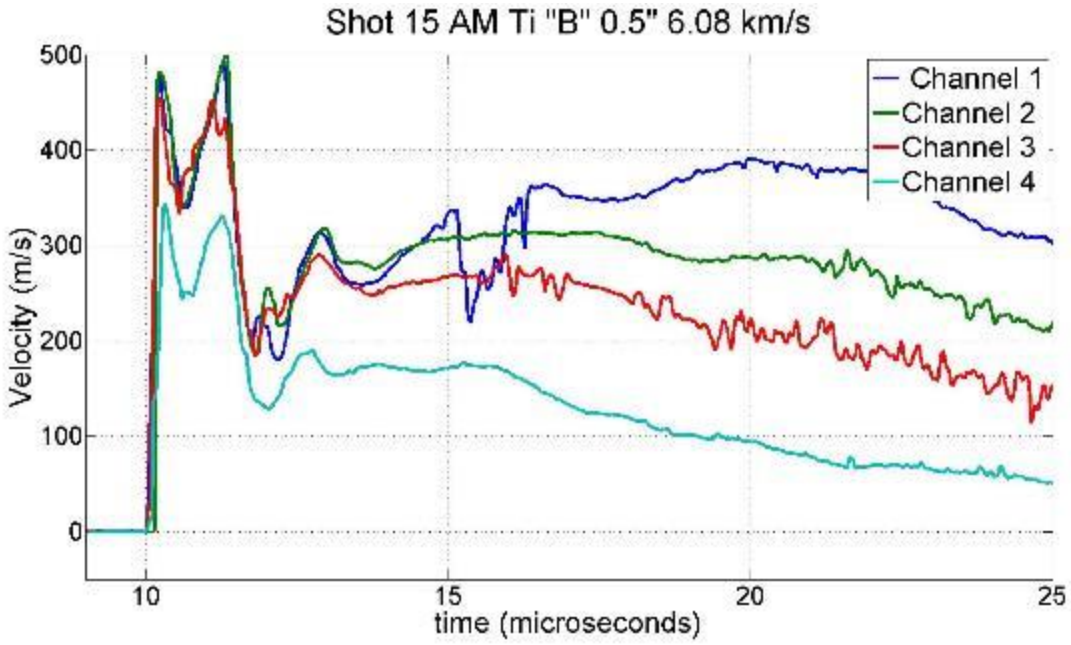

Figure B.21: Shot 15 velocity trace AM 'B' 6.1 km/s

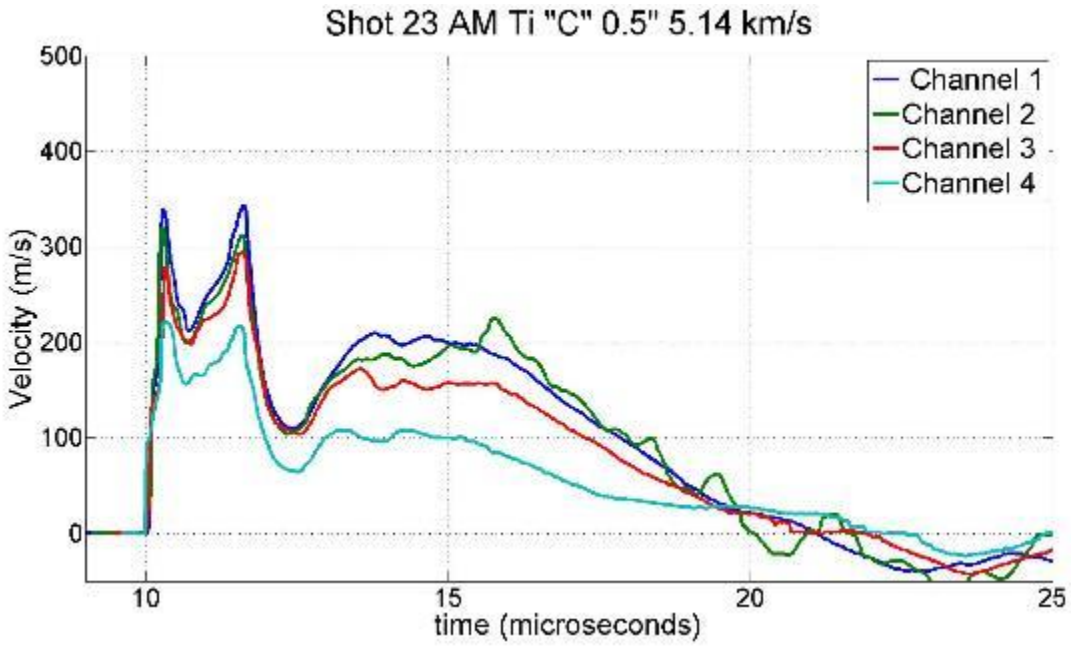

Figure B.22: Shot 23 velocity trace AM 'C' 5.1 km/s

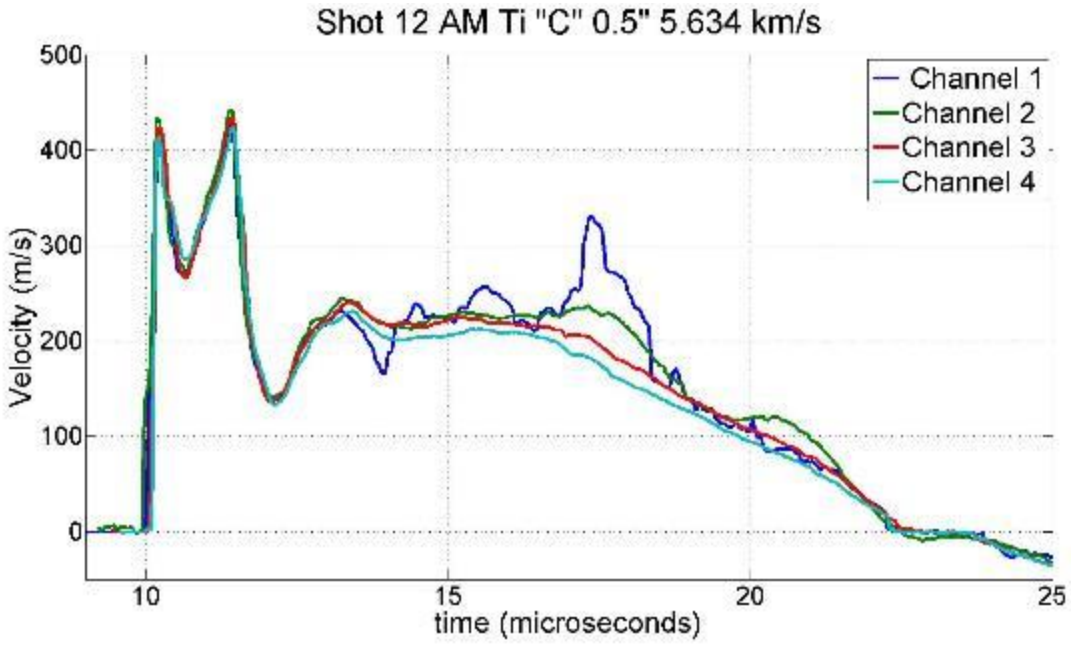

Figure B.23: Shot 12 velocity trace AM 'C' 5.6 km/s

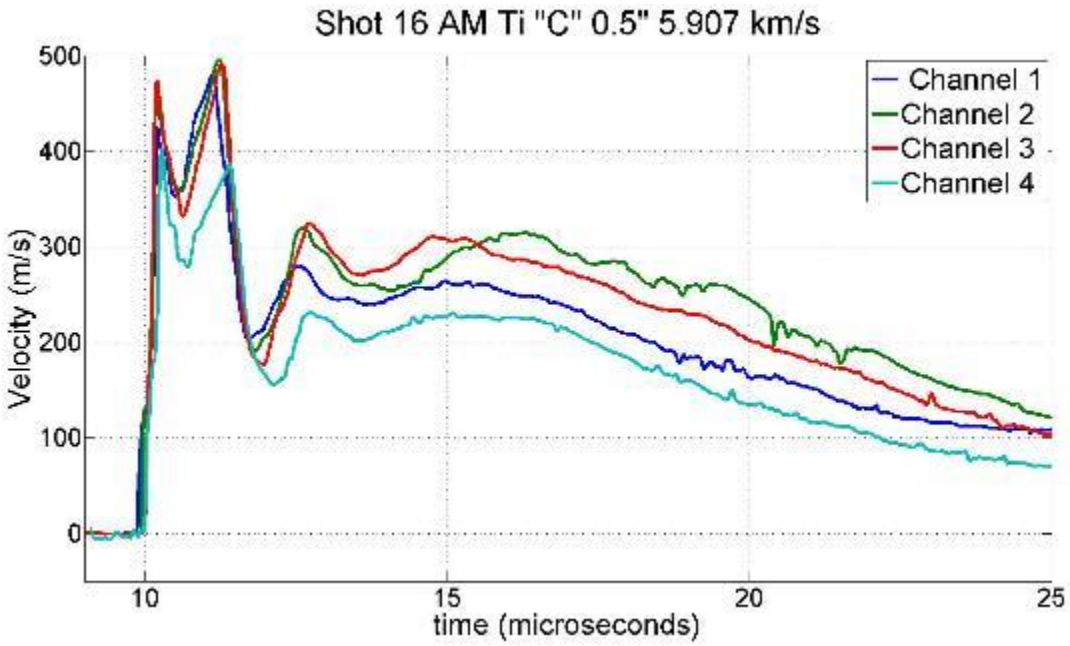

Figure B.24: Shot 16 velocity trace AM 'C' 5.9 km/s

APPENDIX C. PARTICLE SPACING STUDY

In all FEA software, there is a convergence based upon the amount of elements or nodes. This convergence is when there is a less than 5% difference in the simulation data when the number elements or nodes changes. In this case, a study was conducted on the particle spacing, which corresponds to the amount of nodes in a model. Every model was a 12.7 mm (0.5") thick forged titanium 2-D axis-symmetric model impacted by a Lexan^{TM} projectile at.6.1 km/s. The spacing started with 1 mm until 0.1 mm spacing (Figure C.1). Then a final study was conducted at 0.05 mm spacing showing that it converged at 0.1 mm spacing (Figure C.2).

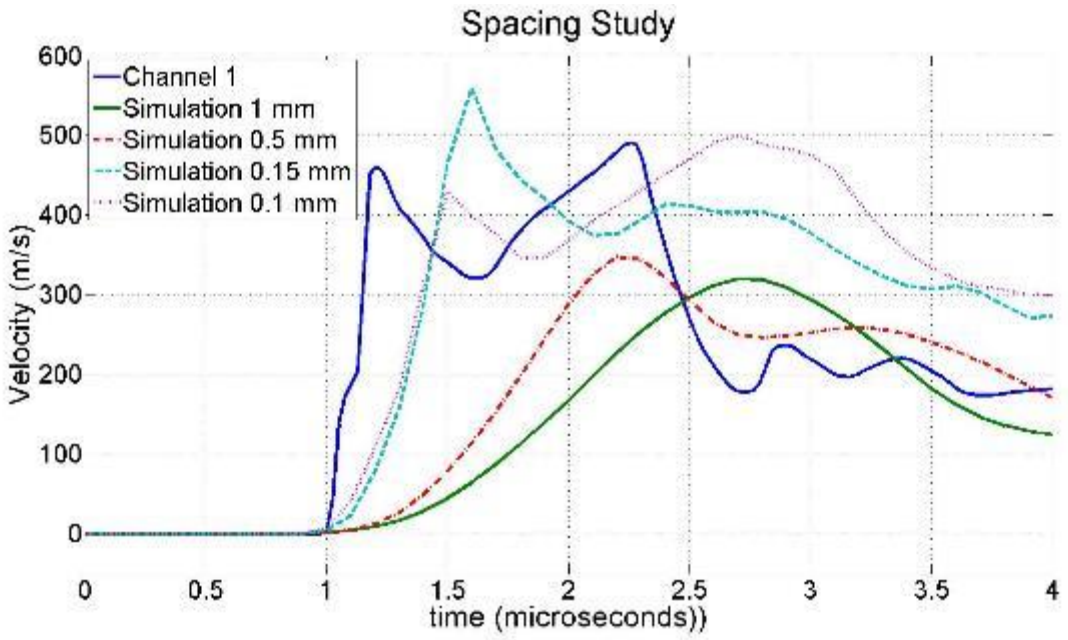

Figure C.1: Spacing study until 0.1 mm spacing

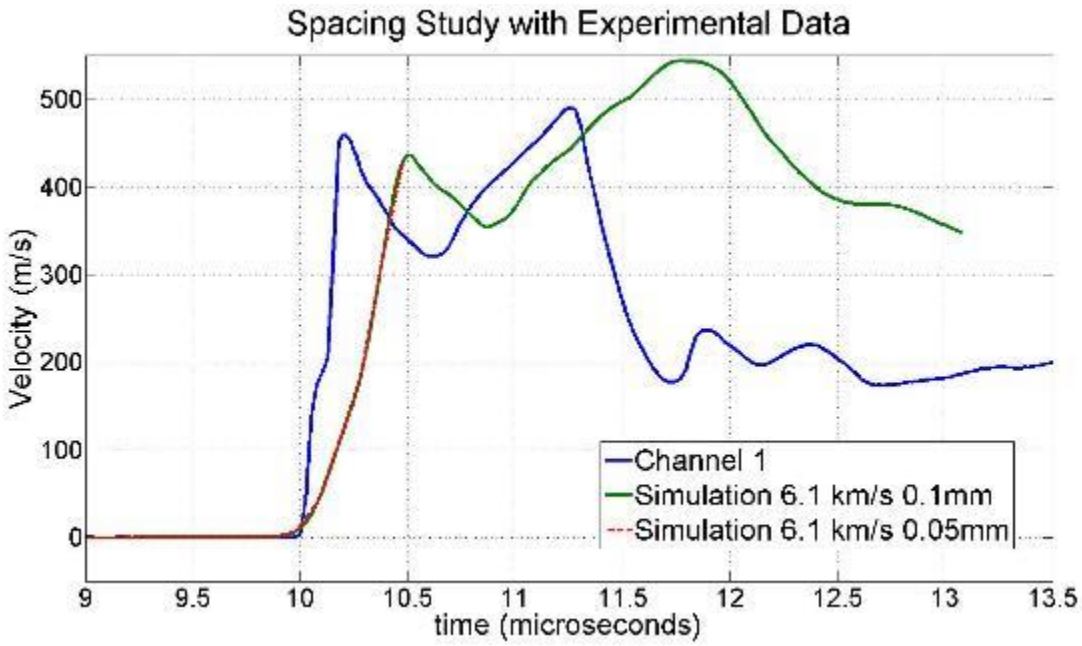

Figure C.2: Spacing study converges to 0.1 mm spacing

APPENDIX D. SAMPLE LS-DYNA® CODE

The following will be examples of the LS-DYNA® code used for the simulations

```
*SECTION_SPH
$HMNAME PROPS       3sph
$#    secid      cslh      hmin      hmax    sphini     death     start
         3  1.050000  0.200000  2.000000     0.0001.0000E+20     0.000
*MAT_JOHNSON_COOK
$HMNAME MATS       1Ti4Al6V
$#     mid        ro         g         e        pr       dtf        vp    rateop
         1 4428.00004.4000E+101.1380E+11  0.342000     0.000     0.000     0.000
$#       a         b         n         c         m        tm        tr      epso
 1.0980E+9 1.0920E+9  0.930000 1.4000E-2  1.100000 1933.0000 298.00000  1.000000
$#      cp        pc     spall        it        d1        d2        d3        d4
 526.29999 -9.500E+8  1.000000     0.000 -9.000E-2  0.270000  0.480000 1.4000E-2
$#      d5      c2/p      erod     efmin
  3.870000     0.000         0 1.0000E-6
*EOS_GRUNEISEN
$HMNAME PROPS       1eos_A36
$#   eosid         c        s1        s2        s3     gamao         a        e0
         1 4459.0000  1.250000     0.000     0.000  1.028000     0.000     0.000
$#      v0
  1.000000
*MAT_JOHNSON_COOK
$HMNAME MATS       2Lexan
$#     mid        ro         g         e        pr       dtf        vp    rateop
         2 1190.0000 7.8600E+8 2.5400E+9  0.340000     0.000     0.000     0.000
$#       a         b         n         c         m        tm        tr      epso
 7.5400E+7 6.8900E+7  1.004000     0.000  1.850000 533.00000 298.00000  1.000000
$#      cp        pc     spall        it        d1        d2        d3        d4
 1186.0000 -1.600E+8  3.000000     0.000     0.000     0.000     0.000     0.000
$#      d5      c2/p      erod     efmin
     0.000     0.000         0 1.0000E-6
*EOS_GRUNEISEN
$HMNAME PROPS       2eos_Lexan
$#   eosid         c        s1        s2        s3     gamao         a        e0
         2 1933.0000  1.420000     0.000     0.000  0.610000     0.000     0.000
$#      v0
  1.000000
*INITIAL_VELOCITY
$#    nsid     nsidex     boxid    irigid      icid
    200481          0         0         0         0
$#      vx        vy        vz       vxr       vyr       vzr
     0.000-5202.0000     0.000     0.000     0.000     0.000
*SET_NODE_LIST_GENERATE
$---+----1----+----2----+----3----+----4----+----5----+----6----+----7----+----8
$       SID       DA1       DA2       DA3       DA4
$#      sid       da1       da2       da3       da4    solver
    200481     0.000     0.000     0.000     0.000MECH
$     B1BEG     B1END     B2BEG     B2END
$#   b1beg     b1end     b2beg     b2end     b3beg     b3end     b4beg     b4end
    200001    200480         0         0         0         0         0         0
*DAMPING_GLOBAL
$$     LCID    VALDMP       STX       STR       STZ       SRX       SRY       SRZ
$#     lcid    valdmp       stx       sty       stz       srx       sry       srz
         0     0.000     0.000     0.000     0.000     0.000     0.000     0.000
```

Figure D.1: Sample forged titanium alloy simulation code

```
        0         0
*SECTION_SPH
$HMNAME PROPS       3sph
$#   secid      cslh      hmin      hmax    sphini     death     start
         3  1.050000  0.200000  2.000000     0.0001.0000E+20     0.000
*MAT_JOHNSON_COOK
$HMNAME MATS       1Ti4Al6V
$#     mid        ro         g         e        pr       dtf        vp    rateop
         1 4177.00004.1800E+101.0811E+11  0.342000     0.000     0.000     0.000
$#       a         b         n         c         m        tm        tr      epso
 1.0980E+9 1.0920E+9  0.930000 1.4000E-2  1.100000 1933.0000 298.00000  1.000000
$#      cp        pc     spall        it        d1        d2        d3        d4
 526.29999 -9.025E+8  1.000000     0.000 -9.000E-2  0.270000  0.480000 1.4000E-2
$#      d5      c2/p      erod     efmin
  3.870000     0.000         0 1.0000E-6
*EOS_GRUNEISEN
$HMNAME PROPS       1eos_A36
$#   eosid         c        s1        s2        s3     gamao         a        e0
         1 4459.0000  1.250000     0.000     0.000  1.028000     0.000     0.000
$#      v0
  1.000000
*MAT_JOHNSON_COOK
$HMNAME MATS       2Lexan
$#     mid        ro         g         e        pr       dtf        vp    rateop
         2 1190.0000 7.8600E+8 2.5400E+9  0.340000     0.000     0.000     0.000
$#       a         b         n         c         m        tm        tr      epso
 7.5400E+7 6.8900E+7  1.004000     0.000  1.850000 533.00000 298.00000  1.000000
$#      cp        pc     spall        it        d1        d2        d3        d4
 1186.0000 -1.600E+8  3.000000     0.000     0.000     0.000     0.000     0.000
$#      d5      c2/p      erod     efmin
    0.000     0.000         0 1.0000E-6
*EOS_GRUNEISEN
$HMNAME PROPS       2eos_Lexan
$#   eosid         c        s1        s2        s3     gamao         a        e0
         2 1933.0000  1.420000     0.000     0.000  0.610000     0.000     0.000
$#      v0
  1.000000
*INITIAL_VELOCITY
$#    nsid    nsidex     boxid    irigid      icid
    200481         0         0         0         0
$#      vx        vy        vz       vxr       vyr       vzr
    0.000-5140.0000     0.000     0.000     0.000     0.000
*SET_NODE_LIST_GENERATE
$---+----1----+----2----+----3----+----4----+----5----+----6----+----7----+----8
$       SID       DA1       DA2       DA3       DA4
$#      sid       da1       da2       da3       da4    solver
    200481     0.000     0.000     0.000     0.000MECH
$     B1BEG     B1END     B2BEG     B2END
$#   b1beg     b1end     b2beg     b2end     b3beg     b3end     b4beg     b4end
    200001    200480         0         0         0         0         0         0
*DAMPING_GLOBAL
$$     LCID    VALDMP       STX       STR       STZ       SRX       SRY       SRZ
$#     lcid    valdmp       stx       sty       stz       srx       sry       srz
         0     0.000     0.000     0.000     0.000     0.000     0.000     0.000
*PART
```

Figure D.2: Sample AM titanium simulation code

```
$# title
SphNode
$#     pid     secid       mid     eosid      hgid      grav    adpopt      tmid
         3         3         2         2         0         0         0         0
*MAT_JOHNSON_COOK
$HMNAME MATS       2Lexan
$#     mid        ro         g         e        pr       dtf        vp    rateop
         2 1190.0000 7.8600E+8 2.5400E+9  0.340000     0.000     0.000     0.000
$#       a         b         n         c         m        tm        tr      epso
 7.5400E+7 6.8900E+7  1.004000     0.000  1.850000 533.00000 298.00000  1.000000
$#      cp        pc     spall        it        d1        d2        d3        d4
 1186.0000 -1.600E+8  3.000000     0.000     0.000     0.000     0.000     0.000
$#      d5      c2/p      erod     efmin
     0.000     0.000         0 1.0000E-6
*EOS_GRUNEISEN
$HMNAME PROPS       2eos_Lexan
$#   eosid         c        s1        s2        s3     gamao         a        e0
         2 1933.0000  1.420000     0.000     0.000  0.610000     0.000     0.000
$#      v0
  1.000000
*INITIAL_VELOCITY
$#    nsid    nsidex     boxid    irigid      icid
    400161         0         0         0         0
$#      vx        vy        vz       vxr       vyr       vzr
     0.000-5520.0000     0.000     0.000     0.000     0.000
*DEFINE_BOX
$#   boxid       xmn       xmx       ymn       ymx       zmn       zmx
         1 1.7370E-4 2.6063E-3 1.3215E-2 2.1385E-2     0.000  1.000000
*DEFINE_BOX
$#   boxid       xmn       xmx       ymn       ymx       zmn       zmx
         2 1.0000E-4  0.101501 6.4492E-3 1.2601E-2     0.000  1.000000
*DEFINE_BOX
$#   boxid       xmn       xmx       ymn       ymx       zmn       zmx
         3 1.0000E-4  0.101501 9.9219E-5 6.2508E-3     0.000  1.000000
*DEFINE_SPH_TO_SPH_COUPLING_ID
$#     did
         1
$---+----1----+----2----+----3----+----4----+----5----+----6----+----7----+----8
$#    ssid      msid     sstyp     mstyp     ibox1     ibox2     pfact
         2         3         1         1         2         1    1.0e-4
*DEFINE_SPH_TO_SPH_COUPLING_ID
$---+----1----+----2----+----3----+----4----+----5----+----6----+----7----+----8
         2
         1         2         1         2         1         3    1.0e-4
*SET_NODE_LIST_GENERATE
$---+----1----+----2----+----3----+----4----+----5----+----6----+----7----+----8
$       SID       DA1       DA2       DA3       DA4
$#      sid       da1       da2       da3       da4    solver
    400161     0.000     0.000     0.000     0.000MECH
$     B1BEG     B1END     B2BEG     B2END
$#   b1beg     b1end     b2beg     b2end     b3beg     b3end     b4beg     b4end
    400001    400160         0         0         0         0         0         0
*DAMPING_GLOBAL
$$     LCID    VALDMP       STX       STR       STZ       SRX       SRY       SRZ
$#     lcid    valdmp       stx       sty       stz       srx       sry       srz
         0     0.000     0.000     0.000     0.000     0.000     0.000     0.000
*ELEMENT_SPH
```

Figure D.3: Sample 2-layer simulation code

```
SphNode
$#     pid     secid       mid     eosid      hgid      grav    adpopt      tmid
         5         3         2         2         0         0         0         0
*MAT_JOHNSON_COOK
$HMNAME MATS       2Lexan
$#     mid        ro         g         e        pr       dtf        vp    rateop
         2 1190.0000 7.8600E+8 2.5400E+9  0.340000     0.000     0.000     0.000
$#       a         b         n         c         m        tm        tr      epso
 7.5400E+7 6.8900E+7  1.004000     0.000  1.850000 533.00000 298.00000  1.000000
$#      cp        pc     spall        it        d1        d2        d3        d4
 1186.0000 -1.600E+8  3.000000     0.000     0.000     0.000     0.000     0.000
$#      d5      c2/p      erod     efmin
    0.000     0.000         0 1.0000E-6
*EOS_GRUNEISEN
$HMNAME PROPS       2eos_Lexan
$#   eosid         c        s1        s2        s3     gamao         a        e0
         2 1933.0000  1.420000     0.000     0.000  0.610000     0.000     0.000
$#      v0
  1.000000
*INITIAL_VELOCITY
$#    nsid    nsidex     boxid    irigid      icid
   1000640         0         0         0         0
$#      vx        vy        vz       vxr       vyr       vzr
    0.000-5603.0000     0.000     0.000     0.000     0.000
*DEFINE_BOX
$#   boxid       xmn       xmx       ymn       ymx       zmn       zmx
         1 6.9500E-5 2.7105E-3 1.3134E-2 2.1466E-2     0.000  1.000000
*DEFINE_BOX
$#   boxid       xmn       xmx       ymn       ymx       zmn       zmx
         2 4.9999E-5 7.6151E-2 9.7695E-3 1.2653E-2     0.000  1.000000
*DEFINE_BOX
$#   boxid       xmn       xmx       ymn       ymx       zmn       zmx
         3 4.9999E-5 7.6151E-2 6.5945E-3 9.4785E-3     0.000  1.000000
*DEFINE_BOX
$#   boxid       xmn       xmx       ymn       ymx       zmn       zmx
         4 4.9999E-5 7.6151E-2 3.4195E-3 6.3035E-3     0.000  1.000000
*DEFINE_BOX
$#   boxid       xmn       xmx       ymn       ymx       zmn       zmx
         5 4.9999E-5 7.6151E-2 4.9609E-5 3.1254E-3     0.000  1.000000
*DEFINE_SPH_TO_SPH_COUPLING_ID
$#     cid                                                            name
         1
$---+----1----+----2----+----3----+----4----+----5----+----6----+----7----+----8
$#    ssid      msid     sstyp     mstyp     ibox1     ibox2     pfact      srad
         4         5         1         1         2         1    1.0e-4      0.05
*DEFINE_SPH_TO_SPH_COUPLING_ID
         2
$---+----1----+----2----+----3----+----4----+----5----+----6----+----7----+----8
$#    ssid      msid     sstyp     mstyp     ibox1     ibox2     pfact      srad
         3         4         1         1         3         2    1.0e-4      0.05
*DEFINE_SPH_TO_SPH_COUPLING_ID
         3
$---+----1----+----2----+----3----+----4----+----5----+----6----+----7----+----8
$#    ssid      msid     sstyp     mstyp     ibox1     ibox2     pfact      srad
         2         3         1         1         4         3    1.0e-4      0.05
*DEFINE_SPH_TO_SPH_COUPLING_ID
         4
```

Figure D.4: Sample 4-layer simulation code

REFERENCES

[1] Doolan C. A Two-Stage Light Gas Gun for the Study of High Speed Impact in Propellants. Salisbury: 2001

[2] Chhabildas LC, Knudson MD. Techniques to Launch Projectile Plates to Very High Velocities. In: Chhabildas LC, Davidson L, Horie Y, editors. High-Pressure Shock Compression Solids VIII, Springer-Verlag Berlin Heidelberg; 2005, p. 143–99. doi:10.1007/3-540-27168-6_4.

[3] Holmes N. "Shocking" Gas-Gun Experiments. S TR 2000:13–9.

[4] Swift HF. Light-Gas Gun Technology : A Historical Perspective. In: Chhabildas LC, Davison L, Horie Y, editors. High-Pressure Shock Compression Solids VIII, SpringerVerlag Berlin Heidelberg; 2005, p. 1–35

[5] Rosenberg Z, Dekel E. Terminal Ballistics. Springer; 2012.

[6] Oscarson JH, Graff KF. Spall fracture and dynamic response of materials. Columbus, OH: 1968

[7] S. Roy, D. Sankar, R. Jennings, S. Becker, E. Daykin, R. Hixson, J. Thota, M. Trabia, B.O'Toole, M. Matthes, "Computational and Experimental Study of Plastic Deformation in A36 Steel during High Velocity Impact", (Abstract) ASME Verification & Validation Symposium 2013-2426, May 22-24, 2013, Las Vegas NV.

[8] S. Roy, B. O'Toole, M. Trabia, J. Thota, R. Jennings, D. Somasundarum, M. Matthes, S. Becker, R. Hixson, E. Daykin, E. Machorro, M. Pena, T. Meehan, N. Sipe, & K. Crawford, "Measurement and Simulation of Plastic Deformation of Steel Plates during High Velocity Impact", To appear in Proceedings of International Symposium on Plasticity, Freeport, Bahamas, January 3-8, 2014.

[9] B. O'Toole, M. Trabia, R. Hixson, S. Roy, M. Pena, S. Becker, E. Daykin, E. Machorro, R. Jennings, M. Matthes, "Modeling Plastic Deformation of Steel Plates in Hypervelocity Impact Experiments," To appear in Proceedings of The 13th Hypervelocity Impact Symposium, Boulder CO, April 27-30, 2015.

[10] "How Can Aerospace Benefit from 3D Printed Titanium," accessed January 29, 2016, http://www.farinia.com/additive-manufacturing/3d-materials/how-can-aerospace-benefit-from-3d-printed-titanium-Ti6Al4V

[11] Needler, S. "F-35 Direct Manufacturing: Material Qualification Results", AeroMat Conference and Exposition 2012, presentation (WDJ1.1), Charlotte, North Carolina, June 18 – 21 2012. https://asm.confex.com/asm/aero12/webprogram/Paper30786.html

[12] Phelps, H. "Electron Beam Direct Manufacturing (EBDM) on the F-35 Lightning II", Lockheed Martin Presentation at NC State Advanced Manufacturing & Logistics Symposium, Raleigh NC, Oct 17, 2013. http://camal.ncsu.edu/wp-content/uploads/2013/10/Hank-Phelps-EBDM-Presentation-to-NC-State-Final-RevA.pdf

[13] Brandl, E., Palm, F., Michailov, V., Viehweger, B., & Leyens, C. (2011). Mechanical properties of additive manufactured titanium (Ti–6Al–4V) blocks deposited by a solid-state laser and wire. Materials and Design, 32(10), 4665–4675-4665–4675. doi:10.1016

[14] Fadida, Refael, Daniel Rittel, and Amnon Shirizly. "Dynamic Mechanical Behavior of Additively Manufactured Ti6Al4V With Controlled Voids." Journal of Applied Mechanics. 82(4), 041004 (Apr 01, 2015) (9 pages) Paper No: JAM-14-1539; doi: 10.1115/1.4029745, 2015.

[15] Radin, J, Goldsmith W. Normal projectile penetration and perforation of layered targets. Int J Impact Eng 1988;7(2):229-59.

[16] Almohandes AA, Abdel-Kader MS, Eleiche AM. Experimental investigation of the ballistic of steel-fiberglass reinforced polyester laminated plates. Compos Part B: Eng 1996;27:447-58.

[17] Hutchinson JW, Suo Z. "Mixed mode cracking in layered materials." Adv. Appl. Mech. 1992;29:63–191.

[18] Abrate, S. "Impact on laminated composites: recent advances." Appl. Mech. Rev. 1994;47:517–44. Nygus G.: Numerical Analysis Using Finite Element Method. PhD Thesis, NTU Mech. Eng. Dept., Lagos, 1983.

[19] Espinosa H, Lu H-C, Xu Y. “A novel technique for penetrator velocity measurement and damage identification in ballistic penetration experiments.” J Compos Mater 1998;32:722–43.

[20] Bosson, S. "Ramrods Shepard Hydrodynamic Tests." Science & Technology Review. September 20, 2007. Accessed February 02, 2016. https://str.llnl.gov/str/Sep07/Bosson.html.

[21] Jilek, B. (2013). Velocimetry Overview, 1–14. Retrieved from https://kb.osu.edu/dspace/bitstream/handle/1811/54247/PDV_2012_Jilek_VelocimetryOverview.pdf?sequence=1\npapers3://publication/uuid/926EAE58-2819-4298-BBBD-2C683B2B55A0

[22] Paschotta, R. 2012. (2016). Optical Heterodyne Detection. RP Photonics. Retrieved February 2, 2016, from https://www.rp-photonics.com/optical_heterodyne_detection.html

[23] Barker, L. M. and Hollenbach, R. E., Rev. Sci. Instr. 36,1617-1620 (1965).

[24] Barker, L. M., & Hollenbach, R. E. (1972). Laser interferometer for measuring high velocities of any reflecting surface. Journal of Applied Physics, 43(11), 4669–4675. doi:10.1063/1.1660986

[25] Strand, O. T., Goosman, D. R., Martinez, C., Whitworth, T. L., & Kuhlow, W. W. (2006). Compact system for high-speed velocimetry using heterodyne techniques. Review of Scientific Instruments, 77(8). doi:10.1063/1.2336749

[26] D. B. Holtkamp, Photonic Doppler velocimetry for dynamic experiments, in: 6-Laboratory Conference on Engineering and Materials at Extreme Conditions, no. LA-UR-11-05797, 2011.

[27] Howard, M., Luttman, A., Machorro, E., Kelly, R., Blair, J., Matthes, M., Hixson, R. (2015). Benchmarking Surface Position from Laser Velocimetry with High-Speed Video in Impact Experiments. Procedia Engineering, 103, 221–229. http://doi.org/10.1016/j.proeng.2015.04.030

[28] R. Schoukens, R. Pintelon, H. V. Hamme, The interpolated Fast Fourier Transform: A comparative study, IEEE Trans. Instr. Measurement 1 (2) (1992) 226–232.

[29] T. Ao, D. H. Dolan, SIRHEN: A data reduction program for photonic Doppler velocimetry measurements, Tech. Rep. SAND2010-3628, Sandia National Laboratories (2010).

[30] Ma, S., Zhang, X., & Qiu, X. M. (2009). Comparison study of MPM and SPH in modeling hypervelocity impact problems. International Journal of Impact Engineering, 36(2), 272–282. http://doi.org/10.1016/j.ijimpeng.2008.07.001

[31] Gadala MS, Wang J. Ale formulation and its application in solid mechanics. Computer Methods in Applied Mechanics and Engineering 1998;167(1–2):33–55.

[32] Belytschko T, Krongauz Y, Organ D, Fleming M, Krysl P. Meshless methods: an overview and recent developments. Computer Methods in Applied Mechanics and Engineering 1996; 139(1–4):3–47.

[33] Liu X, Liu GR. Radial point interpolation collocation method for the solution of nonlinear poisson problems. Computational Mechanics 2005;36(4):298–306.

[34] Gingold R.A. and Monaghan J. J. (1977). Smoothed particle hydrodynamics: theory and application to non-spherical stars. Mon. Not. R. Astron. Soc, (181), 375–89.

[35] Lucy L.B. (1977). A numerical approach to the testing of the fission hypothesis. Astron. J, (82), 1013–24.

[36] Liu, G. R., & Liu, M. B. (2003). Smooth Particle Hydrodynamics. World Scientific.

[37] Zukas, J. A. (1982). Impact Dynamics. New York: John Wiley & Sons.

[38] Shah QH, Abakr YA. Effect of distance from the support on the penetration mechanism of clamped circular polycarbonate armor plates. Int. J. Impact Eng. 2008;35:1244–50. doi:10.1016/j.ijimpeng.2007.07.012.

[39] Swaddiwudhipong S, Islam MJ, Liu ZS. High Velocity Penetration/Perforation Using Coupled Smooth Particle Hydrodynamics-Finite Element Method. Int. J. Prot. Struct. 2010;1:489–506.

[40] O'Daniel J, Danielson K, Boone N. Modeling fragment simulating projectile penetration into steel plates using finite elements and meshfree particles. Shock Vib. 2011;18:425–36. doi:10.3233/SAV-2010-0523.

[41] LS-DYNA® KEYWORD USER ' S MANUAL. vol. I. 971st ed. LIVERMORE SOFTWARE TECHNOLOGY CORPORATION (LSTC); 2007.

[42] S. Jeelani, J.J. Kelly, J.K. Whitefield, R. A. D. (1973). Two-Stage Light-Gas Gun Installation for Hypervelocity Impact Studies. Office of Naval Research.

[43] Sargis, P. D., Molau, N. E., Sweider, D., Lowry, M. E., & Strand, O. T. (1999). Photonic doppler velocimetry. Lawrence Livermore National Laboratory Document Number UCRL-ID-133075.

[44] Somasundaram, D. (2014). Analysis of Bolted Joints Under Medium and High Impact Loading. PhD Dissertation.

[45] Roy, S. (2015). An Approach to Model Plastic Deformation of Metallic Plates in Hypervelocity Impact Experiments. PhD Dissertation.

[46] Slewa, M. (2015). Crystalline Phase Change in Steel Alloys due to High Speed Impact. PhD Dissertation.

[47] Johnson,G., and Cook,W. (1983). An Approach to Model Plastic Deformation of Metallic Plates. Proceedings of the 7th International Symposium on Ballistics, 541–547.

[48] Katayama M, Kibe S, Toda S. A Numerical Simulation Method and Its Validation For Debris Impact Against The Whipple Bumper Shield. Int J Impact Eng 1995;17:465–76.

[49] Seidt JD, Gilat A, Klein JA, Leach JR. High Strain Rate, High Temperature Constitutive and Failure Models for EOD Impact Scenarios. SEM Annu. Conf. Expo. Exp. Appl. Mech., Society for Experimental Mechanics, Inc.; 2007, p. 15.

[50] Littlewood DJ. Simulation of Dynamic Fracture Using Peridynamics, Finite Element Modeling, and Contact. ASME 2010 Int. Mech. Eng. Congr. Expo., Vancouver, BritishColumbia, Canada: ASME; 2010, p. 1–9. doi:10.1115/IMECE2010-40621.

[51] Elshenawy T, Li QM. Influences of target strength and confinement on the penetration depth of an oil well perforator. Int J Impact Eng 2013;54:130–7.doi:10.1016/j.ijimpeng.2012.10.010.

[52] Littlewood DJ. Simulation of Dynamic Fracture Using Peridynamics, Finite Element Modeling, and Contact. ASME 2010 Int. Mech. Eng. Congr. Expo., Vancouver, British Columbia, Canada: ASME; 2010, p. 1–9. doi:10.1115/IMECE2010-40621

[53] Wang, X., & Shi, J. (2013). International Journal of Impact Engineering Validation of Johnson-Cook plasticity and damage model using impact experiment. International Journal of Impact Engineering, 60, 67–75. http://doi.org/10.1016/j.ijimpeng.2013.04.010

[54] Çengel, Y., & Boles, M. (2011). Thermodynamics An Engineering Approach (7th ed.). New York: McGraw Hill.

[55] Zheng, H.W. , Shu, C. , Chew, Y.T. and Qin, N. (2011), "A solution adaptive simulation of compressible multi-fluid flows with general equation of state", International Journal for Numerical Methods in Fluids, Vol. 67 No. 5, pp. 616-637. [CrossRef], [ISI] [Infotrieve]

[56] Mukherjee D, Rav A, Sur A, Joshi KD, Gupta SC. Shock induced spall fracture in polycrystalline copper. AIP Conf. Proc. 1591, vol. 608, AIP Publishing; 2014, p. 608–10.doi:10.1063/1.4872691.

[57] Froes FH (2015) Titanium – Physical Metallurgy, Processing and Applications. ASM International.

[58] Semiatin SL, Seetharaman V, Weiss I (1997) The thermomechanical processing of Alpha/Beta Titanium Alloys. JOM 49:33-39.

[59] Gangireddy, S., Mates, S. P., Science, M., & Division, E. (2016). High-Strain-Rate Deformation of Ti-6Al-4V through Compression Kolsky Bar at High Temperatures. In Society of Experimental Mechanics (pp. 2–7).

[60] Rogers, H. C. (1979). Adiabatic plastic deformation. Annual Review of Material Science, 9, 283–311. http://doi.org/10.1146/annurev.ms.09.080179.001435

[61] Shahan, A.R., Karimi Taheri, A. (1993). Adiabatic shear bands in titanium and titanium alloys: a critical review. Materials and Design, 14(4), 243–250. http://doi.org/10.1016/0261-3069(93)90078-A

CURRICULUM VITA

Melissa Matthes

7142 Shadow Crest Dr • Las Vegas, NV 8919 • (775) 857-8131 • matthes2@unlv.nevada.edu
• U.S Citizen

Education

University of Nevada, Las Vegas

M.S. in Mechanical Engineering — Expected Aug 2016
Focus: Materials and Mechanics — G.P.A: 3.95

B.S. in Mechanical Engineering — Aug 2010 - May 2015
G.P.A: 3.44

Senior Design Project — Aug 2014 - May 2015

Robotic Optoelectronic Test Platform for Nuclear Fusion Experimentation

- **1st Place** Mechanical Engineering Overall
- **1st Place** in Commercialization Potential
- Designed an automated xyz-axis platform to characterize Gallium Nitride Diodes
- Increased repeatability by 95%
- Decreased cost of characterization by $70,000 per specimen
- Increased productivity by 6000%

Honors

- **1st Place** Young Minds Award Overall Undergraduate & Electro-Mechanical — Nov 2015
- Nevada NSF EPSCoR UROP Grant Recipient — Spring 2014
- Alex Charter's Student Scholar HVIS — Spring 2015
- Dean's List — 2013-2015

Relevant Work Experience

Engineer I, National Security Technologies — Feb 2016 - Present

- Build one-stage gas launcher for materials research
- Review technical drawings for the gas launcher
- Develop check list for gas launcher experiments

Teaching Assistant, UNLV Department of Mechanical Engineering — Aug 2015 - Present

- Teach EGG 101 - Introductory Engineering Experience (Laboratory)
- Grade ME 400 – Mechanical Engineering Design
- Study deformation in titanium impacted by a two stage light-gas gun for aerospace/nuclear applications
- Validate computational models, dynamic material properties, and Equations of State (EOS)

Research Assistant, UNLV Department of Mechanical Engineering — May 2013 - Aug 2015

- Conducted undergraduate research under the Nevada NSF EPSCoR Undergraduate Research Opportunity Program
- Increased understanding of operation parameters for UNLV's two stage light-gas gun
- Studied plastic deformation of metallic plates impacted by a two stage light-gas gun for ?
- Collaborated with NSTec with the development of PDV analysis technique

- Designed a composite structure for blast containment in HyperMesh and run FEA in LS-DYNA

Associate Engineer, National Security Technologies May 2014 - Sep 2014
- Developed Photonic Doppler Velocimetry (PDV) data analysis techniques
- Collected data with PDV during hypervelocity impact
- Analyzed PDV data using an in house software
- Consolidated PDV data using Matlab
- Coordinated with the Site Directed Research and Development program collaborating with UNLV

Summer Intern, Nevada Automotive Test Center 2011 - 2012
- Conducted technical research, for the development of a report to be submitted to the DoD
- Coordinated and compiled documentation including test results
- Presented blast results in a briefing to the United States Marine Corps
- Supported engineering staff in collecting and analyzing data

Other Experience

Tutor, UNLV Student Support Services Sep 2014 - Present
- Subjects tutored-Math 95-432, Physics 151-182, Chem 103-121, ME 100-421

Student Worker, UNLV Department of Mathematical Sciences Oct 2010 - Mar 2014
- Logged databases for Transfer Credit Evaluations, Attendance Sheets, and Enrollments
- Assisted Department Chair with current projects
- Presented recommendations for more white boards to the provost of UNLV

Current Related Extra-Curricular

- ASME Student Chapter Chair 2012 - 2013
- UCC Complex Council Char – Residence Hall Executive Board Member Aug 2011 - May 2012
- ΠΜΣ Member April 2012 - Current
- SHPE Member Nov 2015 - Current
- College of Engineering Student Ambassador Aug 2011 - May 2014

Skills and Licensure

- Matlab
- SolidWorks
- HyperMesh
- Microsoft Office Suite
- LS-DYNA
- Lotus Notes
- Soldering
- Basic Machining
- CPR and AED
- Amateur HAM Radio Technician – Call Sign: KG7EPT

Journal Publications

1) B. O'Toole, M. Trabia, R. Hixson, S. Roy, M. Pena, S. Becker, E. Daykin, E. Machorro, **M. Matthes**, "**Modeling Plastic Deformation of Steel Plates in Hypervelocity Impact Experiments**", Procedia Engineering 103 (2015) pp 458 - 465. doi:10.1016/j.proeng.2015.04.060.
2) M. Howard, A. Luttman, E. Machorro, R. Kelly, J. Blair, **M. Matthes**, et al., "**Benchmarking Surface Position from Laser Velocimetry with High-Speed Video in Impact Experiments**," Procedia Engineering 103 (2015) pp 221 - 229. doi:10.1016/j.proeng.2015.04.030.
3) S. K. Roy, M. Trabia, B. O'Toole, **M. Matthes**, et al., "**Study of Hypervelocity Projectile Impact on Thick Metal Plates**," Shock and Vibration, vol. 2016, Article ID 4313480, 11 pages, 2016. doi:10.1155/2016/4313480.

Conference Publications

1) **M. Matthes**, B. O. Toole, M. Trabia, C. Hawkins, T. Graves, R. Hixson, E. Daykin, Z. Fussell, A. Daykin, M. Heika, S. Roy, R. Jennings, and M. Boswell, "**HYPERVELOCITY IMPACT OF TI6AL4V ALLOY MATERIALS."** International Congress of Theoretical and Applied Mechanics, Montreal, Canada, August 26, 2016.
2) **M. Matthes**, B. O. Toole, M. Trabia, S. Roy, R. Jennings, M. Boswell, T. Graves, R. Hixson, E. Daykin, **"Comparison of Failure Mechanisms Due to Shock Propagation in Forged, Layered, and Additive Manufactured Titanium Alloy"** Proceedings of 2016 SEM Conference & Expo, Orlando, FL, June 6-9, 2016.
3) M. Pena, R. Hixson, S. Becker, E. Daykin, M. Walling, B. O'Toole, M. Trabia, S. Roy, R. Jennings, **M. Matthes**, "**Use of Multiplexed Photonic Doppler Velocimetry (MPDV) System to Study Plastic Deformation of Metallic Steel Plates in High Velocity Impact**", Proceedings of 2015 SEM Conference & Expo, Costa Mesa CA, June 8-11, 2015.
4) R. Hixson, B. O'Toole, M. Trabia, S. Roy, M. Pena, S. Becker, E. Daykin, E. Machorro, R. Jennings, **M. Matthes**, "**Computational model verification using multiplexed photonic Doppler velocimetry for high velocity projectile impact on steel target**", 7th Multiscale Materials Modeling International Conference, Berkeley, CA, Oct 6-10, 2014.
5) B. O'Toole, M. Trabia, R. Jennings, S. Roy, **M. Matthes**, et al., "**Multiplexed Photonic Doppler Velocimetry (MPDV) Application in Plastic Deformation Experiments under Hypervelocity Condition**", Abstract, Photonic Doppler Velocimetry Workshop, Las Vegas, NV, June 24-26, 2014.
6) M. Trabia, B. O'Toole, S. Roy, D. Somasundaram, R. Jennings, **M. Matthes**, R. Hixson, S. Becker, E. Daykin, M. Pena, E. Machorro, "**An Approach for Measuring and Modeling of Plastic Deformation of Metallic Plates During High Velocity Impact**", Extended Abstract, NAFEMS Americas Conference, Colorado Springs CO, May 28-30, 2014.
7) S. Roy, M. Trabia, B. O'Toole, J. Thota, R. Jennings, D. Somasundaram, **M. Matthes**, et al., "**Plastic Deformation of Steel Plates under High Impact Loading**", Abstract, 84th Shock & Vibration Symposium, Atlanta GA, Nov 3-7, 2013.